

Department of Physics and Astronomy
University of Heidelberg

Master thesis

in Physics

submitted by

Tobias Buck

born in Eutin (Germany)

2015

The Emergence of spatially and kinematically coherent Planes of Satellite Galaxies in high-resolution Dark Matter only simulations

This Master Thesis has been carried out by Tobias Buck
at the
Max-Planck-Institut für Astronomie
under the supervision of
Dr. Andrea V. Macciò

and Prof. Volker Springel
Heidelberger Institut für Theoretische Studien

When a mystery is too overpowering,
one dare not disobey.

*Antoine de Saint-Exupéry,
The Little Prince*

The Emergence of spatially and kinematically coherent Planes of Satellite Galaxies in high-resolution Dark Matter only simulations:

It has recently been shown that a large fraction of the dwarf satellite galaxies orbiting the Andromeda galaxy are surprisingly well-aligned in a thin, extended and kinematically coherent planar structure. The presence of such a structure seems to challenge the current Cold Dark Matter paradigm of structure formation, which predicts a more uniform distribution of satellites around a central object. In this thesis, I show that it is possible to obtain a thin, extended, apparently rotating plane of satellites resembling the one in Andromeda in cosmological collisionless simulations based on the Cold Dark Matter model. These new high resolution simulations show a correlation between the formation time of the dark matter halo and the thickness of the plane of satellites. The simulations produce a high incidence of satellite planes as thin, extended and rich as the one in Andromeda, when high concentration/early forming halos are selected. However, the analysis of the detailed kinematics and the orbital poles of satellites in the planes shows that these planes are not a long-lived rotating structure. In fact, there exists up to a 40% chance of aligned satellites flying out of the plane within 500 Myr. Furthermore it will be shown that the plane appearance strongly depends on the specific viewing angle. Nevertheless, by tracking the formation of the satellites in the plane, it can be shown that they have been mainly accreted onto the main object along thin dark matter filaments at high redshift. These results show that the presence of a thin, extended, apparently rotating plane of satellites is not a challenge for the Cold Dark Matter paradigm.

Eigenschaften räumlich und kinematisch zusammenhängender Ebenen von Satelliten Galaxien in hochauflösenden Simulationen dunkler Materie:

Es wurde kürzlich gezeigt, dass ein Großteil der um die Andromeda Galaxie kreisenden Zwerggalaxien überraschenderweise in einer schmalen, ausgedehnten und kinematisch kohärenten Ebene angeordnet sind. Das Vorhandensein einer solchen Struktur scheint das gegenwärtig vorherrschende Strukturentstehungsparadigma der Kalten Dunklen Materie, das eine gleichförmigere Verteilung von Satellitengalaxien um zentrale Objekte vorhersagt, zu gefährden. In dieser Masterarbeit zeige ich, dass es in stoßfreien kosmologischen Simulationen basierend auf dem Modell der Kalten Dunklen Materie möglich ist, eine dünne, ausgedehnte und scheinbar rotierende Ebene von Satellitengalaxien ähnlich derjenigen um Andromeda zu erhalten. Diese neuen hochauflösenden Simulationen zeigen eine Korrelation zwischen der Entstehungszeit der Halos aus Dunkler Materie und der Dicke der Ebene aus Satellitengalaxien. Die Simulationen zeigen mit großer Häufigkeit Ebenen ebenso dünn, ausgedehnt und reich an Satelliten wie diejenige um Andromeda, wenn Dunkle Materie Halos einer hohen Konzentration/frühen Entstehungszeit gewählt werden. Allerdings zeigt die Analyse der detaillierten Kinematik und der Orbits der Satellitengalaxien, dass die Ebenen keine langlebige, rotierende Struktur darstellen. Vielmehr bestehen sie aus bis zu 40% zufällig ausgerichteter Satelliten, die bereits nach weniger als 500 Myr aus der Ebene fliegen. Insbesondere hängt die Erscheinung der Ebene sehr stark von der genauen Blickrichtung ab. Dennoch kann durch Nachverfolgen der Entstehung der Satelliten in den Ebenen um Halos hoher Konzentration/früher Entstehungszeit gezeigt werden, dass ein Großteil dieser bei hoher Rotverschiebung entlang dünner Filamente aus Dunkler Materie in den Haupthalo gesogen werden. Diese Resultate zeigen, dass das Vorhandensein einer dünnen, ausgedehnten und scheinbar rotierenden Ebene keine Herausforderung für das Paradigma der Kalten Dunklen Materie darstellt.

Contents

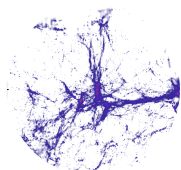
1	Introduction	1
1.1	Cosmological Standard Model	2
1.1.1	Friedmann equations and the content of the Universe	2
1.1.2	Cosmic Microwave Background	4
1.2	Structure Formation in Λ CDM	6
2	Simulating Structure Formation	9
2.1	Press-Schechter formalism for Structure Formation	9
2.2	N -body Simulation of Structure Formation	12
2.2.1	Tree codes and the Lagrangian integration scheme	12
2.2.2	Mesh codes and the Eulerian integration scheme	13
3	High Resolution Simulation	15
3.1	Initial conditions for high resolution simulations	15
3.1.1	Zel'dovich Approximation	17
3.2	Creating high resolution simulations	19
3.3	CDM Substructure Problem	21
3.3.1	Missing Satellite Problem	21
3.3.2	Suppression of Structure formation on small scales	22
3.3.3	Cusp-Core Problem	22
3.3.4	Observational detection biases	23
4	Observations and halo selection	25
4.1	Observed Planes of Satellites	25
4.1.1	Milky Way	26
4.1.2	Andromeda - M31	26
4.2	Main Halo Selection	28
4.3	Satellite Selection	30
4.4	Plane detection and analysis	32

5	Results	33
5.1	Dependence of plane parameters on halo concentration	35
5.1.1	Plane thickness vs halo concentration	36
5.1.2	Number of satellites in plane vs. concentration	41
5.2	Significance of planes	44
5.2.1	Distribution of plane parameters	48
5.3	Kinematic analysis of planes	48
5.3.1	Plane appearance under different viewing angles	48
5.3.2	Angular momentum analysis	54
5.3.3	Plane evolution and plane stability	56
5.3.4	Satellite orbits	59
5.4	Formation scenario and visual impressions of planes	62
5.4.1	Formation scenario	62
5.4.2	Visual impression of planes	64
6	Summary and Discussion	69
7	Conclusion	73
	Bibliography	i
	List of Figures	ix

1 Introduction

Although mankind has always gazed at the stars, it was only in the last 100 years that astronomers realized that the Universe is larger than our own Galaxy. In the beginning of the 20th century, the first observational evidence was obtained showing that objects outside the Milky Way exist. It was realised that galaxies are really just islands in the Universe, and their discovery directly led to the question of how they were formed and how they evolve. In the following questions regarding the Universe in general were asked. Is the Universe finite? Does it evolve over time? Is there a beginning of the Universe? In fact these questions had been asked before, but mankind had only been able to speculate about the answers. But with the new observations made at the beginning of the 20th century mankind was able to approach these questions in an empirical manner.

With the tremendous technical progress of the last few decades striking new discoveries have been made. We are now able to get well-resolved pictures of distant galaxies or, due to the finite speed of light, look millions of years back in time by observing very distant galaxies. Additionally, computers have become more powerful, making detailed simulations of galaxies and large scale structure possible. Thus our knowledge about the Universe vastly increased and the field of astronomy, particularly cosmology, the science of the Universe as a whole, evolved into a quantitative science. Detailed studies of individual galaxies revealed the surprising result that these galaxies contain much more mass than what is visible as stars and gas. The largest component of their mass is invisible to us and only observable through its gravitational effects. Hence it was named *dark matter*. A further boost in knowledge was provided by observations of the first light to travel freely through the Universe, the *Cosmic Microwave Background* (CMB) and the establishment of a standard model of cosmology, the science of the Universe as a whole. The basic parameters of this model have been determined to very high accuracy by observations and are repeatedly confirmed through independent measurements. However, there are many unsolved problems and questions that have been raised by recent observations of the distinct features of galaxies. For example, it seems that the satellite galaxies of our companion galaxy, the Andromeda galaxy, are aligned in a thin rotating plane. This alignment remains unexplained in a cosmological context and is the subject of this thesis.



1.1 Cosmological Standard Model

The Universe we live in can be described to a very high level of accuracy as an expanding, almost flat space-time, the dynamics of which are governed by a collisionless form of matter and a repulsive form of energy. The collisionless Cold Dark Matter model (CDM) accompanied with a cosmological constant Λ (Λ CDM) has become the standard model for describing our Universe. It is tremendously successful in describing the expansion history, structure formation and related statistical properties such as the power spectrum. In the following chapter this model will be described in more detail.

1.1.1 Friedmann equations and the content of the Universe

The dynamics of the Universe are described by the *Friedmann-Lemaître* equations for the scale factor $a(t) = R(t)/R_0$, which measures the expansion $R(t)$ of the Universe at a time t relative to its present day expansion R_0 ¹ (commonly: $a(t = 0) = 0$, $a_0 = 1$). In a universal form they read:

$$\left(\frac{\dot{a}}{a}\right)^2 = \frac{8\pi G}{3}\rho - \frac{Kc^2}{a^2} + \frac{\Lambda}{3} \quad (1.1)$$

and

$$\frac{\ddot{a}}{a} = -\frac{4\pi G}{3}\left(\rho + \frac{3P}{c^2}\right) + \frac{\Lambda}{3} \quad (1.2)$$

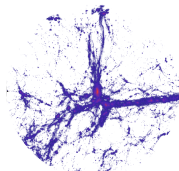
where G denotes the gravitational constant, ρ the energy density of the Universe in matter and radiation and K is a term describing the spatial curvature of the Universe. Λ is the cosmological constant accounting for the effect of Dark Energy, P is a pressure term and c is the speed of light.

In the cosmological standard model the curvature term K is equal to zero, resulting in the flat geometry of our Universe, and its energy-mass budget consists of three components, commonly quantified by a density parameter Ω_i measuring the energy density of each component in terms of the critical density² at present time.

Dark Energy dominates the energy density of the Universe at the present time and its relative contribution is increasing. Its energy density Ω_Λ has a negative equation of state such that it exhibits negative pressure and is thus repulsive.

¹Present day values are typically denoted by the subscript 0

²The critical density $\rho_{c,0}$ denotes the density at which the geometry of our Universe is flat. The present day value is: $\rho_{c,0} = 2.7755 \cdot 10^{11} h^2 M_\odot / \text{Mpc}^3$



It is therefore responsible for the accelerated expansion of the Universe. In the equations governing the expansion of the Universe, Dark Energy is represented by the cosmological constant Λ , first introduced by Albert Einstein for completely different reasons.

Matter consists of two fundamentally different sub-components. The larger of the two components interacts only gravitationally, and only weakly via the electro-weak force, if at all. Thus it does not radiate and is therefore not directly observable, which is the reason why it was named *Dark Matter*. It was originally introduced as an invisible source of gravitation in galaxy cluster to account for their dynamics (Zwicky 1933). Nothing is known of its fundamental nature apart from how it interacts. To date it is not yet been directly detected but many attempts to resolve these problems both theoretically and observationally are being made (Bertone et al. 2005). Dark matter governs the structure formation and the evolution of the dark structure of the Universe on all scales.

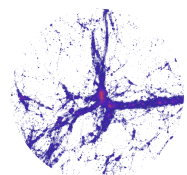
The other component contributing to the matter content of the Universe is much smaller compared to the budget in Dark Matter. It interacts electromagnetically, producing radiation, and is therefore directly observable. This form is “normal”, visible matter (e.g. gas and dust), forming stars³, planets and everything we know from our daily life. It is made out of baryons and its energy density Ω_b is only $0.15\Omega_m$ (Planck Collaboration et al. 2014). In the past the matter energy density used to dominate the expansion of the Universe but its relative contribution is decreasing in favor of Dark Energy.

Radiation The energy density of radiation Ω_r was important at very early times in the evolution of the Universe, but can be neglected at present times (Aceves 2013). As the name implies, it is the energy density contained in photons, and it mainly consists of “Cosmic Microwave Background” (CMB, see 1.1.2) photons.

To summarize our Universe mainly consist of dark or unknown energy forms named *Dark Energy* Λ and *Cold Dark Matter* (CDM). Therefore the theory describing the evolution of such a Universe is called Λ CDM. At the present time the sum of all three components is unity (Planck Collaboration et al. 2014),

$$\Omega_{r,0} + \Omega_{m,0} + \Omega_{\Lambda,0} = 1 \quad (1.3)$$

³especially Death Stars (Vader et al. 1977)



resulting in a Euclidean geometry of the Universe. As mentioned above, the contributions of all of the components scale with the expansion of the Universe, changing their relative contribution, but they always add up to the value of the critical density,

$$\frac{\rho_{\text{crit}}(t)}{\rho_{\text{crit},0}} = \frac{H(t)}{H_0} = \Omega_r(t) + \Omega_m(t) + \Omega_\Lambda(t) = \frac{\Omega_{r,0}}{a(t)^4} + \frac{\Omega_{m,0}}{a(t)^3} + \Omega_{\Lambda,0} \quad (1.4)$$

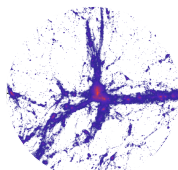
where $H = \dot{a}/a$ is the Hubble constant measuring the relative expansion rate of the Universe. The present day value is commonly presented as $H_0 = h100 \text{ km s}^{-1} \text{ Mpc}^{-1}$. A more convenient way of describing the expansion of the Universe is in terms of the redshift z , defined as $z = (1/a) - 1$. This makes the expansion of the Universe directly measurable from observations, since the redshift of objects can be easily obtained from spectra. For this thesis, the values of the various parameters in equation 1.4 were taken from the Planck Collaboration (2014) with numerical values of $\Omega_r < 10^{-4}$, $\Omega_m = 0.3175$, $\Omega_\Lambda = 0.6825$ and $h = 0.671$ inferred from cosmic microwave background (CMB) radiation measurements (see section 1.1.2).

1.1.2 Cosmic Microwave Background

The *cosmic microwave background* (CMB) is a nearly isotropic thermal radiation field of temperature $\sim 2.7 \text{ K}$ present everywhere in the Universe. It has remarkably small fluctuations of order $\Delta T/T \sim 2 \cdot 10^{-5}$ and was first detected by Penzias and Wilson (1965). It originates from the light released during recombination and encodes a great deal of valuable information about the very early Universe as well as the cosmological parameters in general. The origin and importance of the CMB in cosmology is described in this section.

Up to $380,000^4$ years after the Big Bang, matter and radiation were in thermal equilibrium. The temperature and density of the ancient Universe were extremely high, and the Universe was filled with a hot plasma of protons, electrons, neutrinos and photons. Due to the Thompson scattering of photons from free electrons, the mean free path of photons was incredibly small and photons were not able to stream freely. Due to continued expansion of the Universe, the temperature and densities dropped until electrons and protons were able to recombine into neutral hydrogen atoms. At the stage when electron number densities fell below a critical value, photon-electron scattering stopped. Matter and radiation dropped out of thermal equilibrium and decoupled, and photons started propagating through the Universe with an energy spectrum of thermal radiation whose temperature was

⁴This is roughly $1.2 \cdot 10^{13} \text{ s}$ or $2.22 \cdot 10^{56}$ Planck times, where the Planck time measures the smallest possible time interval.



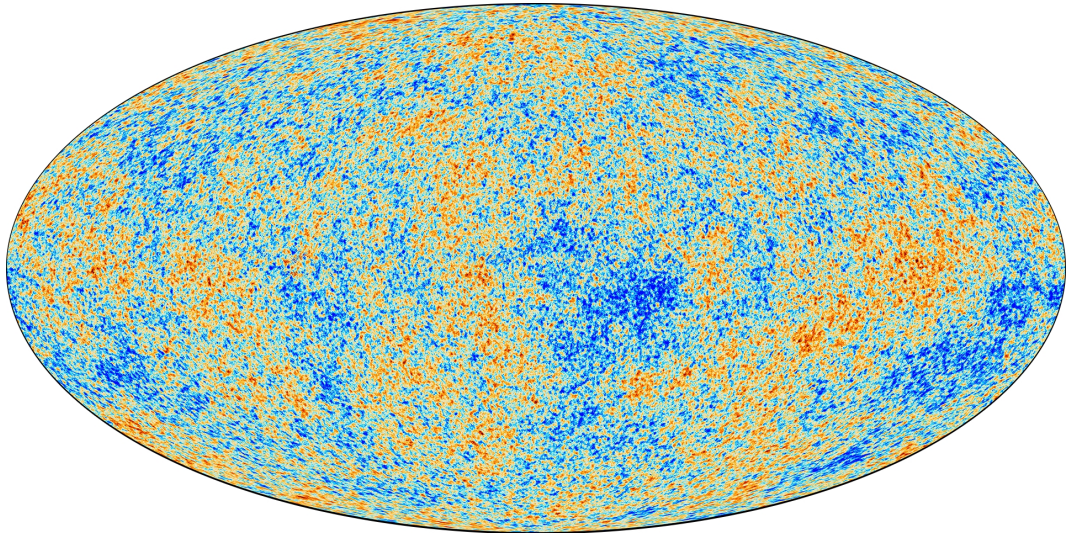


Figure 1.1: The anisotropies of the Cosmic microwave background (CMB) as observed by Planck. The CMB is a snapshot of the oldest light in our Universe, imprinted on the sky when the Universe was just 380,000 years old. It shows tiny temperature fluctuations that correspond to regions of slightly different densities, representing the seeds of all future structure, including the present stars and galaxies. (Planck Collaboration et al. 2014).

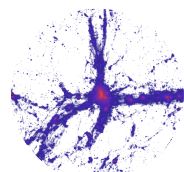
that of the matter-radiation plasma at the point of decoupling. As the Universe expands, photons are redshifted and the temperature of their thermal radiation field decreases. Nowadays, this radiation field is observable as the CMB.

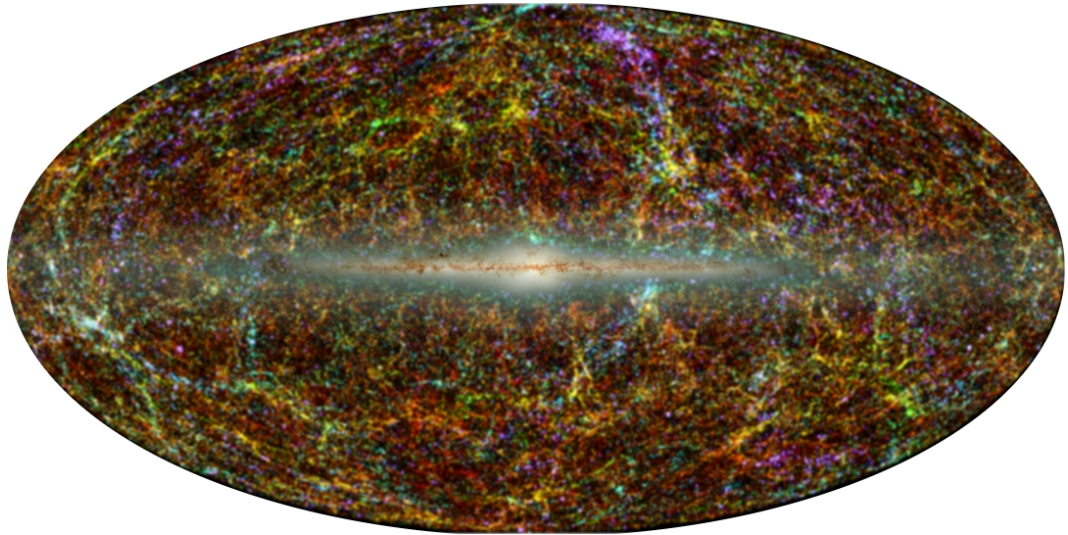
Small anisotropies in the CMB directly translate into anisotropies in the matter distribution of the Universe, and observational data of the CMB enables us to quantify initial density perturbations at the time of decoupling, when structures started to grow. Thus the CMB can tell us the initial conditions of our Universe to very high accuracy. We therefore know the exact initial configurations for our models describing the Universe. In this sense, Figure 1.1 represents the initial configuration of our Universe, whereas Figure 1.2 shows the outcome of the evolution of this initial configuration up to the present day.

The initial density perturbations are conveniently described by the matter power spectrum $P(k)$, the variance of over-densities $\delta := \delta\rho/\bar{\rho}$ in Fourier space.

$$\langle \hat{\delta}(\mathbf{k}) \hat{\delta}^*(\mathbf{k}') \rangle =: (2\pi)^3 P(k) \delta_D(\mathbf{k} - \mathbf{k}') \quad (1.5)$$

In this equation, δ_D is the Dirac delta distribution. The power spectrum is a measure of the amplitude of density perturbations on scales $\lambda = 2\pi/k$, and must not depend on direction in the isotropic case, $P(\mathbf{k}) = P(k)$. All of the statistical information





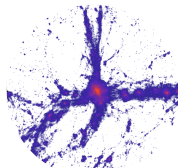
46

Figure 1.2: All-sky map of the galaxies in the 2MASS survey, colour-coded by their distance from the Earth. Blue dots show the nearest sources, through green to the most distant sources shown in red. This picture represents the present day stage of our Universe, evolved from the initial conditions set by the CMB. The survey picture is overlaid by a picture of our Galaxy indicating where the sky is obscured by its disk (Skrutskie et al. 2006).

needed to reconstruct the density field is encoded in the power spectrum. From the principle of scale invariance it follows that the primordial power spectrum has to be a power law with index n . The shape of the power spectrum is subsequently altered during the evolution of the Universe (compare 1.2).

1.2 Structure Formation in Λ CDM

Today's Universe exhibits very large density fluctuations between galaxy cluster environments and nearly empty space called voids (compare also Fig.: 1.2), while the amplitudes of the CMB anisotropies are very small (see section 1.1.2). This implies that the inhomogeneities must have grown significantly since early times in the Universe. This evolution of the matter density field occurs because gravitational forces amplify tiny density fluctuations. Over-dense regions decouple from the expansion of the Universe due to their self-gravitation. As a consequence these regions expand more slowly, and relative density fluctuations get amplified. At a



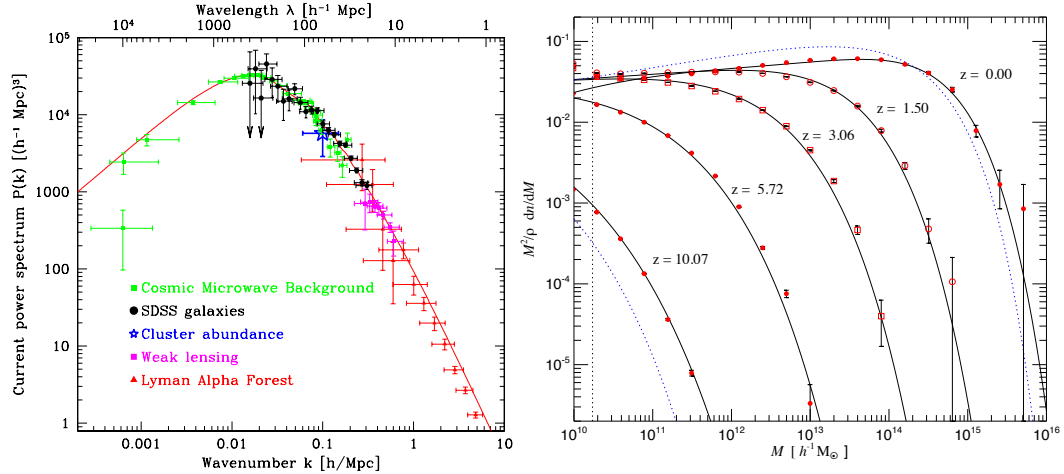
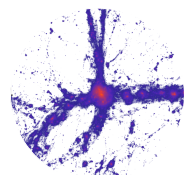


Figure 1.3: *Left:* Power spectrum constraints from different measurements (Tegmark et al. 2004). *Right:* Differential halo number density as a function of mass and redshift in the Millennium simulation (Springel et al. 2005).

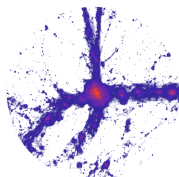
critical value of $\delta_{\text{crit}} \sim 1.69$, density fluctuations start to collapse into gravitationally bound objects.

As described above, the much larger part of the cosmic matter is Dark Matter. In the framework of Λ CDM, Dark Matter consists of heavy particles with negligible velocity dispersion and is therefore dynamically cold, hence the name Cold Dark Matter (CDM). Luminous baryonic matter contributes $\lesssim 20\%$ of the total matter content. Since baryonic matter drops out of thermal equilibrium later than Dark Matter, primordial structure formation is governed by dark matter, and the resulting structures are called *dark matter halos*. CDM structures grow in a hierarchical way, with smaller scales collapsing earlier than larger scales. The explanation for the *hierarchical structure formation* in CDM is found in the precise shape of the power spectrum given by the transfer function. Due to the finite speed of light as propagation speed of gravitational interactions and the fact that the Universe has a finite age gravitational interactions are limited to a volume of radius r_H , the Hubble radius, which acts like an event horizon. Structures smaller than this radius are able to collapse while perturbations larger than this radius can only grow but not collapse. Since the Big Bang the Hubble radius has grown and therefore more and more perturbations could enter the horizon. The precise shape of the power spectrum depends on the time when perturbations enter the horizon. At early times, when baryonic matter was in thermal equilibrium with radiation the growth of perturbations smaller than the horizon is strongly suppressed by radiation pressure,



while perturbations larger than the horizon grew until they entered the horizon and were suppressed. At later times, after dropping out of thermal equilibrium, the structures could grow unopposed on all scales bigger than the Jeans scale. On galactic scales, non-linear effects of gravity transport power from larger to smaller scales (for further details see Schneider (2006)).

Due to the non-linearity of structure formation, numerical simulations are best suited for making predictions based on a cosmological model. The success of Λ CDM lies in the excellent agreement of observations with results from numerical N -body simulations of structure formation. Under the assumption that galaxies trace the distribution of Dark Matter in the Universe, the observed distribution of galaxies is in excellent agreement with the clustering of Dark Matter halos in numerical simulations (Springel et al. 2005). This can be seen, for example, by comparing large scale surveys with large scale simulations of structure formation (see Fig.: 2.1).



2 Simulating Structure Formation

In this chapter, the theory for describing structure formation in a Λ CDM Universe is presented. Firstly, the equations governing structure formation are introduced and explained. Secondly, the solutions of these equations obtained using numerical computer programs and the possible algorithms to solve them are described.

2.1 Press-Schechter formalism for Structure Formation

The description of the Press-Schechter formalism in this section is mainly based on the text book by Schneider (2006). Structure formation in the Universe can be understood in the framework of perturbation theory. From observations of the CMB it is clear that initial density perturbations must have grown over time. The density field can be described by the relative density contrast

$$\delta(\mathbf{r}, t) = \frac{\rho(\mathbf{r}, t) - \bar{\rho}(t)}{\bar{\rho}(t)} \quad (2.1)$$

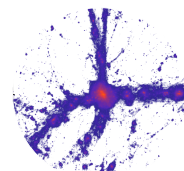
where $\bar{\rho}(t)$ is the mean density in the Universe at time t . For length scales smaller than the Hubble radius, structure formation can be described in the framework of linear perturbation theory. The second-order differential equation governing the growth of the density contrast δ reads:

$$\frac{\partial^2 \delta}{\partial t^2} + \frac{2\dot{a}}{a} \frac{\partial \delta}{\partial t} = 4\pi G \bar{\rho} \delta \quad (2.2)$$

where a is the cosmic scale factor. This equation has solutions of the form

$$\delta(\mathbf{r}, t) = D(t) \tilde{\delta}(\mathbf{r}) \quad (2.3)$$

where $D(t)$ is the growth factor describing the temporal evolution of a perturbation and $\tilde{\delta}(\mathbf{r})$ is an arbitrary function of the spatial coordinates. In the special case of an Einstein-de Sitter Universe $D(t)$ is of the form $D(t) = (t/t_0)^{2/3} = a(t)$. These equations describe how density perturbations grow, but they are not able to describe the complete function $\delta(\mathbf{r})$ of a Universe. The exact functional form



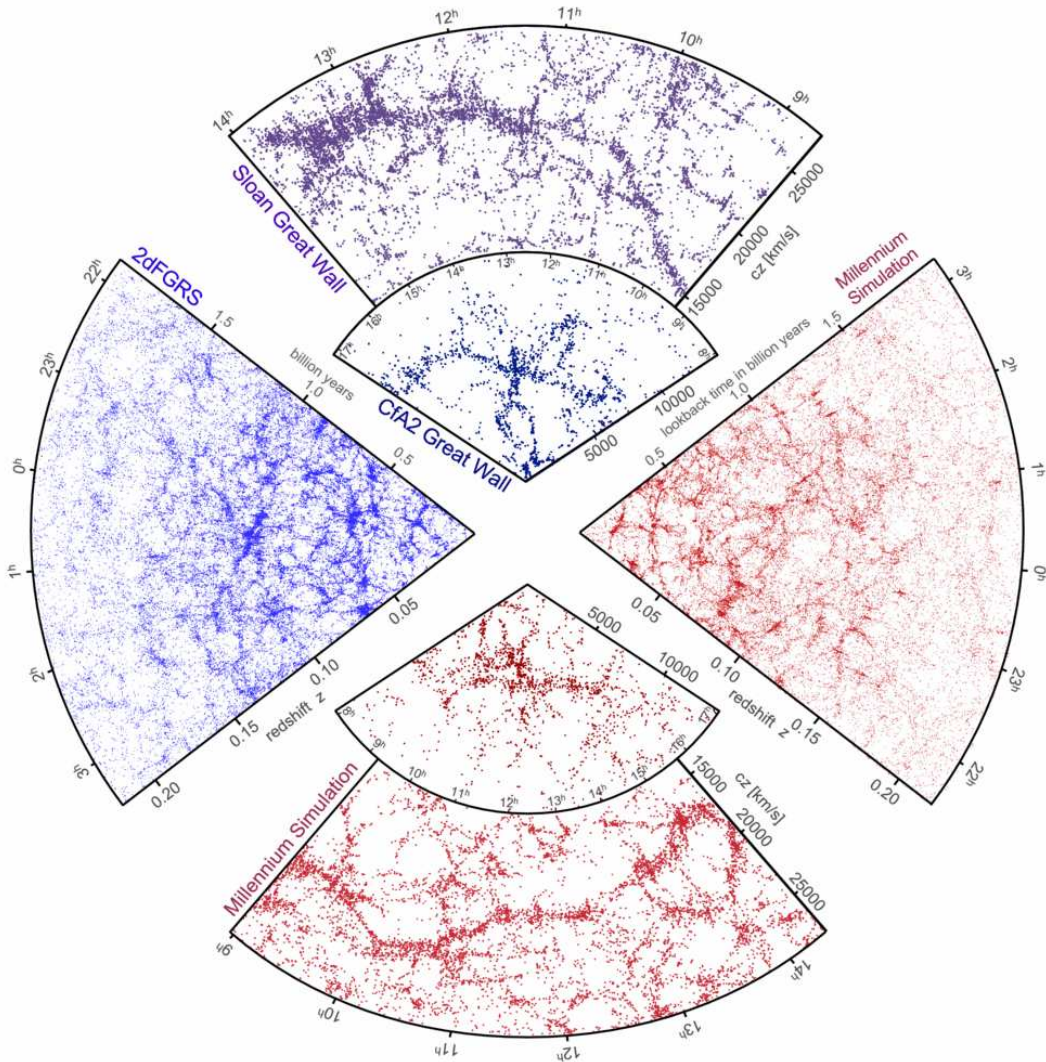
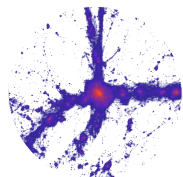


Figure 2.1: The galaxy distributions obtained from spectroscopic redshift surveys and from mock catalogues constructed from cosmological simulations are presented for comparison. The wedge on the left (*blue*) shows data from the 2dF galaxy redshift survey, which measured the distances to more than 220,000 galaxies in the southern sky out to a depth of 2 billion light years. The upper wedge (*purple*) shows SDSS data, which includes over 650,000 observed galaxies in the northern sky. At the bottom and on the right (*red*), mock galaxy surveys constructed using semi-analytic techniques to simulate the formation and evolution of galaxies in the Millennium simulation are shown (Springel et al. 2006).



depends on the specific initial conditions. It is therefore desirable to describe the statistical properties of structure formation rather than detailed mass distributions. In this sense, the density field δ is considered a *random field* and any individual mass distribution with the same statistical properties as δ is called a *realization of the random field*. The basic quantity used to describe the statistical properties of a random field is the *power spectrum*, $P(k)$, defined as the Fourier transformation of the two point correlation function.

$$\langle \hat{\delta}(\mathbf{k}) \hat{\delta}(\mathbf{k}') \rangle = (2\pi)^3 P(k) \delta_D^3(\mathbf{k} - \mathbf{k}') \quad (2.4)$$

where $\hat{\delta}(\mathbf{k})$ is the Fourier transform of the density contrast and δ_D^3 is the three dimensional Dirac delta distribution. If, at some point in time, the density contrast δ in some region of the Universe exceeds the threshold of $\delta_{\text{crit}} = 1.69$, it will collapse and form a dark matter halo. Press and Schechter (1974) introduced a model that allows computation of the number density of collapsed objects as a function of their mass from the density field δ . This formalism will be described here.

The density field smoothed on a comoving scale R reads:

$$\delta_R(\mathbf{r}, R) = \int \delta(\mathbf{r}) W(\mathbf{r} - \mathbf{r}', R) d^3 r' \quad (2.5)$$

The smoothed field contains only fluctuations on scales larger than R . If the density fluctuation is sufficiently large, such that $\delta \gtrsim \delta_{\text{crit}}$, this density peak will collapse to form an object of mass $M \sim (4\pi/3)R^3\rho$. If the statistical properties of the density field δ are Gaussian, these properties are solely defined by the power spectrum, and the probability for a density peak with an amplitude higher than the threshold δ_{crit} is given by:

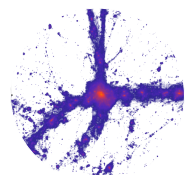
$$P(\delta > \delta_{\text{crit}}) = \frac{1}{\sqrt{2\pi}\sigma(M)} \int_{\delta_{\text{crit}}}^{\infty} \exp\left(-\frac{\delta_R^2}{2\sigma_R^2(M)}\right) d\delta_R \quad (2.6)$$

Here M is the mass of a sphere of radius R as defined previously, and σ_R denotes the variance of the density field $\delta(\mathbf{r})$ on a given scale R , which can easily be calculated from the convolution of the power spectrum with the window function W

$$\sigma_R^2(M) = \frac{1}{2\pi^2} \int_0^{\infty} P(k) \tilde{W}^2(\mathbf{k}, R) k^2 dk \quad (2.7)$$

Under the assumption that the mass function of collapsed objects is equal to twice the probability of finding a density peak above the threshold δ_{crit} , one obtains the number density of collapsed objects as:

$$n(M, t) dM = -\sqrt{\frac{2}{\pi}} \frac{d\sigma(M)}{dM} \frac{\bar{\rho} \delta_c}{M \sigma^2(M)} \exp\left(-\frac{\delta_{\text{crit}}^2}{2\sigma^2(M)}\right) dM \quad (2.8)$$



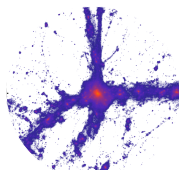
A plot of this function for different times (redshifts) is shown in Figure 1.3

2.2 N -body Simulation of Structure Formation

The formalism of Press and Schechter as introduced in the previous section describes structure formation in linear theory. It gives remarkably good results and predicts the number density of dark matter halos correctly. However, structure formation is a highly non-linear process, which for the dark sector (CDM) is entirely driven by gravity. To capture it properly, one needs to account for non-linearities, which are practically impossible to calculate analytically. One possibility for modelling the structure formation in detail is to perform N -body simulations representing a density distribution of a large number (N) of mass elements (particles) and to evaluate their mutual gravitational forces. This is typically done using N -body codes, which integrate the equations of motion for the $6N$ phase space coordinates. Simple integration of the orbit of every single particle needs N^2 force evaluations. A very large number of particles is needed to resolve structure formation properly. High resolution simulations can therefore become extremely computationally expensive, and several techniques have been developed to reduce the computational expense. In general, two different kinds of codes have been developed for simulating structure formation. *Tree codes* build on Lagrangian integration schemes and *particle mesh codes* utilize Eulerian integration schemes. For the simulations performed for this thesis, the *tree code* PKDGRAV2 by Stadel (2001, 2013) was used.

2.2.1 Tree codes and the Lagrangian integration scheme

Lagrangian integration schemes discretize a mass distribution into single mass elements (particles) and trace the flow of matter. The properties of these particles are arbitrary, and they have nothing in common with real particles like, for example, atoms. Rather, the choice of particles and their mass depends on the desired resolution. All of the required physical quantities like velocity, pressure, temperature or mass are then assigned to these particles and traced as the particles flow. Because the particles move with the flow the total time derivative d/dt for all of the desired quantities has to be integrated. To save on computational costs, particles can be grouped together. As the gravitational force falls off with distance proportional $1/r^2$, particles at large distances from each other contribute very little to the total force. One can therefore divide the simulated volume recursively into sub-volumes containing fewer and fewer particles until a pre-specified minimum number of particles remains in the lowest sub-volume cell. This division into sub-volumes



is performed by demanding the same number of particles or an equal volume for the resulting sub-volume. An equal number of particles results in an efficient parallelization, while an equal amount of volume gives better accuracy for the force calculation (Dubinski 1996; Stadel 2001).

Dividing the volume in this way results in a hierarchical tree structure, which gives the *tree code* its name. For sufficiently distant particles, the opening angle of a cell of the tree becomes small and the gravitational force of all the particles in the cell can be approximated by a multipole expansion. Thus *tree codes* achieve a scaling proportional to $N \log(N)$ (Barnes and Hut 1986). For a detailed description of the tree method implemented in `PKDGRAV2` see Stadel (2001).

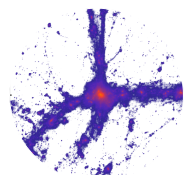
Special care has to be taken for close encounters between two particles. As the particles do not represent a physical body but rather an approximation of a continuous mass distribution, the direct integration of their forces at close encounters could lead to a spurious increase in kinetic energy. This is due to the fact that the time spent in close encounters is much smaller than the time of one integration step, and therefore integrating over one time step leads to a much larger mean acceleration of the particles. In order to reduce this numerical artefact, the gravitational potential can be smoothed below a certain length scale by introducing a *gravitational softening length* ϵ (Power et al. 2003) to modify the Green's function

$$F(r) = -\frac{1}{r^2 + \epsilon^2} \quad (2.9)$$

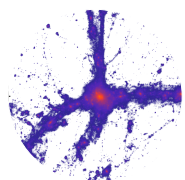
Thus a lower bound on the spatial resolution of the simulation is introduced, where typically only structures above 2.5ϵ are robustly resolved (Klypin et al. 2001; Power et al. 2003).

2.2.2 Mesh codes and the Eulerian integration scheme

In contrast to the Lagrangian scheme, Eulerian schemes assign physical quantities to volume elements at fixed positions. They discretize space with a Cartesian grid and then solve the equations of motion at spatially fixed points, in order to calculate the flow of quantities through a given volume element. Therefore, the partial time derivative $\partial/\partial t$ is integrated at each time step. To solve for the flux through a given cell, the Riemann problem, which describes the evolution of discontinuities, has to be solved at the cell interfaces. For this reason, Eulerian methods are well suited to resolving shocks and instabilities. In order to resolve large scales and large gradients in the quantities, the mesh can be refined locally (adaptive mesh refinement, AMR). As with tree codes, *mesh codes* scale as $N \log(N)$ (Toukmaji and Board 1996). However, *mesh codes* are not Galilean invariant (Wadsley et al. 2008;



Tasker et al. 2008), which makes them particularly bad for simulating galaxy and structure formation, where high relative velocities are often present. Nevertheless, attempts to overcome this problem are being made by introducing moving mesh codes, where the mesh cells move with the flow of matter. For more details see Springel (2010).

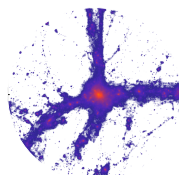


3 High Resolution Simulation

Using the methods described in the previous chapter, structure formation in the Universe can be modelled accurately and the formation process of galactic dark matter halos can be observed. Initial density perturbations collapse into so called sheets and filaments with a characteristic length scale of ~ 100 Mpc, forming a web-like structure called the cosmic web. At the nodes of these filaments, galaxy clusters and massive galaxies form. The outcome of such large scale simulations, e.g. the Millennium II simulation (Boylan-Kolchin et al. 2009) can be compared to surveys of equal scale such as SDSS (Abazajian et al. 2009) or 6dF (Jones et al. (2009), see also Figure 2.1). By zooming into a specific region of the cosmic web and refining this particular region to high resolution, one can study the structure and substructure formation of, for example, a galaxy and its dwarf galaxies, in a cosmological context. For this purpose, one needs to derive initial conditions for the high resolution run out of the initial conditions used for the lower resolution simulation. The process of creating these initial conditions will be described in this chapter.

3.1 Initial conditions for high resolution simulations

In order to study detailed structures of dark matter halos in a cosmological context, one needs enough resolution to robustly resolve substructures. This means that for a given subhalo mass, one needs a sufficient number of dark matter particles to sample in this halo. For example, to resolve a $10^8 h^{-1} M_\odot$ dark matter halo robustly, one needs on the order of 100 dark matter particles, which leads to a particle mass of about $10^6 h^{-1} M_\odot$. Sampling an entire cosmological volume with such particles is too computationally expensive. Instead, one can run a cosmological simulation with higher mass particles to resolve the main halos and afterwards select interesting ones to rerun in much higher resolution. Thereby the large scale mass distribution is sampled with low resolution particles (with high mass particles) while for the high resolution (low mass particle) region, the volume containing all of the particles in the halo of interest is sampled using particles with lower masses, so that the mass distribution of the underlying low resolution simulations is reproduced. There



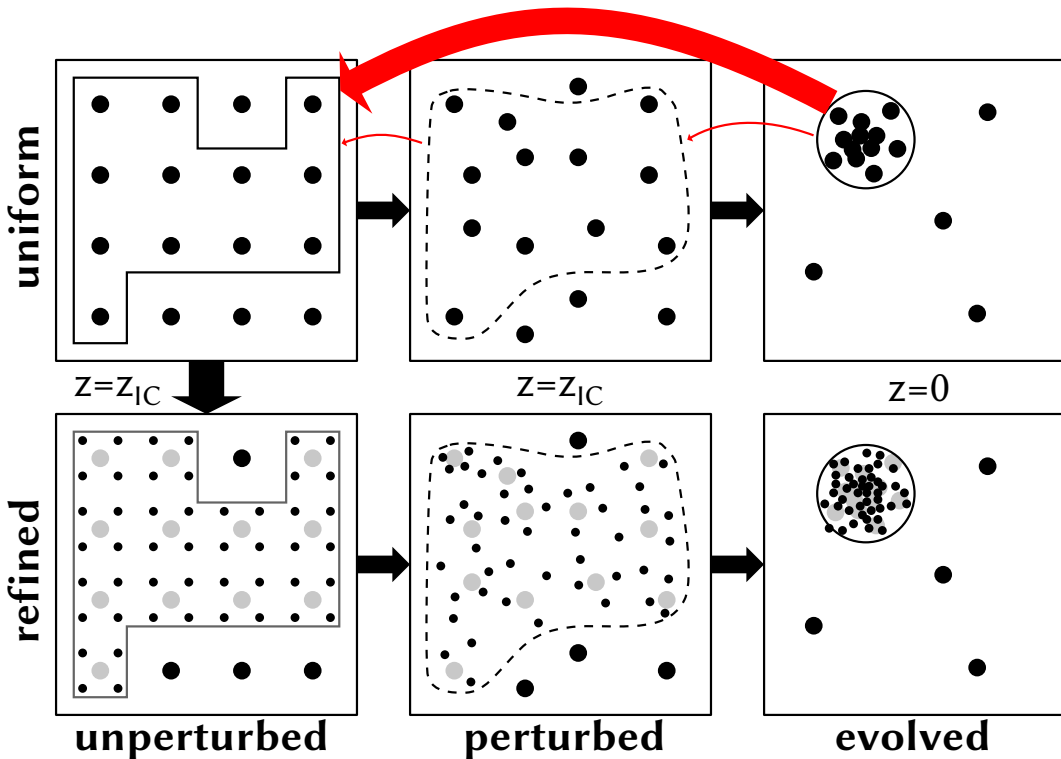
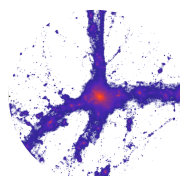


Figure 3.1: Schematic of the creation process of the initial conditions for “zoom-in” simulations. The *upper panels* represent a low resolution simulation. The left panel shows the particles on an unperturbed Cartesian grid at $z = z_{IC}$, the middle panel shows the perturbed particle positions at $z = z_{IC}$ and the right panel shows the outcome of the simulation at $z = 0$. The *lower panels* represent the high resolution simulation with small black dots showing the high resolution particles of lower mass, big black dots showing the low resolution particles sampling the large scale max distribution and big grey dots showing the the position of the former low resolution particles in the region of interest. From left to right, the unperturbed Cartesian grid of particles, the perturbed grid of particles and the evolved simulation are shown. The dashed and solid black lines in the middle and respectively in the left panels show the Lagrangian volume of the region of interest. The figure is taken from Herpich (2013).

are many examples of such “zoom-in” simulations (e.g. Navarro et al. (1996, 1997); Springel et al. (2008); Gillet et al. (2015)). An overview of how the initial conditions are set in such simulations will be given below.



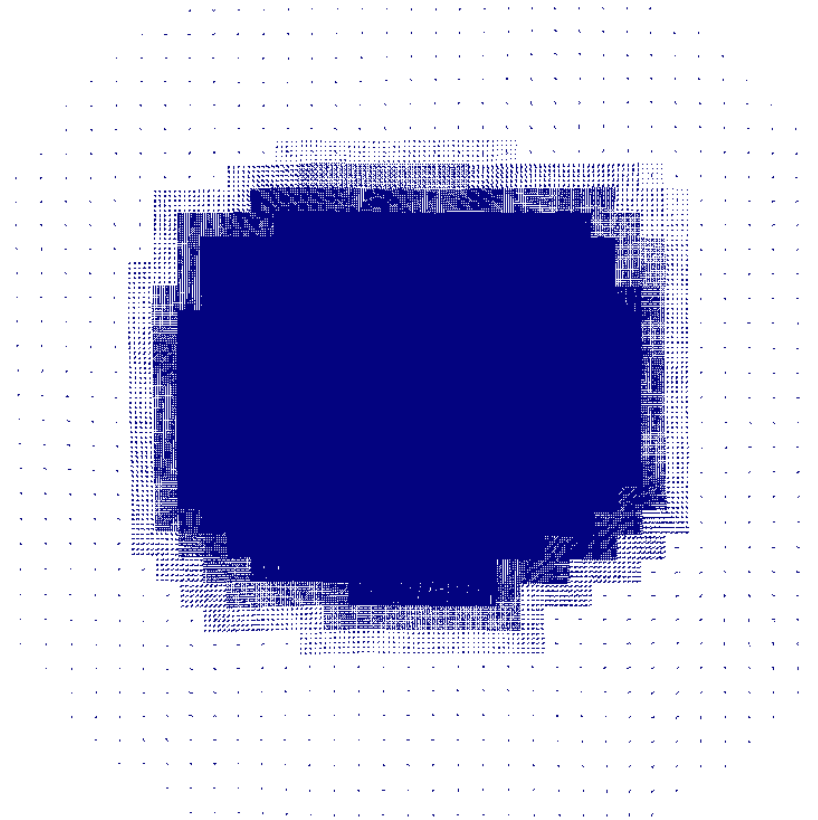
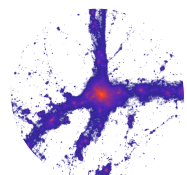


Figure 3.2: A snapshot of the initial conditions for a “zoom-in” simulation. The dark blue part in the middle is sampled by the lowest mass particles with the lowest inter-particle distance, followed by layers of increasing particle masses and inter-particle distances. The highest particle mass layer, reproducing the large scale mass distribution of the whole box, is not shown here.

3.1.1 Zel'dovich Approximation

Initial conditions can be easily constructed using the Zel'dovich approximation, first introduced by Zel'dovich (1970). This theory is based on an approximation of structure growth in the early universe that extrapolates the solutions of perturbation theory for gravitational instabilities from the linear regime to the nonlinear regime. The Zel'dovich approximation has been proven to be very accurate in the linear regime, and by extrapolation one obtains qualitative models for structure growth in the nonlinear regime ($\delta \gg 1$). Therefore this approach is well suited to create initial conditions for N -body simulations.



The necessary initial conditions consist of a set of position and velocity values at very high redshift ($z \sim 99$) and hence very early times in the Universe. The spatial position \mathbf{r} is calculated as a function of time and the initial Lagrangian coordinate \mathbf{q} of the particle (Shandarin and Zeldovich 1989) and is implemented in comoving coordinates \mathbf{x} . The evolution of the comoving coordinate \mathbf{x} is given by the Lagrangian coordinate \mathbf{q} itself and a contribution from the displacements $\mathbf{p}(\mathbf{q})$ caused by forces from a potential field.

$$\mathbf{x}(t, \mathbf{q}) = \frac{\mathbf{r}(t, \mathbf{q})}{a(t)} = \mathbf{q} + b(t)\mathbf{p}(\mathbf{q}) \quad (3.1)$$

In this equation $a(t)$ is the cosmic expansion factor, determined solely from cosmological parameters and $b(t)$ is the growth rate of density perturbations. From linear density perturbations it follows that $b(t)/a(t) = D(t)$ (see chapter 2, Eq.: 2.3). The displacements derived from the potential field can be calculated as follows

$$\mathbf{p}(\mathbf{q}) = \mathbf{F}(\mathbf{q}) = -\nabla\Phi(\mathbf{q}) \quad (3.2)$$

where the potential field Φ is related to the density field according to the Poisson equation 2.2. For convenience the Poisson equation is solved in Fourier space. On the one hand the information of the density field is given by the power spectrum (Eq.: 1.5), which is a function of the Fourier modes k , and on the other hand the partial differential Poisson equation in real space becomes an algebraic equation in Fourier space, which makes the solution much more straightforward.

$$-\mathbf{k}^2\hat{\Phi}(\mathbf{k}) = 4\pi G\hat{\rho}(\mathbf{k}) \quad (3.3)$$

In the simulations, a finite volume V with periodic boundary conditions is used to represent a small fraction of the cosmic volume. In this case, the power spectrum is given by

$$P(k) = \frac{\langle \hat{\delta}(\mathbf{k})\hat{\delta}^*(\mathbf{k}) \rangle}{V} \quad (3.4)$$

(Binney and Tremaine 2008) where the density field δ is represented by a Gaussian random field following the power spectrum. Thus the expectation value can be calculated as the mean value. A combination of equation 3.3 and 3.4 makes it possible to calculate the potential field $\hat{\Phi}(\mathbf{k})$. From this the forces $\hat{\mathbf{F}}(\mathbf{q})$ in Fourier space can be calculated as:

$$\hat{\mathbf{F}}(\mathbf{q}) = -i\mathbf{k}\hat{\Phi}(\mathbf{q}) \quad (3.5)$$

Transforming this equation back to real space and plugging it into the Zel'dovich approximation (Eq.: 3.1) leads to the initial comoving positions. In such a way,

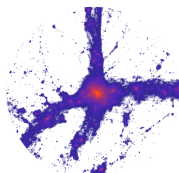


Table 3.1: The halo properties of all the high resolution simulations run for this thesis.

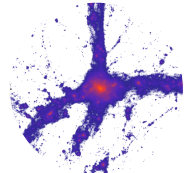
Halo	Box size [h^{-1} Mpc]	M_{200} [$10^{12} h^{-1} M_\odot$]	c_{200}	N_{200}	Force soft. [h^{-1} kpc]
1	80	1.003	12.03	7 625 912	0.29
2	80	1.389	11.35	5 408 955	0.36
3	80	0.848	6.86	6 448 219	0.29
4	60	0.626	13.30	7 105 711	0.25
5	60	0.864	13.93	9 808 180	0.25
6	60	0.702	10.67	7 968 616	0.25
7	60	0.535	17.19	6 071 696	0.25
8	60	0.637	4.18	7 230 898	0.25
9	60	0.907	6.93	7 502 238	0.27
10	60	0.813	7.19	9 226 352	0.25
11	60	0.654	5.63	7 428 609	0.25
12	60	0.890	7.65	7 367 008	0.25
13	60	0.661	5.63	7 499 975	0.25
14	60	0.570	8.19	6 471 415	0.27
15	60	0.760	9.14	8 630 941	0.25
16	60	0.831	8.69	9 430 020	0.25
17	60	0.872	11.63	7 215 346	0.28
18	30	0.736	13.62	8 351 551	0.25
19	30	1.321	11.29	10 275 350	0.25
20	30	1.028	6.37	11 666 510	0.25
21	30	0.922	7.82	10 464 423	0.25

the initial spatial positions of the particles can be calculated from cosmological parameters. The corresponding initial velocities then follow from the time derivative of the Zel'dovich approximation as:

$$\dot{\mathbf{x}}(t, \mathbf{q}) = \frac{d}{dt} [\mathbf{q} + b(t)\mathbf{p}(\mathbf{q})] = \dot{b}(t)\mathbf{p}(\mathbf{q}) \quad (3.6)$$

3.2 Creating high resolution simulations

The initial conditions used for the simulations run for this thesis were created with a modified version of the GRAFIC2 package by Bertschinger (2001), as described in Penzo et al. (2014). The refinement level was chosen to maintain a roughly constant

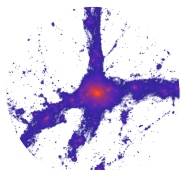


relative resolution per halo, for example, $\sim 10^7$ dark matter particles with particle masses of about $10^5 \text{ h}^{-1}\text{M}_\odot$. This allows reliable resolution of the substructure down to halo masses of $\sim 10^7 \text{ h}^{-1}\text{M}_\odot$.

The halos for refinement were selected from the cosmological boxes from Dutton and Macciò (2014), assuming Planck Cosmology (Planck Collaboration et al. (2014)). The halos were selected according to their concentration parameter, with the aim to have an equal number of high, average and low concentration halos. For these halos, high resolution initial conditions were created. First, all particles within three to five times the virial radius at $z = 0$ were identified by their ID. The particle IDs are constant throughout entire simulations, as dark matter particles can not be created or destroyed. With these IDs, the particles can be identified on the initial Cartesian grid. The next step was to reenter the simulation at the appropriate region, and each of the particles was split up into N_{HR}^3 particles, equally distributed in a cube of side length equal to the inter particle distance of the “parent” particles, centred on the “parent” particle position. Next, regions were created with intermediate resolution particles. In this case, the particles were split into N_{MR}^3 particles in the same process as described above. Depending on the zooming factor, there were several such intermediate regions with increasing particle mass and inter particle distance and thus decreasing resolution. Figure 3.1 shows a sketch of this process. Since in this thesis, the goal was to reach nearly the same relative resolution for all halos ($\sim 10^7$ dark matter particles per halo), the zooming factors depended on the halo mass and box size such that for each halo a different zooming factor was used. Detailed information on the zoomed halos can be found in Table 3.1.

The initial conditions created this way were evolved with PKDGRAV2 (Stadel 2013) up to redshift $z = 0$ and halos were identified using the *AMIGA halo finder* (AHF). This halo finder is able to deal with different particle masses and variable resolution levels, as well as to identify substructure (Knollmann and Knebe 2009).

In the high resolution runs, the same halo as that identified in the low resolution run had to be identified. Typically it was the one with the highest number of particles, but not necessarily the most massive one. It was then necessary to check whether there were high mass or intermediate mass (lower resolution) particles in the virial radius or the region of interest of the halo. These particles can alter the outcome of a simulation drastically, and if there are some of them in the region of interest of the high resolution halo, one has to choose a bigger region around the low resolution halo for refinement and rerun the whole simulation. Figure 3.2 shows a visual impression of a sample IC setup for a high resolution run.



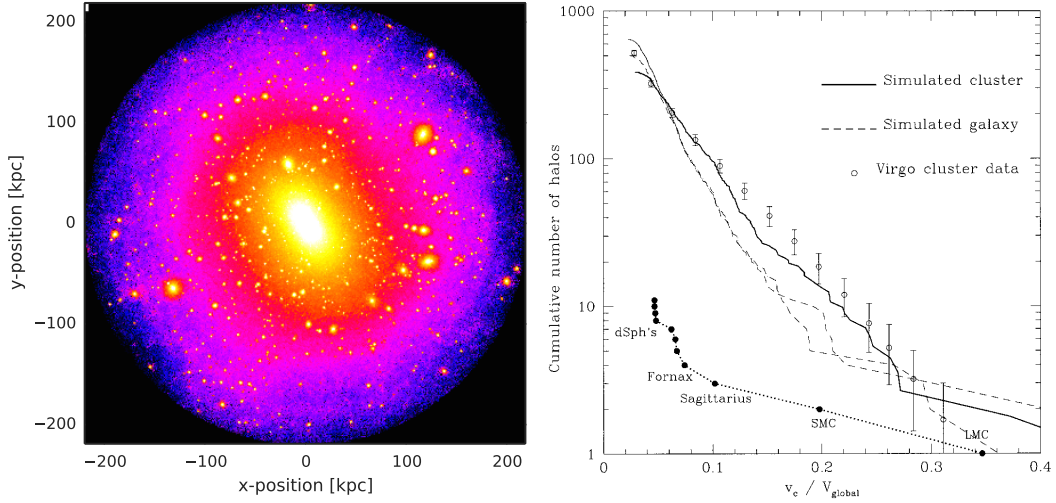
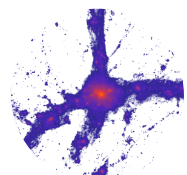


Figure 3.3: *Left panel:* A density plot of the high resolution Milky Way mass-like dark matter halo, revealing hundreds of resolved sub-halos. *Right panel:* Cumulative numbers of the Milky Way substructure, the Virgo Cluster substructure and the simulated model substructure, with the same mass scale for comparison (Moore et al. 1999).

3.3 CDM Substructure Problem

3.3.1 Missing Satellite Problem

Numerical simulations of dark matter halos, which are pure N -body simulations, are in excellent agreement with observations on cluster scales. The simulations predict lots of substructure that can be matched to the cluster galaxies. But due to the nearly scale-free nature of structure formation in the Λ CDM framework, galaxy size dark matter halos also reveal hundreds of sub-halos (see left panel of Fig.: 3.3). There are two discrepancies in this prediction. Firstly, the observed number of satellites around the Milky Way or Andromeda is much smaller than that predicted by numerical dark matter only simulations (Moore et al. 1999; Klypin et al. 1999; Diemand et al. 2008). Secondly, Λ CDM predicts a scale-free or self-similar mass function for the substructure in dark matter halos of different masses, while observed luminosity functions are strongly mass dependent (see right panel of Fig.: 3.3). These discrepancies result in the so-called *Missing Satellite Problem*. This problem manifests itself in dark matter only simulations that do not include baryonic physics. Several possible methods have been proposed to solve this problem. For example, inclusion of baryonic physics in the simulations could alleviate the *Missing Satellite Problem* (Bullock et al. 2000; Macciò 2010).



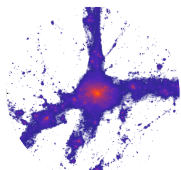
3.3.2 Suppression of Structure formation on small scales

The substructure problem associated with CDM can be alleviated either by the inclusion of baryonic physics in the simulations or by introducing alternative particles, in the form of so-called warm dark matter (WDM). The particles of this species are much lighter (several keV) than the cold dark matter particles and therefore have non-negligible velocity dispersion. Hence they are able to escape from primordial small potential wells and thus wash out density perturbations. This leads to a suppression of the power spectrum on small scales and the number of sub halos is reduced compared to CDM (Colín et al. 2000; Schneider et al. 2012; Lovell et al. 2012; Anderhalden et al. 2012).

Another potential solution to the substructure problem is the suppression of star formation in lower mass dark matter halos. There have been two possible solutions of this kind suggested. Firstly, in low mass halos, supernova feedback can cause the ejection of cold gas (Dekel and Silk 1986; Klypin et al. 1999), preventing these halos from forming luminous dwarf galaxies. Secondly, the ionizing radiation field after reionization keeps the gas from cooling into low mass halos, preventing star formation in low mass environments (Rees 1986; Thoul and Weinberg 1996). The heating of the ionizing background provides additional pressure and keeps the gas from falling into these small halos and can even evaporate existing virialized objects (Barkana and Loeb 1999). These solutions assume the underlying substructure of Λ CDM to be correct, and therefore predict lots of dark or ultra faint satellites, because for the supernova feedback mechanism at least some amount of star formation must have occurred. Through the inclusion of baryonic physics, it can be shown that galaxy formation is strongly suppressed in dark matter halos below $3 \cdot 10^9 M_\odot$ (Sawala et al. 2014).

3.3.3 Cusp-Core Problem

Another discrepancy between observations and the predictions from dark matter only simulations on small scales is the so called *Cusp-Core Problem*. It describes the difference between observed density profiles in dwarf galaxies and the ones in simulated dark matter halos of same mass scale. Dwarf galaxy density profiles possess a core, whereas dark matter only simulations predict the dark matter density profile to be well described by a universal cuspy profile (NFW profile, Navarro et al. (1997); Moore (1994); Diemand et al. (2005); Macciò et al. (2012a)). As in the case of the *Missing Satellite Problem*, the inclusion of baryonic physics might be a solution to this problem. Baryons are subject to many more interactions than dark matter particles, which leads to much greater variation in the baryonic density



profile, due to responses to feedback processes, such as gas outflows after star formation or heating due to AGN feedback. The gravitational interaction of dark matter and baryons is then able to alter the density profile of the underlying dark matter distribution and leads to a cored profile (Flores and Primack 1994; de Blok and Bosma 2002; Mashchenko et al. 2008; Governato et al. 2012; Macciò et al. 2012b).

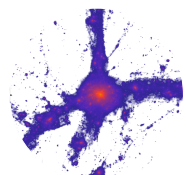
3.3.4 Observational detection biases

The substructure problem is not just a result of incorrect theoretical descriptions, but is also partly induced by the incompleteness and biases in observations of dwarf galaxies in the local group due to detection limits. Besides theoretical issues, the *Missing Satellite Problem* can be at least partly interpreted as a consequence of incomplete dwarf galaxy samples due to the following observational problems (see Bullock (2010) and also references therein):

Surface Brightness Limits : Most of the known dwarf galaxies have very low surface brightnesses, which lie close to the current detection limits. Therefore one expects further dwarf galaxies to easily fall below the threshold of current surveys, leading to the non-detection of a significant number of satellites.

Sky Coverage : The current dwarf galaxy surveys are incomplete. They only include $\sim 20\%$ of the total sky, which then leads to the conclusion that up to five times more satellites might be discovered if the whole sky were observed. If the dwarf galaxy populations were evenly distributed around the Milky Way or Andromeda, this bias could be accounted for. But as Pawłowski and Kroupa (2014) and Ibata et al. (2013) claimed, the satellite distribution around the Milky Way and Andromeda might be highly anisotropic. This makes an estimation of the sky coverage bias very difficult (see e.g. Fig.: 4.2).

Luminosity Bias : Observations are naturally limited by luminosity, and it is relatively easy to obtain the luminosity limit of a survey. But since dwarf galaxies are also distributed radially around a galaxy with unknown distance from the host, it is difficult to estimate a correction factor for this bias. Future deeper surveys are required to account for this bias (but see Koposov et al. (2008)).

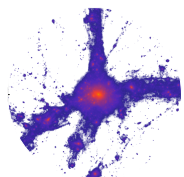


4 Observations and halo selection

Since 1976, when Lynden-Bell (1976) first proposed that Milky Way satellites lie in a plane, a great deal of progress has been made. Further satellites around the Milky Way and especially around its companion Andromeda (M31) have been found (Koch and Grebel 2006; McConnachie and Irwin 2006; Metz et al. 2008; Ibata et al. 2013; Conn et al. 2013). With accurate sky surveys like the Sloan Digital Sky Survey (Abazajian et al. 2009, SDSS) or the Pan-Andromeda Archaeological Survey (McConnachie et al. 2009, PAndAS), many new members could be assigned to the ‘plane of satellites’ and their kinematics could be investigated. The analysis of these kinematics recently revealed that among the 27 satellites found around Andromeda in the PAndAS survey, 15 lie within a thin plane of (12.6 ± 0.6) kpc (Ibata et al. 2013; Conn et al. 2013). Furthermore, Ibata et al. (2013) estimated from line-of-sight velocity measurements that 13 out of the 15 satellites in the plane seem to co-rotate. This kind of spatial and kinematic alignment is not easily found in Cold Dark Matter simulations, and raised the question once again of whether Cold Dark Matter is the correct cosmological model (Kroupa et al. 2005, 2012; Pawłowski et al. 2014; Ibata et al. 2014). In this chapter, recent observations of satellite planes around Andromeda and the Milky Way are presented, the detection methods for the M31 plane are discussed, and the main halo selection as well as the methodology used to find planes of sub-halos in the simulations are introduced.

4.1 Observed Planes of Satellites

The detection methods of planes of satellite galaxies around our own Galaxy and around Andromeda are totally different in nature. While we can observe Andromeda from the outside, nearly edge-on, our position in the Milky Way makes it impossible to get such a view of our own Galaxy. The detectable planes are therefore also very different in nature. The plane of satellites around Andromeda is seen nearly edge on, and line-of-sight velocity information for the motion in the plane can thus be obtained. Additionally, distance information is available to calculate the relative distances of the satellites to Andromeda and get a three-dimensional picture of the plane. For the Milky Way, such information is not always available, and only



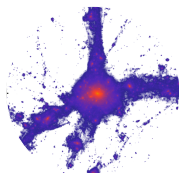
proper motion measurements (for only some of the satellites), positions on the sky and distances can be obtained. From these values, the plane can be found by the clustering of angular momentum vectors around the orbital pole of the plane (compare Fig.: 4.1). A detailed view on the distribution of satellites around the Milky Way and Andromeda will be given below.

4.1.1 Milky Way

The Milky Way plane is much harder to define than the plane around Andromeda. So far, 27 satellites of our own Galaxy are known (Pawlowski and Kroupa 2014), and for 11 of them, proper motion measurements are available. For 8 out of these 11 satellites, Pawlowski et al. (2013) were able to obtain an average orbital pole leading to a plane of thickness (rms value) 19.6 kpc and a parallel root-mean-square extension of 129.5 kpc (Pawlowski et al. 2014). They find that at least 6 orbital poles are closely aligned with the average orbital pole, and thus the satellites seem to co-rotate the Milky Way on a similar orbit. However, considering the context of the availability of data (with proper motion values available for 11 out of 27 satellites) and the fact that only 6 out of the 27 satellites seem to align spatially and kinematically, this is a weak statement. But nevertheless, the orbital poles seem to align with some of the known stellar streams around the Milky Way (Pawlowski et al. 2013). Furthermore, more and more planes of satellites are being discovered around other galaxies.

4.1.2 Andromeda - M31

In the case of Andromeda, it is much easier to find the plane of satellites and to determine its characteristics. Ibata et al. (2013) analysed 27 satellites in the Pan-Andromeda Archaeological Survey (McConnachie et al. 2009, PAndAS) and found that 15 of the 27 satellites lay in a thin plane of thickness (12.6 ± 0.6) kpc (Ibata et al. 2013; Conn et al. 2013). Furthermore, using line-of-sight velocities, they reported that 13 of the satellites in the plane co-rotate. The fact that all of the distances were obtained from the same survey makes the distance and thickness estimates more reliable. Additionally, the view of the galaxy from the outside makes it much easier to identify the planar structure. Moreover Ibata et al. (2013) excluded nine known satellites (two that lie inside the PAndAS field, and seven that lie outside, see Fig.: 4.2, left panel), either because they are too close to Andromeda's disk or because they are not part of the survey area of PAndAS. Four clearly lie outside the plane and do not contribute to it. Five of them, however, are located such that they may belong to the plane. Since these satellites were not included



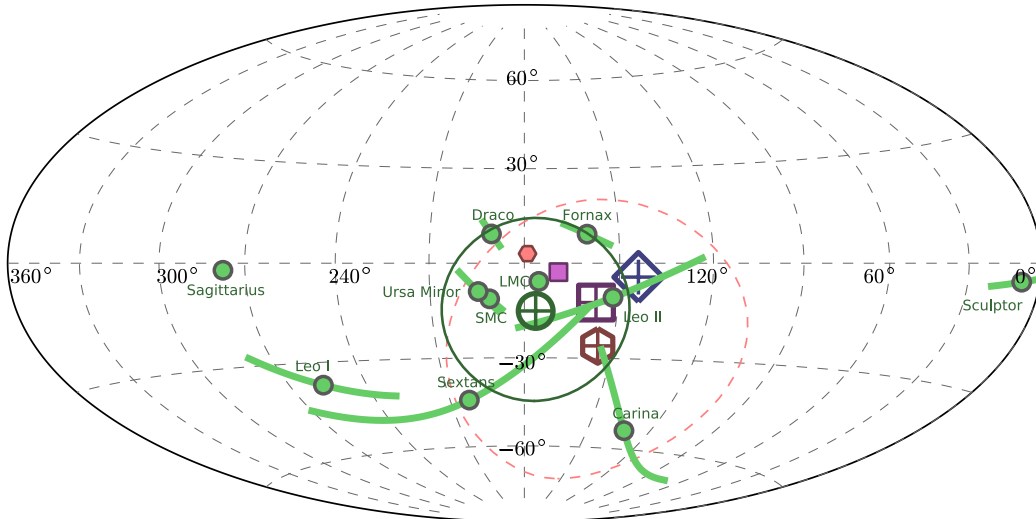
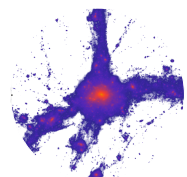


Figure 4.1: An all-sky plot of the orbital poles of the MW satellite galaxies (green dots) in Galactic longitude l and Galactic latitude b in an Aitoff projection. The measurement uncertainties of the orbital pole directions are indicated by the green great-circle segments. The average direction of the eight most concentrated orbital poles is indicated by the dark green circle with a central cross at $(l, b) = (176.4^\circ, -15.0^\circ)$, and the surrounding solid green circle is the size of the spherical standard distance ($\Delta_{\text{sph}} = 29.3^\circ$) of the eight contributing poles around this direction. The magenta square gives the direction of the normal vector to the plane fitted to the positions of the 11 brightest satellite galaxies. The blue diamond indicates the direction of the normal to the plane fitted to all Globular Clusters. The red hexagon shows the average direction of the normal vectors to all 14 streams in the MW halo analyzed for this plot, the dashed red circle is the size of their spherical standard distances of $\Delta_{\text{sph}} = 46^\circ$ and the small filled hexagon indicates the normal direction to the Magellanic Stream. The small filled square denotes the normal direction to the plane fitted to the positions of all MW satellites with the exception of three outliers. The plane normal directions, the average stream normal and the majority of the orbital poles are all concentrated in the centre of the plot, indicating co-orbiting structures, with one satellite on a retrograde orbit (Pawlowski et al. 2013).

in previous analysis we stick to the values calculated by Ibata et al. (2013), but keep in mind that these satellites will alter the root-mean-square thickness and the extension of the plane, as well as the ratio of satellites in the plane to those satellites outside of the plane and the fraction of co-rotating satellites. A visual impression of the plane as it was observed by Ibata et al. (2013) is shown in the left panel of Fig.: 4.2. The blue dots represent satellites outside of the plane while



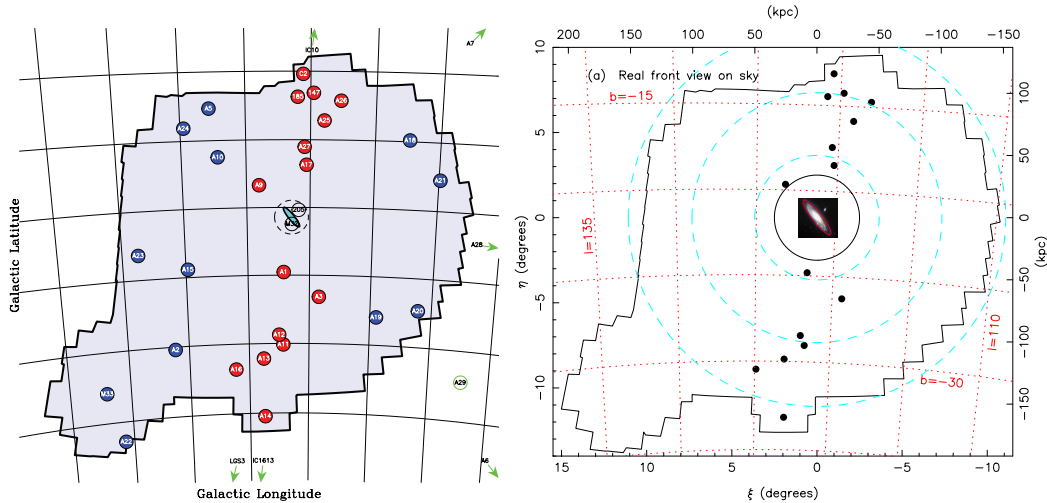
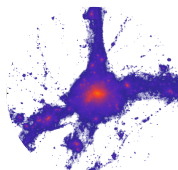


Figure 4.2: *Left panel:* Satellites as observed in the PAndAS field of view around Andromeda (Ibata et al. 2013), red satellites are in the plane, blue satellites are outside of the plane. Arrows indicate further known satellites that are not in the PAndAS field. *Right panel:* The plane as observed around Andromeda by Ibata et al. (2014) with blue dashed circles showing distances of 50, 100 and 150 kpc from the center of Andromeda. The irregularly shaped region in both panels represents the PAndAS survey area.

red ones show the satellites in the plane. A visual impression of the extension of the plane is shown in the right panel of Figure 4.2 with blue dashed circles indicating distances of 50, 100 and 150 kpc from the center of Andromeda. The selection of 15 satellites used to make up the plane is somewhat arbitrary and was chosen because this number minimizes the root-mean-square thickness of the plane. After specifying the plane and its constituents, the kinematics were investigated, revealing kinematical coherence. A detailed description of the selection process can be found in Conn et al. (2013).

4.2 Main Halo Selection

The dark matter halos re-simulated in this thesis were selected from four cosmological boxes of side length 30, 45, 60 and $80 h^{-1} M_{\odot}$ from Dutton and Macciò (2014), who used cosmological parameters from the Planck Collaboration (2014): $\Omega_m = 0.3175$, $h = 0.671$, $\sigma_8 = 0.8344$, $n = 0.9624$. From these boxes, Andromeda-like mass halos ($5 \times 10^{11} < M_{200}/[h^{-1} M_{\odot}] < 1.5 \times 10^{12}$) were selected, where the halo mass was defined with respect to 200 times the critical density of the



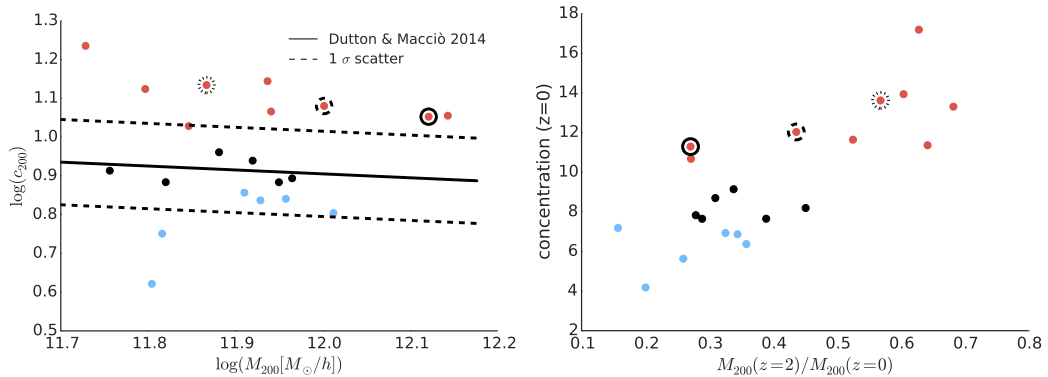
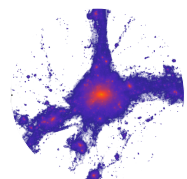


Figure 4.3: *Left panel:* The concentration mass relation. This diagram shows the concentration as a function of mass of the high resolution halos. The solid line is the average relation from Dutton and Macciò (2014). The dashed line indicates the 1σ scatter of this relation. Colour coding shows the division of the halos into high, average and low concentration. *Right panel:* Mass growth vs. concentration. The plot shows the concentration at $z = 0$ as a function of mass at $z = 2$ in terms of the present day mass. Rapidly growing halos (late forming) are located on the left, while slowly growing halos (early forming) are located on the right. The color coding shows the division of the halos into high, average and low concentrations. The halos with satellite planes coming closest to the values of Andromeda are marked by black circles. The dotted one is *halo A*, the dashed one is *halo B* and the solid circle marks *halo C*.

universe. Aside from halo mass, the only other selection criteria for the objects was the concentration, which is a proxy for halo formation time (Wechsler et al. 2002). The right panel of Figure 4.3 shows the concentration at $z = 0$ as a function of the mass growth since $z = 2$. The clear correlation validates the approach of using the concentration as a first proxy for the halo formation time.

The reasoning behind such a choice is that, at a fixed mass at the present time, early forming halos are more likely to form at the nodes of intersections of a few filaments of the cosmic web, while typical halos tend to reside inside such filaments (Dekel et al. 2009). One then might expect that, rarely, early forming halos would accrete satellites from a few streams that are narrow compared to the halo size, while typical halos accrete satellites from a wide angle in a practically spherical pattern.

In the left panel of Figure 4.3 the concentration-mass relation of the high resolution halos is shown. Here the concentration is defined as $c_{200} = R_{200}/r_{-2}$, where R_{200} is the virial radius, and r_{-2} is the radius where the logarithmic slope of the



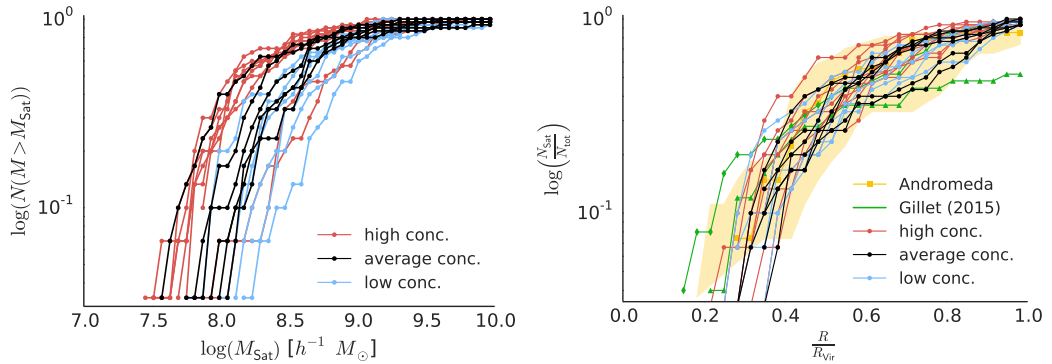


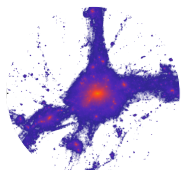
Figure 4.4: *Left panel:* The present day cumulative mass function of the 30 most massive satellites at the infall time for every host halo in the sample. The differences in masses between the high and low concentration halos show the effect of stripping due to the earlier accretion of satellites in high concentration halos. *Right panel:* The present day cumulative radial distribution of the 30 most massive satellites at the infall time for every host halo in the sample. The yellow line indicates the cumulative radial distribution of the satellites around Andromeda (assumed $R_{\text{vir}} = 250$ kpc). The shaded yellow area marks the measurement uncertainty by using the maximal and minimal radius of every satellites respectively. The green lines indicate the two Andromeda analogues from Gillet et al. (2015).

density profile is -2 . A roughly equal number of high (red points), average (black points) and low (blue points) concentration halos (see Figure 4.3) was selected.

The solid line is the power law fit from Dutton and Macciò (2014), while the dashed ones show the 1σ intrinsic scatter of 0.11 dex around the mean. The high concentration halos have on average an offset of about 2σ from the mean relation. This means these halos are the rarest 2.3% of the whole population. For a random sample of halos, it would thus require ~ 40 simulations to recover such rare halos. This helps to explain why previous high resolution simulations were unable to reproduce the observed properties of the satellite distribution around the Andromeda galaxy: they simply did not sample enough halos to find the rarer earliest forming ones.

4.3 Satellite Selection

These high resolution simulations reveal hundreds of resolved sub-halos (compare Figure 5.1), which have to be matched to actual luminous galaxies. Galaxy formation models robustly predict the luminous sub-halos to be the ones that are most massive at the infall times (Kravtsov et al. 2004; Conroy et al. 2006; Vale and Ostriker 2006).

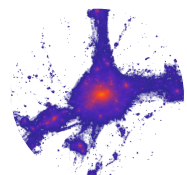


Thus, a sample of the 30 most massive subhalos at the time of accretion was chosen, where the analysis was restricted to subhalos within the virial radius of the host halo (~ 200 kpc).

Although observations around Andromeda use a special selection function given by the peculiarities of the Pan-Andromeda Archaeological Survey (McConnachie et al. 2009, PAndAS), for this thesis it was decided not to reproduce the selection function for a number of reasons. Firstly, it requires surface-brightness information that is not available in these (dark matter only) simulations. Secondly, the PAndAS footprint is unique to the Andromeda galaxy, being non-circular, and including a region around its most massive satellite M33. Thus it would not make sense to apply the same footprint to a cosmological simulation. Thirdly, the spatial depth of the survey is somewhat uncertain due to the difficulties in measuring accurate distances to the satellites. Rather, in this thesis simple, reproduceable, and physically motivated selection criteria are chosen. As the satellite population of the most massive sub-halos (at the infall time) are within the $z = 0$ virial radius, R_{vir} is chosen. Choosing satellites within the virial radius leads to a bigger volume ($\approx R_{\text{vir}}^3$) compared to the observations and hence a total of 30 satellites instead of 27 are used. Furthermore, there is some arbitrariness in the number of satellites related to Andromeda. As mentioned before, nine known satellites (two that lie inside the PAndAS field, and seven that lie outside) were not considered by Ibata et al. (2013). Nevertheless, for this thesis, different sample sizes of 25, 27 and 30 satellites were tested and no major differences in the plane statistics were found. Therefore, only the results for samples consisting of 30 satellites will be discussed.

Figure 4.4 shows the present day cumulative mass function (left panel) and the cumulative radial distribution (right panel) of the 21 satellite samples together with the observations plotted in yellow. Selection of the 30 most massive satellites at the infall time results in present day satellite samples with masses in the range ($3 \times 10^7 < M_{200}/[h^{-1}M_\odot] < 1 \times 10^{10}$). The separation in the cumulative mass function between the satellite samples of main halos with different concentrations, shown in the left panel of Figure 4.4, with high concentration satellites showing lower masses, is a result of stripping. High concentration halos accrete their satellite samples at earlier times than low concentration halos, which leads to satellites being more stripped in high concentration halos than in low concentration halos.

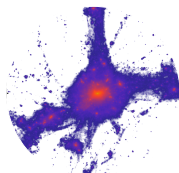
The cumulative radial distribution of satellite samples (right panel of Figure 4.4) reveals that the selection of the 30 most massive satellites at infall time results in satellite samples occupying radii between ($0.2 < R/R_{\text{vir}} < 1$) in good agreement with the observed radial distribution of satellites around Andromeda (shown in yellow). There is no indication that high concentration halos have a different radial distribution, namely a more concentrated distribution of satellites than low



concentration halos or observed satellites (compare right panel of Figure 5.2). Figure 5.2 shows the observed radial distribution of the 27 satellites around Andromeda with a yellow line. The yellow shaded area marks a nominal uncertainty range calculated by taking the maximum and minimum radius for every satellite given by its measurement uncertainties. For Andromeda a virial radius of $R_{\text{vir}} = 250 \text{ kpc}$ was assumed. Inclusion of two satellites at radii of about $r \sim 400 \text{ kpc}$ into the observational sample leads to the fact that the cumulative radial distribution is not equal to unity at $R/R_{\text{vir}} = 1$. In green the radial distribution of the 25 satellites of the two Andromeda analogues from Gillet et al. (2015) are shown. The radial distribution of their satellite sample is, although only 25 satellites are considered, comparable to the sample of this work. Interestingly one of their simulation is a bit more concentrated than the ones done for this work, while the other is far more extended by inclusion of satellites far beyond the virial radius.

4.4 Plane detection and analysis

In this section, the plane finding algorithm used for this work and the measured variables will be described. The plane finding algorithm works by invoking random planes defined by their normal vector. All planes include the center of the main halo. To uniformly cover the whole sphere, 100,000 random planes are generated with a fixed thickness of $2\Delta = 30 \text{ kpc h}^{-1}$, where only half of the sphere actually has to be considered, since plane normal vectors are symmetric. After specifying a plane, the distance of every satellite to this plane is calculated. A satellite is considered to lie in the plane if its distance to the plane is smaller than Δ . For each plane, the number of satellites in the plane, its root-mean-square thickness Δ_{rms} and its radial extension is calculated. Then, for every number of satellites in the plane, the one that is thinnest and richest is chosen to be analyzed for the kinematics (further details on the plane finding algorithm can also be found in Gillet et al. (2015); Ibata et al. (2014); Conn et al. (2013)). For these planes, the line-of-sight velocity of the satellites in the plane in edge-on view is calculated, and that information is used to infer the number of co-rotating satellites.



5 Results

This chapter contains the analysis of the planes of satellites found in the 21 high-resolution “zoom-in” dark matter only simulations. The simulations were intended to resolve a sufficient number of subhalos to make planes of satellites identifiable. The main halos for re-simulation were selected from large-volume simulations run by Dutton and Macciò (2014), in such a way that an almost equal number of high, average and low concentration halos were chosen (for details see 3 and 4.2).

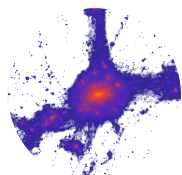
The substructure within a high-resolution region was identified using the *Amiga Halo Finder* (Knollmann and Knebe 2009, AHF), which is capable of finding subhalos as well as dealing with different particle masses. At $z = 0$, a plane finding algorithm (as described in section 4.4) was applied to the 30 most massive satellites at the infall time, with the goal of identifying planes of satellites similar to the observed ones. The kinematics of the simulated planes of satellites were investigated and compared to those of the observed satellite planes. As a further step, the formation scenario of the planes was analysed.

One particularly interesting feature is the visual impression of the planes found in the simulations. The upper left panel of Figure 5.1 shows a density plot of the halo coming closest to the parameters observed for Andromeda

$$\begin{aligned} \text{Simulation : } & N_{\text{in}} = 15, N_{\text{corot}} = 13, \Delta_{\text{rms}} = 12.9 \text{ kpc} \\ \text{Andromeda : } & N_{\text{in}} = 15, N_{\text{corot}} = 13, \Delta_{\text{rms}} = (12.6 \pm 0.6) \text{ kpc} \end{aligned} \quad (5.1)$$

The upper right panel shows the same plot, but it now indicates all 30 of the most massive satellites at the infall time used for the plane finding algorithm with black circles. The lower left panel shows the satellites in the plane as green circles and the ones outside of the plane again as black circles. Finally, the lower right panel shows the kinematics of the plane by color-coding the sign of the line-of-sight velocity with red and blue.

In this section, all of the simulations will be investigated for such planes, and the dependence of plane parameters (like the number of satellites in the plane or the plane thickness) on the concentration of the main halo will be shown. In a second step, a detailed kinematic analysis of the planes will be performed, including an investigation of the co-rotation fraction, the lifetime of the plane and the dependence of the appearance of the plane on the viewing angle.



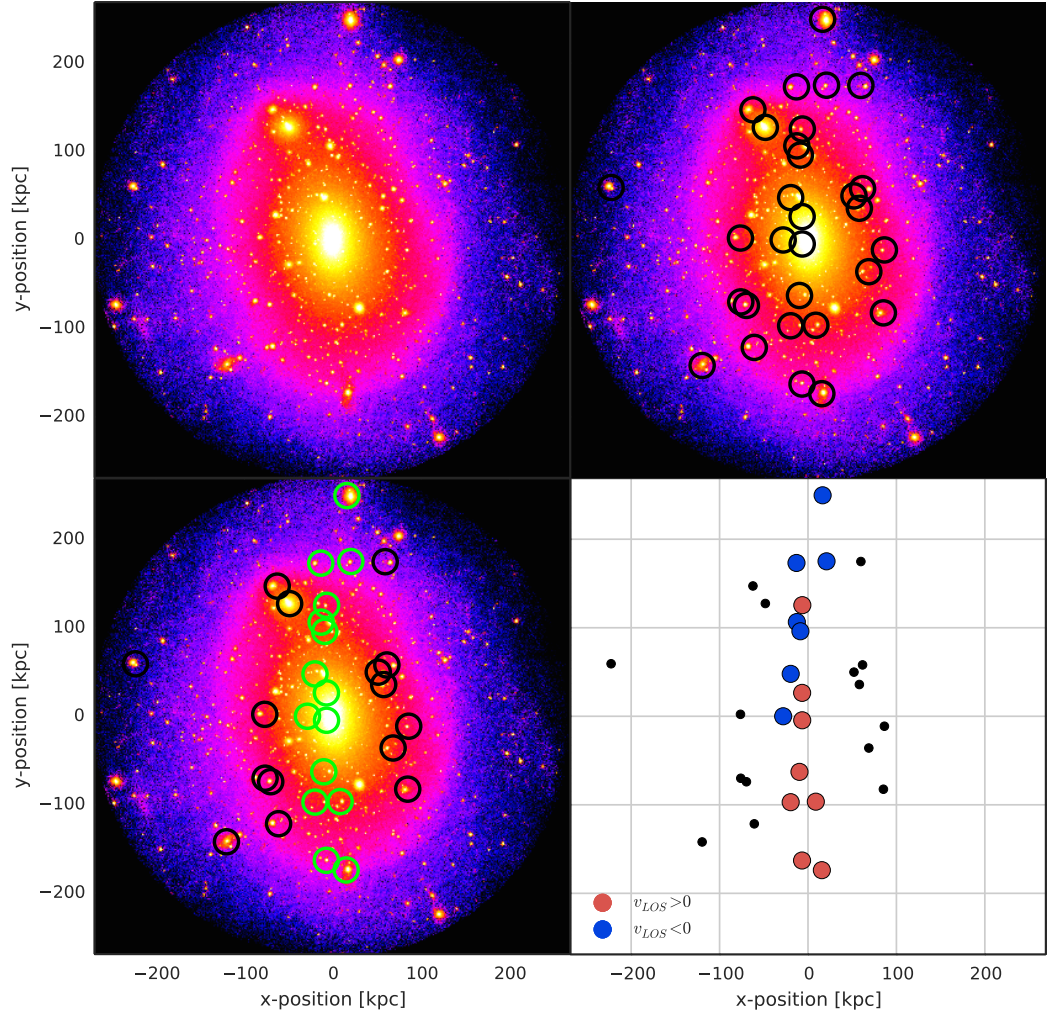
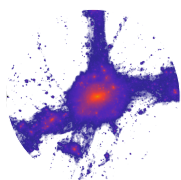


Figure 5.1: A density plot of the plane of satellites with values closest to those of Andromeda. *Upper left panel:* A density plot of the halo, showing hundreds of resolved satellites. *Upper right panel:* A density plot of the same halo, indicating the 30 most massive satellites at the infall time with black circles. *Lower left panel:* Here the plane is highlighted by showing satellites in the plane as green circles and satellites outside of the plane with black circles. *Lower right panel:* Here the kinematics of the plane are shown by the color-coding of the directions of the line-of-sight velocities of satellites in the plane as red and blue dots.



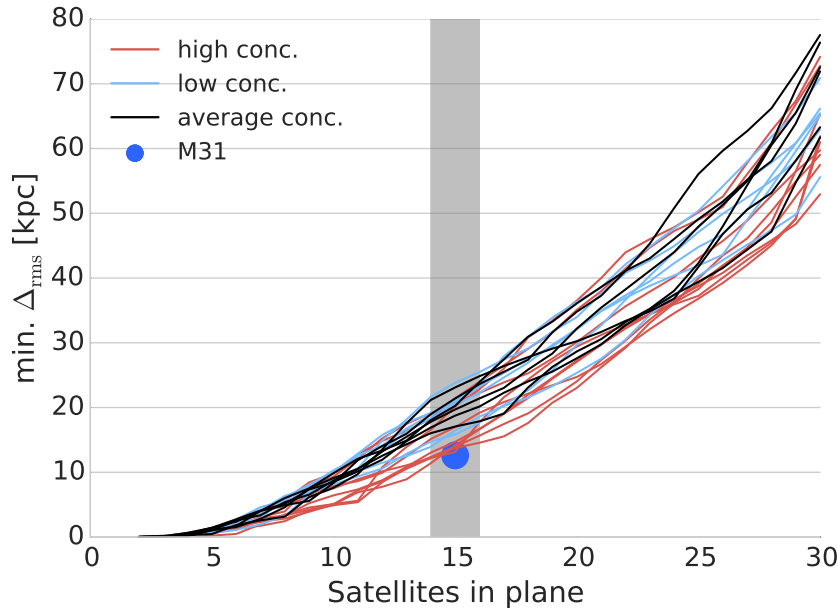
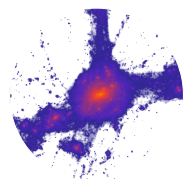


Figure 5.2: The minimal root-mean-square thickness, $\text{min. } \Delta_{\text{rms}}$, of planes as a function of the number of satellites in the plane. Each line represents a different dark matter halo. *Red* lines show high concentration halos, *blue* lines show low concentration halos and *black* lines show average concentration halos. The thinnest planes occur in the highest concentration halos. The *blue dot* shows the rms value of the plane of satellites observed around Andromeda (Ibata et al. 2013; Conn et al. 2013). The *grey area* represents a nominal uncertainty in the number of satellites in the plane around Andromeda of ± 1 .

5.1 Dependence of plane parameters on halo concentration

As the first step in analysing the planes of satellites generated in these high-resolution simulations, the dependence of the plane parameters on the concentration of the main halo was investigated. For this purpose, correlations of the plane thickness, the number of satellites in the plane and the number of co-rotating satellites with the concentration (as a proxy for the formation time) of the host were investigated.



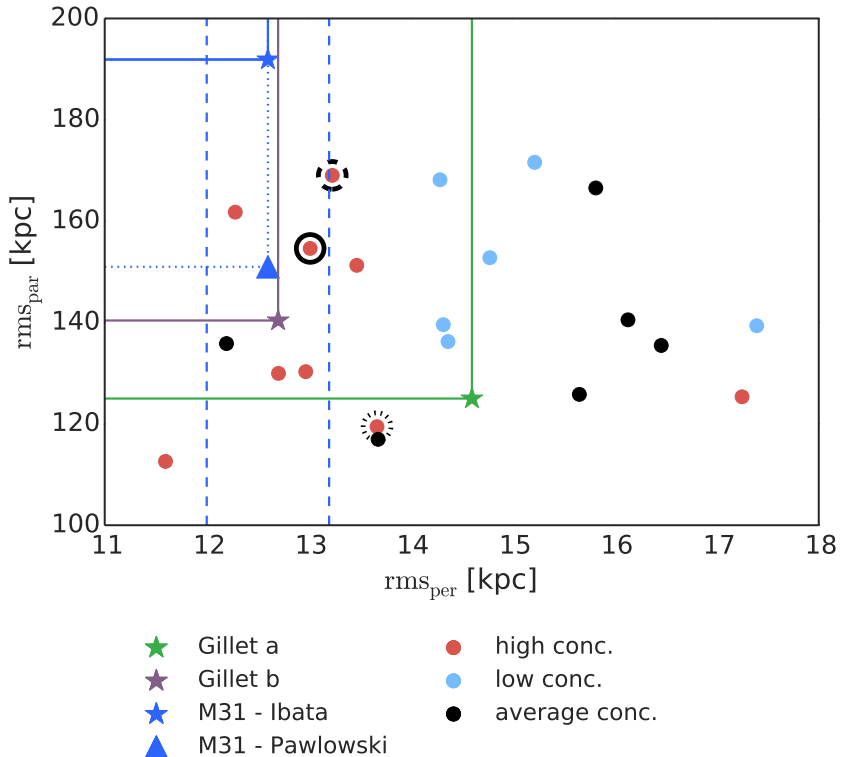
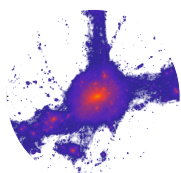


Figure 5.3: The minimal root-mean-square thicknesses parallel and perpendicular to the richest planes found, color-coded by halo concentration. The values from Andromeda are indicated by the *blue triangle* and the *blue star*, with the dashed blue lines indicating the measurement uncertainty of the perpendicular rms value of (12.6 ± 0.6) kpc. The solid blue lines and the blue star show the values calculated by Ibata et al. (2013). The dotted blue lines together with the blue triangle show an estimate of the parallel rms value given by (Pawlowski and Kroupa 2014), while the values obtained by Gillet et al. (2015) for their two Andromeda analogues are plotted in green and purple respectively. The halos with satellite planes with the closest number of members to that of Andromeda (15 satellites in the plane) are marked with black circles. The dotted one is *halo A*, the dashed one is *halo B* and the solid circle marks *halo C*.

5.1.1 Plane thickness vs halo concentration

To analyse the dependence of plane thickness on the concentration of the main halo and hence on the formation time of the host, the minimum root-mean-square thickness of the plane, Δ_{rms} , for every given number of satellites in the plane was calculated. Δ_{rms} is the the root-mean-square value of the distance of the satellites



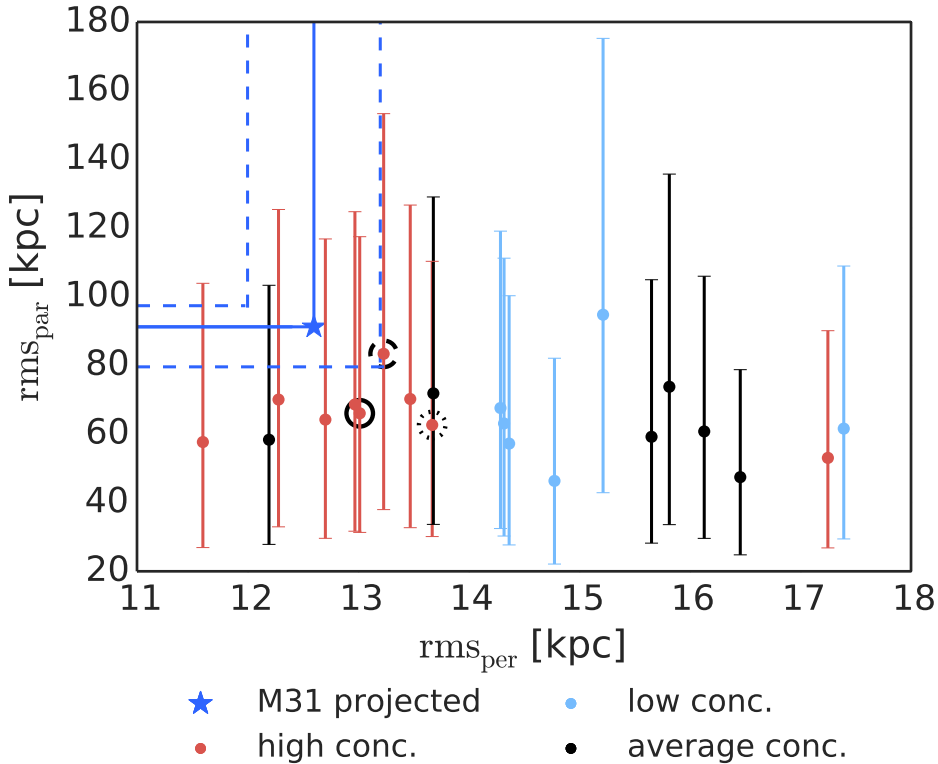
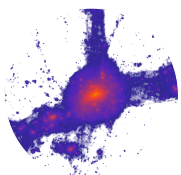


Figure 5.4: The projected 2 dimensional root-mean-square thickness parallel and perpendicular to the richest plane found, color coded by halo concentration. The value for Andromeda is indicated by the *blue star* where the dashed blue lines indicate the measurement uncertainties, for the perpendicular rms value this is given by (12.6 ± 0.6) kpc (Ibata et al. 2013) and for the parallel one the uncertainty is given by calculating the projected rms value with the upper and lower limit of the radius of each satellite. The error bars of the simulated satellite planes indicate the range of possible values if different viewing angles for the projection of the edge-on plane are chosen. The halos with satellite planes coming closest in number of members to the values of Andromeda (15 satellites in plane) are marked by black circles. The dotted one is *halo A*, the dashed one is *halo B* and the solid circle marks *halo C*.

perpendicular to the plane. Figure 5.2 shows the plane thicknesses as a function of the number of satellites in the plane, with lines color-coded according to the halo concentration. There is a clear dependence of the plane thickness on the concentration of the halo. The thinnest planes are only found to be associated with the highest concentration (red lines) halos, and hence the earliest forming halos.



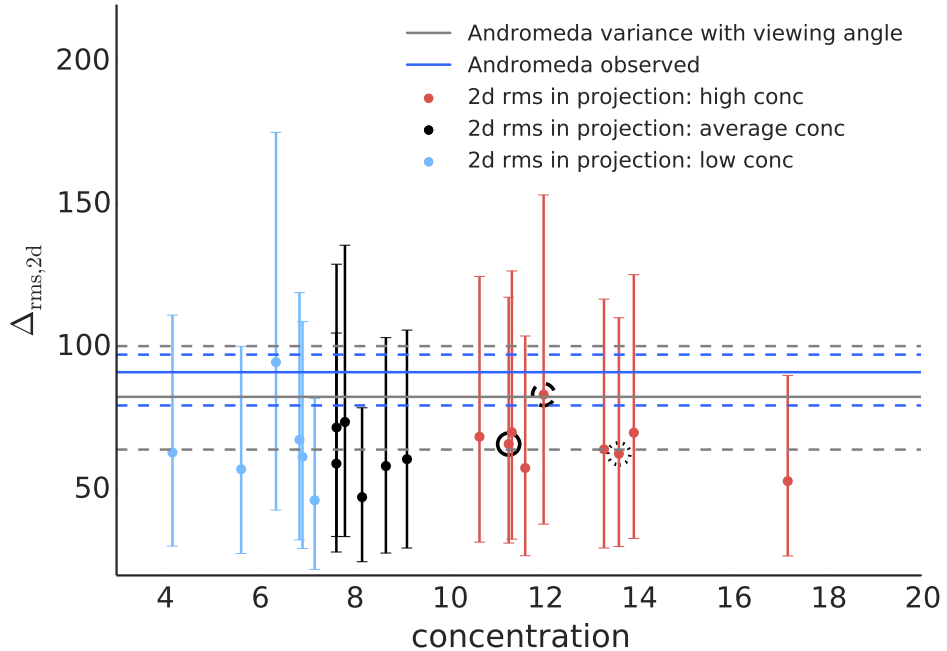
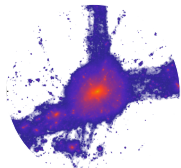


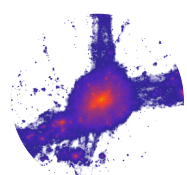
Figure 5.5: The projected 2-dimensional root-mean-square thickness parallel to the richest plane found as a function of halo concentration. The value for Andromeda is indicated by the *blue line* where the dashed blue lines indicate the uncertainty from calculating the projected rms value with the upper and lower limit of the radius of each satellite. The error bars of the simulated satellite planes indicate the range of possible values if different viewing angles for the projection of the edge-on plane are chosen. The grey line together with the dashed grey line shows the mean value and the possible range of values for the projected 2-dimensional rms value parallel to the plane if different viewing angles for the projections are used partially respecting the spatial selection function of the PandAS by excluding satellites with projected radius greater than 160 kpc. The halos with satellite planes coming closest in number of members to the values of Andromeda (15 satellites in plane) are marked by black circles. The dotted one is the *halo A*, the dashed one is the *emphhalo B* and the solid circle marks the *halo C*.

Furthermore, only high concentration halos have planes as thin as those observed in Andromeda (assuming 15 members). The smooth relation between plane thickness and the number of satellites in the plane suggests that there is an arbitrariness in the number of satellites chosen to be in the plane. There is no clear evidence of two distinct spatial structures, such as a planar and spherical distribution of satellites. It is worth noting that an investigation of the satellite distribution does not reveal a more concentrated satellite distribution in high concentration halos, which might



trivially explain the dependence of plane thickness on the concentration that is found (see also Figure 4.4). Selected subhalo samples of low and high concentration halos show the same radial root-mean-square value. This can be seen from Figure 5.3 where a comparison of the root-mean-square thickness of the plane with its parallel root-mean-square value, calculated as the rms of the radial distances to the halo center as projected onto the plane, is shown. The corresponding value for Andromeda is indicated by a blue solid line and a blue star with dashed lines indicating the measurement uncertainty. The value estimated by Pawlowski and Kroupa (2014) for the parallel rms of the Andromeda plane without the furthest satellite AndXXVII ($r > 400$ kpc) is shown as a blue dotted line together with a blue triangle to give an impression of the uncertainty of the parallel rms value. Values for the Andromeda analogues of Gillet et al. (2015) are shown as green and purple lines.

Our plane samples have comparable values to the planes found by Gillet et al. (2015). This plot shows no dependence of the radial root-mean-square value on concentration, but the dependence of perpendicular root-mean-square thickness on concentration found in Figure 5.2 is confirmed. Only high concentration halos show planes with the lowest root-mean-square thickness. One clearly sees that these planes do not show the same high radial root-mean-square value as observed around Andromeda. This is no major problem since the root-mean-square value can be biased by outliers such as the satellite AndXXVII of Andromeda with radial distance further away from the center of Andromeda than 400 kpc (larger than the virial radius of Andromeda and the one of the simulated halos). The mean radius of satellites around Andromeda is about 150 kpc. Therefore, and because it is the value which is actually observed, it is better to compare the projected two-dimensional rms value parallel to the plane in edge-on view. This was done in Figure 5.4 and Figure 5.5. Figure 5.4 shows the projected 2-dimensional root-mean-square thickness parallel and perpendicular to the richest planes found. The values of planes for individual halos are color-coded by halo concentration with high concentration halos shown in red, average ones in black and low concentration halos in blue. The value for the observed plane around Andromeda is indicated by the blue star with dashed blue lines indicating the measurement uncertainties. For the perpendicular rms value this is given by the measurement uncertainties of $\Delta_{\text{rms}} = (12.6 \pm 0.6)$ kpc (Ibata et al. 2013) and for the parallel one the uncertainty is given by calculating the projected rms value with the upper and lower bounds of the radius of each satellite obtained from the measurement uncertainties of the radius. The error bars of the simulated satellite planes indicate the range of possible values if different viewing angles for the projection of the edge-on plane are chosen. In comparison to the radial root-mean-square value obtained for the satellites in the plane shown in Figure 5.3



the values for the projected planes are in better agreement with the observed value and most of the high concentration halos are consistent with the observed value. Furthermore when comparing the simulations to the observations one has to keep in mind that for the observations the satellites with projected radius smaller than 34 kpc are removed. This selection biases the projected root-mean-square value of the observations high compared to the simulations where this selection was not applied for several reasons. The most important reasons is that if this selection criteria was used for the simulations one would have to correct for every viewing angle the number of the 30 most massive satellites since some would be excluded. Instead of applying the same exclusion criteria for the simulations the observed distribution of satellites was used to estimate the projected root-mean-square value parallel to the plane if the viewing angle in edge-on view is altered without excluding satellites projected into the innermost 34 kpc. Since the observations also include satellites obviously outside the virial radius a cut for a projected outermost radius of 160 kpc adopted from the PAndAS footprint was set. The result of this analysis is shown in Figure 5.5 where the projected 2-dimensional root-mean-square thickness parallel to the plane as a function of halo concentration for the simulations is shown. The grey line together with the dashed grey line shows the mean value and the possible range of values for the projected 2-dimensional rms value parallel to the plane if different viewing angles in edge-on view are used for the projections of the observed satellite distribution excluding satellites with projected radius greater than 160 kpc. For comparison the value observed for Andromeda is indicated by the *blue line* with the dashed blue lines showing the uncertainty from calculating the projected rms value with the upper and lower limits of the radius of each satellite obtained from their measurement uncertainties. The observed value (blue line) and the estimated mean value (grey line) by using different viewing angles are in full agreement within their uncertainties. The error bars of the simulated satellite planes again indicate the range of possible values if different viewing angles for the projection of the edge-on plane are chosen. For this analysis the simulations are in even better agreement with the observations although showing a systematical bias to lower parallel rms values compared to the observations. This could be due to several reasons, for example does a lower virial mass of the simulations compared to the observations bias them low (see also subsection 5.4.2 for the impact of different definitions for dark matter halo border). Furthermore, the observed satellite sample already suffers from a bias towards a more extended satellite sample due to the PAndAS selection function. Nevertheless, given the huge scatter in projected parallel root-mean-square thickness in the simulations, they are in good agreement to both, the observed 2-dimensional rms value and the one estimated by using different viewing angles.



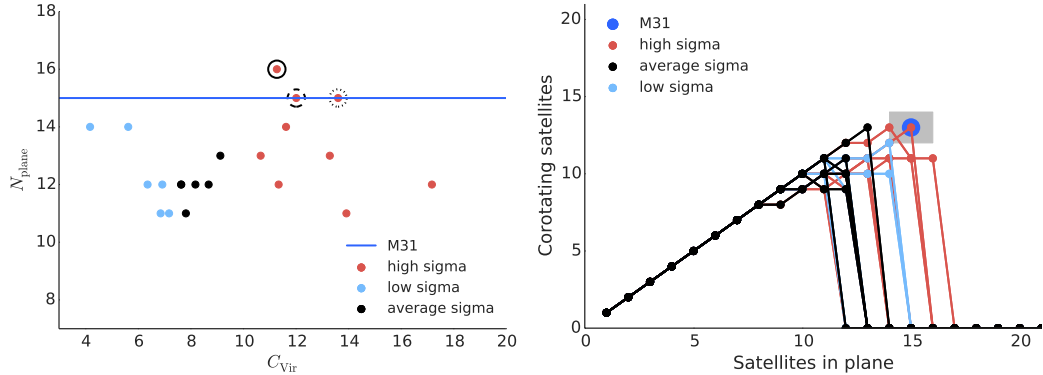
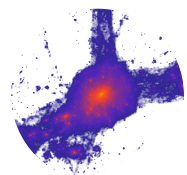


Figure 5.6: *Left panel:* The maximum number of satellites in the plane as a function of the concentration. The color-coding divides the halos into high (red), average (black) and low (blue) concentration halos. The *blue line* shows the value obtained with 15 satellites in the plane for Andromeda. The halos with satellite planes coming closest to the values of Andromeda are marked with black circles. The dotted one is *halo A*, the dashed one is *halo B* and the solid circle marks *halo C*. *Right panel:* The maximum number of co-rotating satellites vs. the number of satellites in the plane, color-coded by concentration. The blue dot shows the observed values of Andromeda’s plane (15 satellites in the plane, with 13 co-rotating) with a grey shaded area indicating an uncertainty of ± 1 for a satellite in the plane and ± 1 for a co-rotating satellite.

5.1.2 Number of satellites in plane vs. concentration

For a given number of satellites in a plane, the thickness correlates with the concentration of the main halo. But an interesting question is whether, for a given maximum root-mean-square thickness, the number of satellites in the plane also correlates with the concentration. This can be assessed by specifying a maximum distance of the satellites from the plane of, for example, 22 kpc and searching for the plane that contains the highest number of satellites. The left panel of Figure 5.6 shows the maximum number of satellites in a plane as a function of the concentration. The overall maximum number of satellites in a plane is about 12 to 13, with just three high concentration halos reaching a satellite count in the plane as high as that observed for Andromeda. Furthermore, there is no obvious correlation with halo concentration. But by showing that high concentration halos have the same number of satellites in their planes, this plot strengthens the conclusion drawn from Figure 5.3, namely that high concentration halos have thinner planes. The thinner planes in high concentration halos are not due to a more concentrated satellite distribution nor to a lower number of satellites in the plane. Rather, high



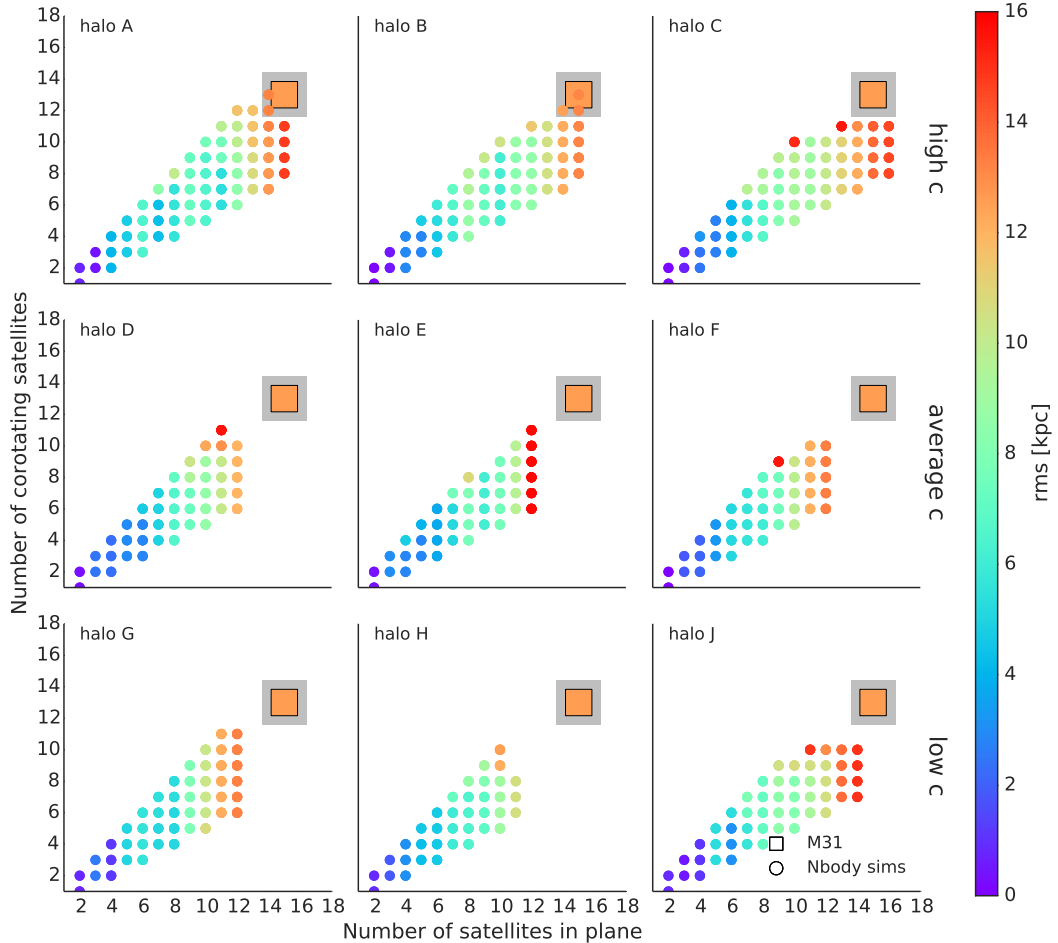
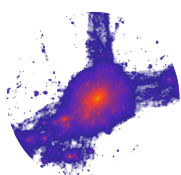


Figure 5.7: The number of co-rotating satellites vs. the number of satellites in the plane for a selection of halos. The points are color coded by the rms thickness (Δ_{rms}) of each plane. The *square* marks the values observed for Andromeda (15 in the plane, 13 co-rotating), where the *grey shaded area* marks the uncertainty of ± 1 for a satellite in the plane and ± 1 for a co-rotating satellite. The *dots* show the values of different planes found per simulated halo. The *top row* shows the high concentration halos, the *middle row* the average concentration halos and the *bottom row* the low concentration halos.

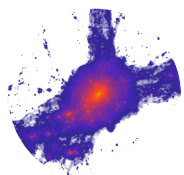


concentration (and thus earlier forming) halos produce genuine thin planes. As a last remark, it might be mentioned that despite the weak dependence of the number of satellites in a plane on the concentration, only high concentration halos seem to produce planes consisting of 15 or more satellites, and thus as rich as the one observed around Andromeda (shown as a blue solid line in Fig.: 5.6, left panel).

In order to investigate the co-rotating of the planes obtained from the plane finding algorithm, for every possible number of satellites in the planes, N_{in} , the number of co-rotating satellites, N_{corot} , was calculated. For this purpose, the sign of the line-of-sight velocity with an edge-on view is used as a proxy for the co-rotating. The result is shown in the right panel of Figure 5.6. When calculating for every possible value for the number of satellites in the plane, the maximum number of co-rotating satellites shows that a fully rotating plane can be obtained for a wide range of planes. Up to values of about 10 satellites in the plane, there are viewing angles from which the plane looks like a fully rotating one (with 100% co-rotating). Interestingly, there is only a slight correlation between the number of co-rotating satellites and the halo concentration, and as was found before, there is no clear dependence of the absolute number of satellites and the number of co-rotating satellites on the halo concentration. There is quite wide scattering among halos of the same concentration, but again, only high concentration halos exhibit the highest numbers of satellites in their planes and the highest number of co-rotating satellites.

To provide a better overview of the possible plane configurations, Figure 5.7 shows the outcome of the plane finding algorithm for a selection of halos of different concentrations with high concentration halos in the upper row, average ones in the middle row and low concentration halos in the bottom row. For every value of the number of satellites in the plane N_{in} , the plots show the number of co-rotating satellites, N_{corot} . Every dot in the plot represents a different plane. The points are color-coded according to the thickness of the plane Δ_{rms} . For all of the halos one can find planes with up to about 10 members that have a 100% co-rotating fraction. Furthermore, one can always find planes with no coherent kinematics (i.e., a co-rotating fraction of 50%). As would be expected, planes with more satellites tend to be thicker. The thickness of the plane, to first order, is also independent of the co-rotating fraction, except for at the highest values of co-rotating fractions.

Figure 5.7 is a remarkable plot summarizing the key parameters of the planes (N_{in} , N_{corot} and the thicknesses Δ_{rms}), and it shows that there is some arbitrariness in selecting the best plane. In particular, it shows that for a given number of satellites in the plane, there is always a plane or viewing angle for which there is no kinematic coherence (50% co-rotating). A more elaborate analysis of the kinematic coherence



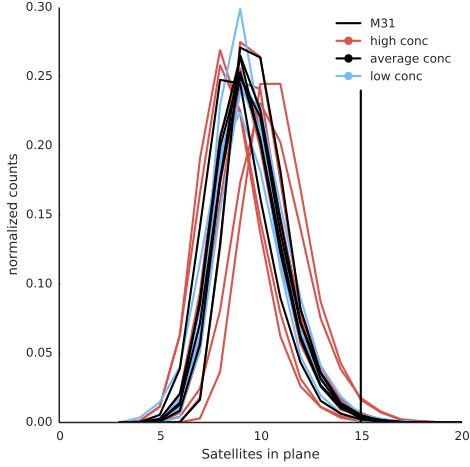
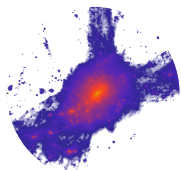


Figure 5.8: The probability density function of the number of satellites in a plane for planes with $\Delta_{\text{rms}} < 22 \text{ kpc}$, color-coded by concentration. *Red lines* show high concentration halos, *black lines* average concentration ones and *blue lines* show low concentration halos. The *solid black line* shows the number of satellites in the plane around Andromeda ($N_{\text{in}} = 15$).

of the richest planes (with the highest number of satellites) will be given in section 5.3.

5.2 Significance of planes

Before investigating the planes in detail for their kinematic coherence, the significance of the best planes returned by the algorithm should be investigated. The best planes are defined as the richest and thinnest ones. The significance of a plane is defined as the probability of finding a plane of a given number of satellites or higher in a random distribution, $P(N \geq N_{\text{in}})$, respecting the radial distribution of the original sample. The probability of finding planes consisting of a given number of satellites or higher in a random sample should be comparably low to be a significant detection. For example, it is easier to include more satellites in a plane if the satellite distribution is less extended and more flat than if it is a spherically symmetric, widespread distribution. For this purpose, for each main halo, 10,000 random samples of the 30 most massive satellites at the infall time, respecting their radial distribution, were generated. To this end, the satellite's radii were kept fixed and their spatial positions were randomised. The plane finding algorithm was applied to these samples, and the number of rich planes with a given number of



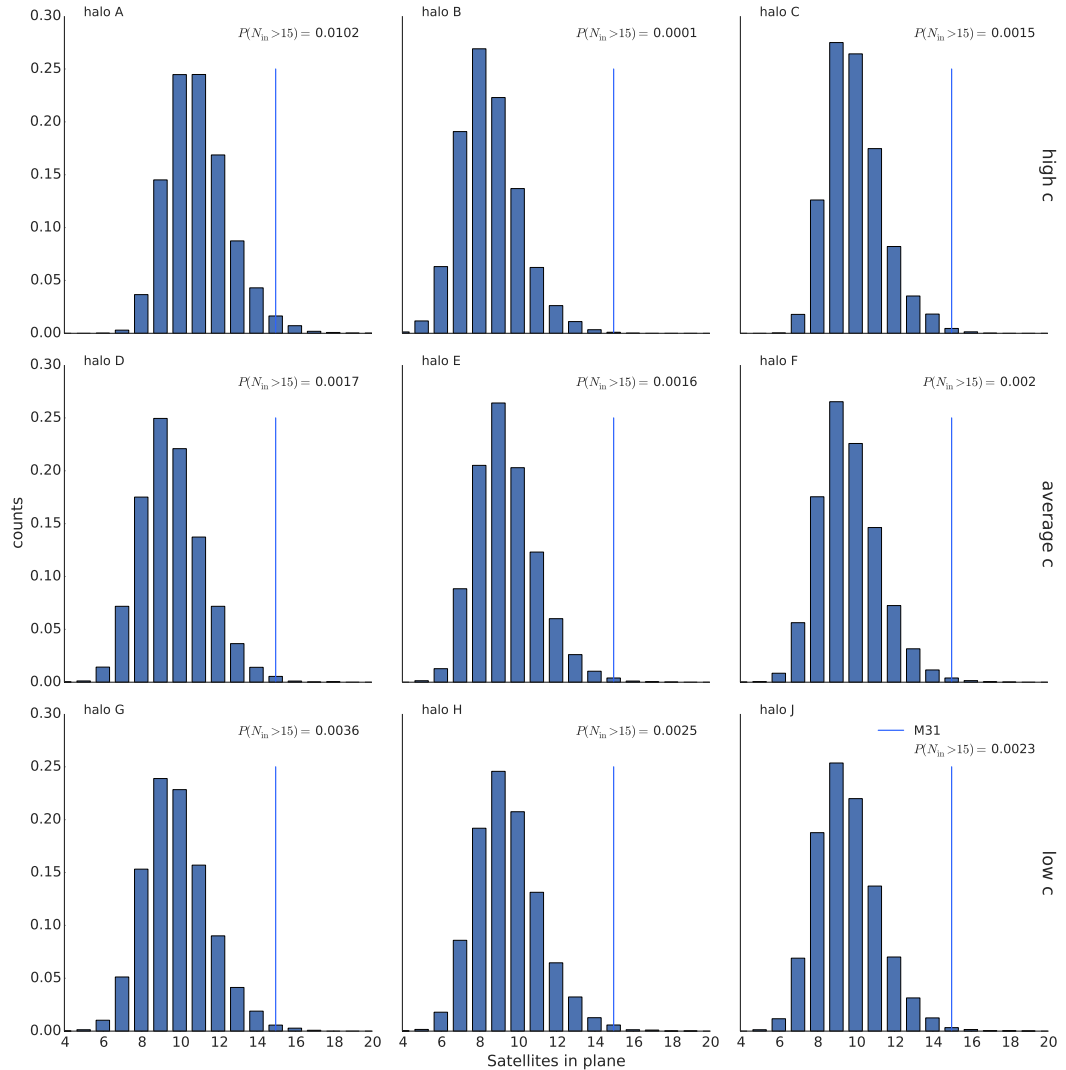
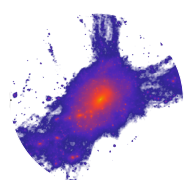


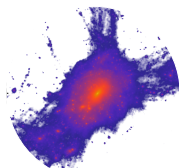
Figure 5.9: The significance of certain individual planes is also demonstrated in Figure 5.7. This is the probability density function for obtaining a plane consisting of N_{in} satellites in a random sample of satellites, respecting the original radial distribution. The *top row* shows high concentration halos, the *middle row* average concentration halos and the *bottom row* shows low concentration halos.



satellites was recorded. This procedure was also utilised by Ibata et al. (2013) to quantify the significance of the plane found around Andromeda and by Gillet et al. (2015) to quantify the significance of planes in their simulations.

Counting the occurrence of planes for every given number of satellites in the plane results in a probability density function for the number of satellites in the plane. In this way, one is able to quantify for a given radial distribution of satellites the significance of a plane fitted to them. A comparison of all of the probability density functions obtained for the simulations is shown in Figure 5.8. Interestingly, for all of the halos, the peak of the distribution is around ~ 10 satellites in the plane with a width of about ± 1 satellite and a tail extending up to around 16 to 18 satellites. Comparable results were also found by Gillet et al. (2015) for their simulations. This means that satellite planes consisting of up to 11 satellites are fully consistent with a random occurrence. Only two high concentration halos show a slightly more pronounced tail, revealing less significant planes if one assumes 15 satellites in a plane. All of the other halos, disregarding their concentration, show very significant planes if 15 satellites are assumed. Looking at planes consisting of only 12 satellites or less, as is the case for average and low concentration halos, the significance drops drastically. The probability of finding such planes in a random distribution is between 7 and 10%, making such planes comparable to random occurrences, while the detection of planes consisting of 15 or more satellites, as in high concentration halos, is very low.

A more detailed view and comparison between individual halos is given in Figure 5.9. This plot shows the significance values of the same selection of halos as shown in Figure 5.7. Once again, the upper row shows high concentration halos, the middle row shows average concentration halos and the bottom row shows low concentration ones. The blue solid line indicates a plane consisting of 15 satellites as observed around Andromeda. In the upper right corner of each panel, the probability of finding a plane consisting of 15 or more satellites is shown. Despite halo A, all of the halos reveal planes which can not be easily found in random distributions with probabilities lower than 0.1% ($P(N_{\text{in}} > 15) < 0.1\%$). But comparing the real number of satellites found in a plane for each halo (for most planes less than 15 satellites) with its associated probability distribution reveals that only the planes of high concentration halos are really significant. For other halos, the significance drops significantly due to the lower number of satellites in the plane.



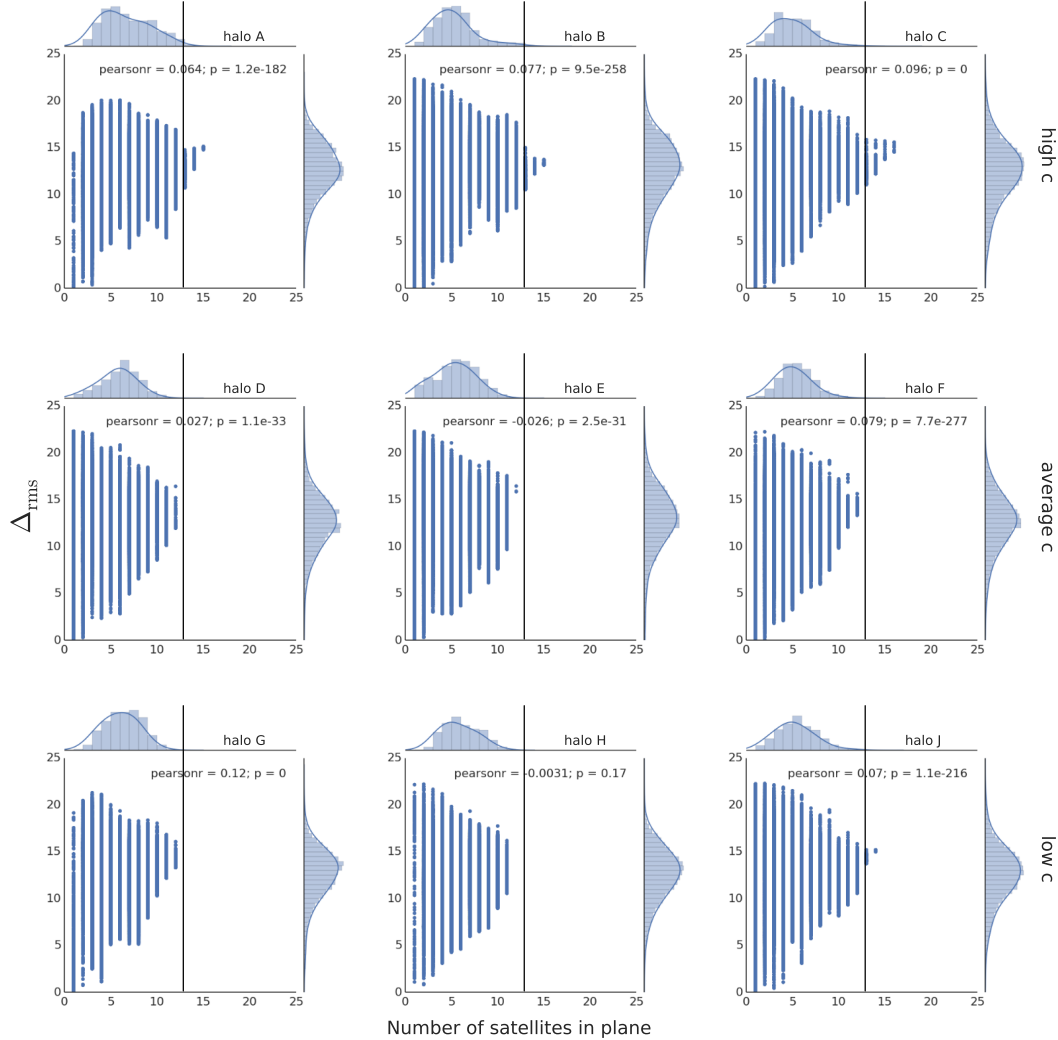
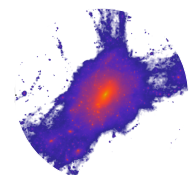


Figure 5.10: The distribution of plane parameters for a particular number of satellites in the plane N_{in} and the rms value, Δ_{rms} , of the associated plane. The *top marginal histogram* shows the cumulation along the y-axis, and the *right marginal histogram* shows the cumulation along the x-axis. The *black line* shows a value of 13 satellites in the plane. The *top row* shows high concentration halos, the *middle row* average concentration halos and the *bottom row* shows low concentration halos.



5.2.1 Distribution of plane parameters

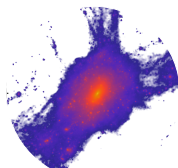
Besides discussing the significance values of the richest planes obtained from the plane finding algorithm, it is interesting to do a more physical comparison of the planes found in different halos. For this purpose, the distribution of values for the number of satellites in the plane, N_{in} , and the root-mean-square thickness, Δ_{rms} , as obtained from the plane finding algorithm are shown. Despite assuming a random distribution of satellites, this procedure reflects that satellite distributions are not random in Λ CDM but that there are physical processes like, for example, accretion via filaments, which shape the satellite distribution. In order to demonstrate the distribution of plane parameters, 100,000 values for the number of satellites in a plane and the corresponding root-mean-square value are recorded during the plane fitting process. Figure 5.10 shows a scatter plot of the plane parameters obtained. For every number of satellites in the plane, N_{in} , the root-mean-square value for the plane thickness of the plane, Δ_{rms} , is plotted. The histogram on the upper x-axis shows the distribution of the number of satellites in the plane, disregarding the thickness. On the right y-axis, a similar distribution for the root-mean-square values of the planes, disregarding the number of satellites, is shown. The solid blue line in the marginal plots shows a kernel density estimation of the probability distribution function. The solid black line indicates a plane consisting of 13 satellites. The overall structure of the panels of the plot is the same as in Figure 5.7 and Figure 5.9, with the upper row showing high concentration halos, the middle row showing average concentration halos and the bottom row showing low concentration ones.

Figure 5.10 shows that there is a large diversity of planes. There is no such thing as a uniquely defined plane. For a given number of satellites in the plane there exist a variety of possible thicknesses. Therefore it is difficult to decide or to define which of the planes should be taken as the best plane.

5.3 Kinematic analysis of planes

5.3.1 Plane appearance under different viewing angles

One peculiarity of the plane finding algorithm is that it does not specify a given viewing direction, but rather takes 100,000 random planes and finds the best plane, which is only thin and extended (and therefore detectable) with an edge-on view. Once the plane is found, it is interesting to study how the appearance of this particular plane evolves if one either rotates it in edge-on view around the normal vector, focusing on the co-rotating measured via the line-of-sight velocity, or if one rotates it around an axis perpendicular to the normal vector, investigating its



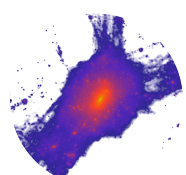
thickening as the inclination angle rises. Both of these dependences are discussed in this subsection.

Planes of satellites are easiest to find when viewed edge-on and impossible to find when inclined. Figure 5.11 shows the appearance of the plane, particularly its thickness, when rotating it from an edge-on view to a face-on view. The solid blue and black lines show the rms value of the plane thickness when rotating the plane around either of the two directions perpendicular to the plane normal. As one expects, the plane thickness basically mimics the behaviour of a solid body plane when rotating it from an edge-on to a face-on view. There is only a small region around the edge-on view where the plane appears really thin. When rotating, depending on the shape of the satellite distribution in the plane, the plane thickness rises steeply towards higher values, reaching almost the same value as the radial root-mean-square extension calculated for the right panel of Figure 5.2. The difference between the value calculated for that plot and the one obtained here is due to the projection effect and the actual shape of the satellite distribution. For Figure 5.11, only the root-mean-square value of the projected distance onto the original edge-on view of the plane is calculated, and not the true radial root-mean-square value.

The dashed blue and black lines show the number of satellites appearing to be projected onto the slit of ± 22 kpc, where the edge-on plane is located when rotating the whole satellite distribution in the same fashion as described above. High concentration halos reveal only one distinct, rich plane, which is only seen edge-on, while average and low concentration halos reveal a much greater degree of scattering in the number of satellites projected into that slit. This might be due to a more spherically symmetric distribution of the satellites in average and low concentration halos, which would also be compatible with the results obtained from the significance study, where the peak for finding planes in a random distribution is around 9 or 10. This number is comparable to the value around which the number of satellites in the slit in these halos fluctuates. The dotted blue and black lines show the corresponding root-mean-square thicknesses of the satellites projected onto the slit. This value is relatively constant, with a value of about 15 kpc for all halos, regardless of the number of satellites in the slit.

Given the results of this plot, it seems to be fairly unlikely to find planes as rich and as thin as the ones observed around Andromeda, unless it is viewed almost edge-on. But nevertheless, these results imply that planes consisting of only around 10 satellites with a root-mean-square thickness of around 15 kpc can be found in more or less every halo.

Moving on to the investigation of the kinematics, it is useful to test the dependence of the count of co-rotating satellites measured via the line-of-sight velocity on the



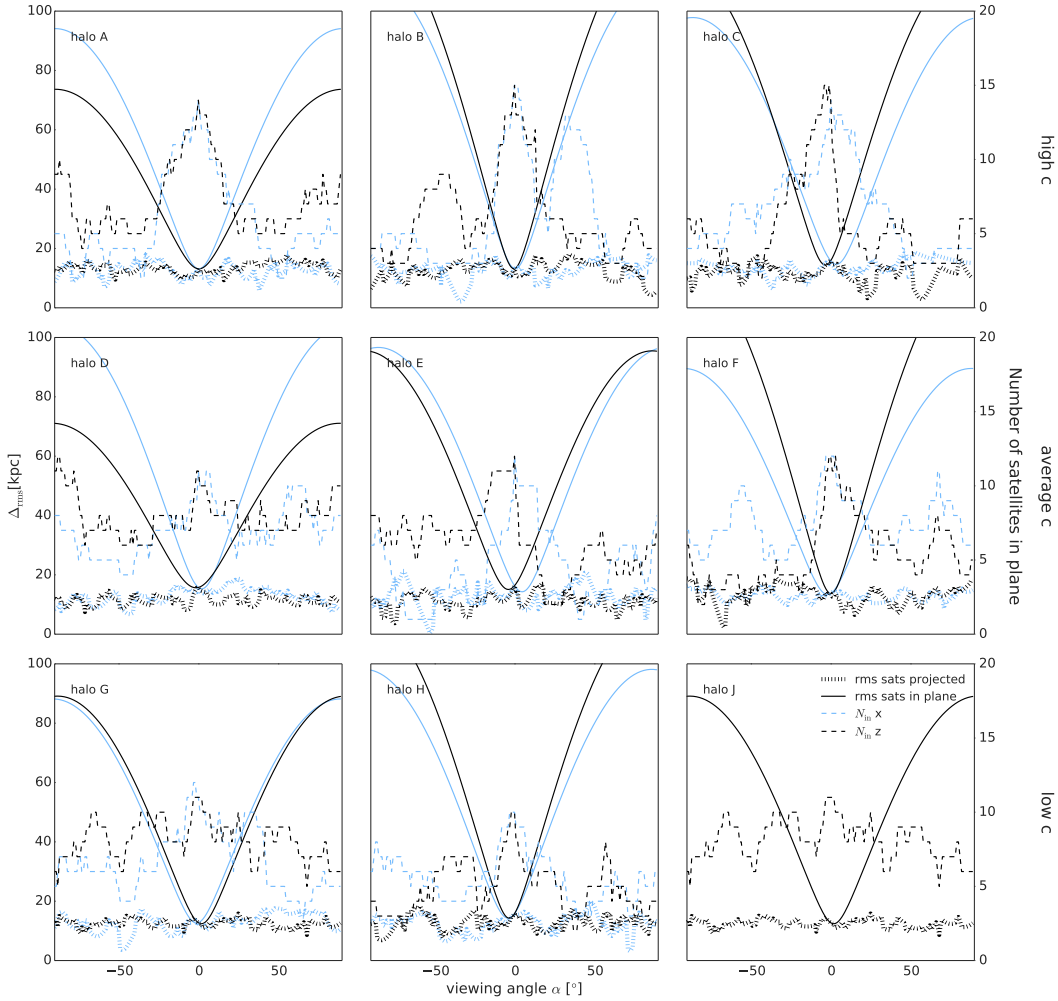
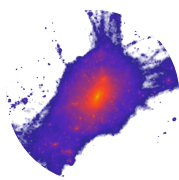


Figure 5.11: The variation of plane parameters as a function of inclination angle to the plane when rotating around an axis perpendicular to the plane normal. *Solid lines*: the rms value, Δ_{rms} , of the plane when the satellites belonging to the plane are fixed. *Short dashed line*: the rms value, Δ_{rms} , of the plane with a fixed width of $\Delta_{\text{rms}} = 22 \text{ kpc}$, with rotation of the satellite configuration allowing satellites to step out of or into the slit. *Long dashed lines*: The number of satellites in the plane with a fixed width of $\Delta_{\text{rms}} = 22 \text{ kpc}$, with rotation of the satellite configuration. The *top row* shows high concentration halos, the *middle row* average concentration halos and the *bottom row* shows low concentration halos.



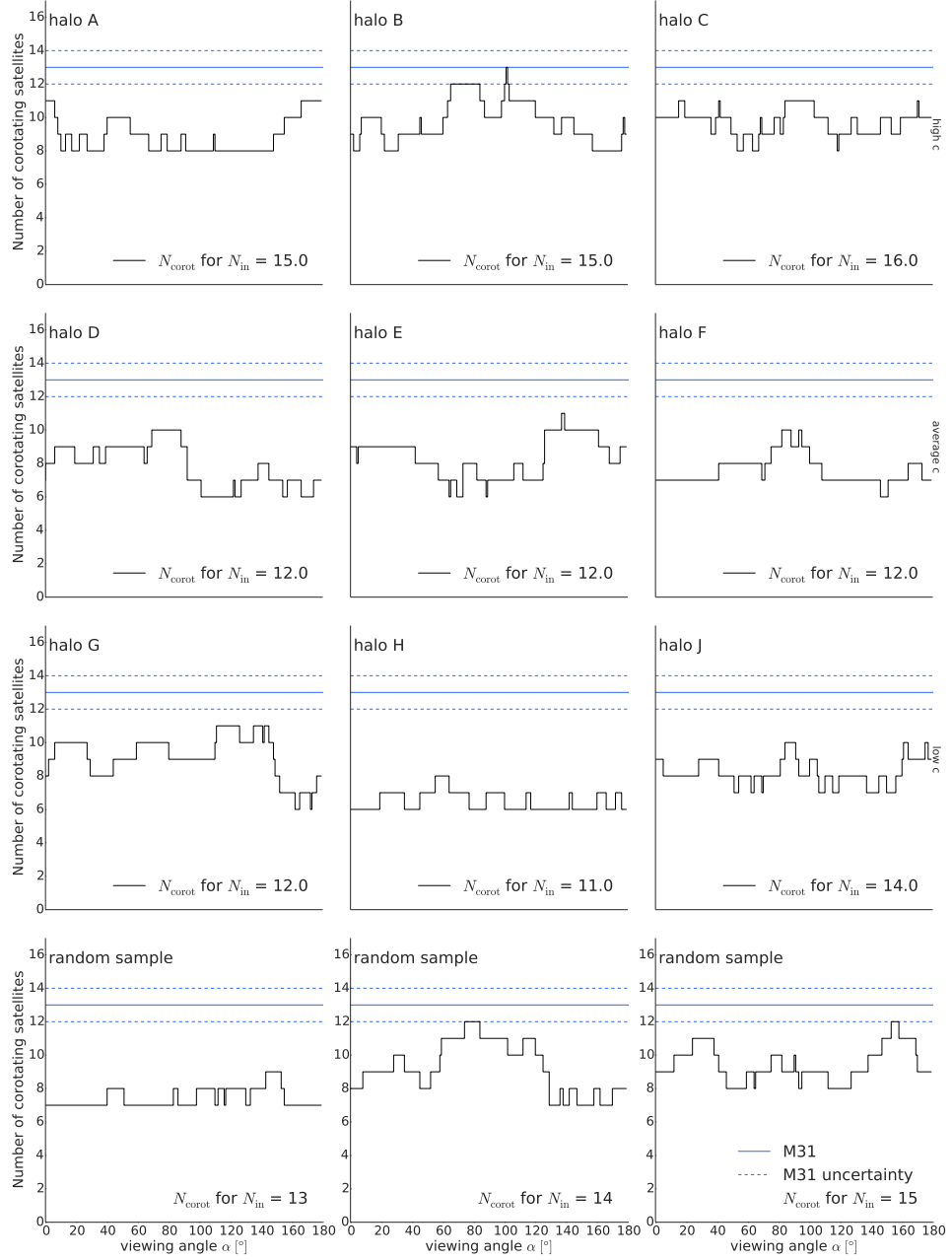
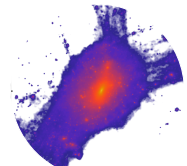


Figure 5.12: The line-of-sight velocity as a function of rotation angle when rotating the plane around the normal vector in edge on view. The *blue line* shows the value measured for Andromeda with *dashed lines* indicating an uncertainty of ± 1 co-rotating satellite. For better comparison, the number of satellites in the plane is also given in the lower right corner of each panel. This plot shows the same selection of halos as in Figure 5.7, with high concentration halos in the *top row*, average concentration halos in the *second row* and low concentration one in the *third row*. Additionally three plots for a random sample of 13, 14 and 15 satellites with randomized positions in the plane and randomized velocities are shown in the *bottom row*.



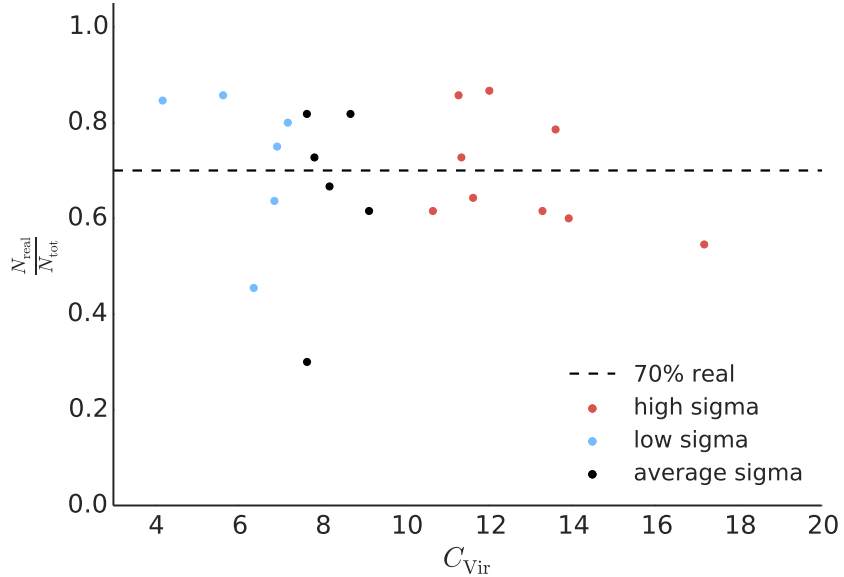
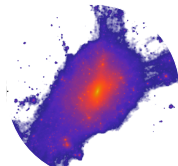


Figure 5.13: The fraction of satellites bound to the plane, color-coded by concentration. The selection criteria for these satellites to be kinematically confined in the plane is the ratio of the velocity component in the plane to the total velocity: $v_{\text{in plane}}^2/v_{\text{tot}}^2 > \frac{2}{3}$. The dashed black line indicates a fraction of 70% real satellites.

viewing angle when rotating the plane with an edge-on view around its normal vector. If the planes found are fully co-rotating, there should be no dependence of the line-of-sight co-rotation fraction on the edge-on viewing position. Thus, when rotating the plane around the normal vector, the line-of-sight count of co-rotating satellites should not vary. But if there are interlopers in the plane that only align with it by chance, these might alter the behaviour. Or, if the plane is not fully rotating, the line-of-sight velocity count should depend on the exact viewing angle.

In Figure 5.12, the number of co-rotating satellites counted via the line-of-sight velocity are shown as a function of the viewing angle with an edge-on view. The figure presents the same selection of halos as shown in the previous plots with high concentration halos in the top row, average concentration halos in the middle row and low concentration halos in the bottom row. For comparison, the number of co-rotating satellites and the total number of satellites in the plane are shown in the lower right corner of each panel. Furthermore, the number of 13 co-rotating satellites observed in Andromeda is shown as a blue solid line with an uncertainty range of ± 1 co-rotating satellites shown as a dashed blue line. The first thing to notice is that there is quite a large variation in the number of co-rotating satellites

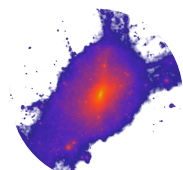


as the viewing angle changes. The overall number of co-rotating satellites is only around 6 to 8 (60% of the co-rotation fraction). Really high co-rotating numbers are only reached at some peaks of the special viewing angles. Despite halo G, which reaches a co-rotation fraction of 100% for one specific peak only, high concentration halos reach higher co-rotation fractions for larger intervals in the viewing angle. But even these halos do not exhibit fully rotating planes. The reason for this could be some special projections of elliptical orbits, counter-rotating satellites or some other projection effect, but the most probable explanation is that the planes are not fully kinematically coherent structures but include a significant amount of “fake” satellites, which have just joined the plane coincidentally. This can be concluded from the comparison to a random sample of 15 satellites shown in the *bottom row*. The line-of-sight counting of co-rotating satellites for a random sample exhibits the same features as the simulated planes. Without specifying which panel is which it is hard to tell whether a random distribution is given or not. Therefore inferring the kinematical coherence of the plane from this measurement is not robust. This can be further concluded from Figure 5.13 which shows the number of satellites confined to the plane counted via an analysis of the velocity components in the plane and perpendicular to the plane. For this plot, the 2-dimensional velocity component in the plane $v_{\text{in plane}}$ is compared to the total velocity v_{tot} . For this purpose the plane normal is assumed to point in the z -direction.

$$v_{\text{in plane}} = \sqrt{v_x^2 + v_y^2} \quad v_{\text{tot}} = \sqrt{v_x^2 + v_y^2 + v_z^2} \quad (5.2)$$

If the motion of satellites is fully random and isotropic, every velocity component should have the same magnitude and the above comparison will result in $v_{\text{in plane}}^2/v_{\text{tot}}^2 = 2/3$. Therefore, this analysis can be used to test satellite planes for their “real” rotation fraction. If $v_{\text{in plane}}^2/v_{\text{tot}}^2 < 2/3$, the velocity component perpendicular to the plane is higher than in a random case and the satellite can be regarded as not taking part in the motion of the plane. Vice versa, if $v_{\text{in plane}}^2/v_{\text{tot}}^2 > 2/3$, the 2-dimensional velocity component in the plane is higher than in the random case, and the satellite’s motion can be regarded as motion in the plane.

Figure 5.13 shows the fraction of satellites belonging to the plane if the above criteria is used to discriminate between “real” and “fake” members as a function of concentration. There is not much difference between the high and low concentration halos. All of the halos reveal planes that contain about $\sim 30\%$ “fake” satellites with a high perpendicular velocity component relative to the plane, indicating that these satellites are just by coincidence members of the plane. These results are in agreement with the findings of Gillet et al. (2015), who find a fraction of about 1/3 of the satellites to be interlopers. This conclusion is also supported by the analysis

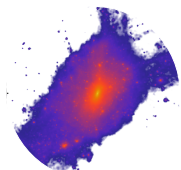


of the angular momentum vectors of the plane members done in subsection 5.3.2 as well as the analysis of the past orbits of the satellites making up the plane at the present time is presented in Figure 5.17.

5.3.2 Angular momentum analysis

Until now, only 1-dimensional or 2-dimensional measures of the kinematical coherence of the plane have been used. In order to capture the motion of the satellites in the 3-dimensional case, and not only as a projection by counting the number of co-rotating satellites by their line-of-sight velocity, it is possible to measure the angular momentum vector of each satellite in the plane and compare its direction to the direction of the plane normal. A similar study was done by Pawłowski et al. (2013) for the 11 classical Milky Way satellites (compare section 4.1.1 and Figure 4.1). The angular momentum vector of the satellites that are fully orbiting counter-clockwise in the plane should point in the same direction as the plane normal. For this analysis, the plane normal vector is set to $(\phi, \theta) = (0, 0)$ in spherical coordinates as seen from the halo center. For satellites that orbit clockwise within the plane, the direction of the angular momentum vector should point in the opposite direction to the plane normal, hence to $(\phi, \theta) = (180, 0)$ or $(\phi, \theta) = (-180, 0)$. Therefore, the main difference between the co- and counter-rotating satellites is the directions of their angular momentum vectors. Satellites that are not orbiting within the plane show a deviation in the directions of their orbital poles from the plane normal. For a better comparison of the clustering of orbital poles, the ones for clockwise orbiting satellites are shifted back by 180° to scatter around $\phi = 0^\circ$ rather than $\phi = \pm 180^\circ$, and are colored blue. The orbital poles for counter-clockwise rotating satellites are kept fixed and are colored red.

In Figure 5.14, for each main halo, the direction of the angular momentum vector of every satellite in the plane as seen from the main halo center and measured in spherical coordinates is shown in a Hammer-Aitoff projection. As in the other multi-panel plots, the high concentration halos are shown in the upper row, average ones in the middle and low concentration halos are plotted in the bottom row. The plane normal at $(\phi, \theta) = (0, 0)$ is shown as a green dot. Furthermore, the spherical standard distance of the Milky Way satellites, measured as the scatter of the angular momentum directions around the mean orbital pole, is shown as a green solid circle of radius $\Delta_{\text{sph}} = 29.3^\circ$ (see Pawłowski et al. (2013)). The spherical standard distance for *all* of the satellites in the planes of the simulations is shown as a dashed black line with the average pole shown as a black dot. For comparison also three random distributions of 13, 14 and 15 orbital poles drawn from a uniform distribution of angles is also shown in the lower most panel.



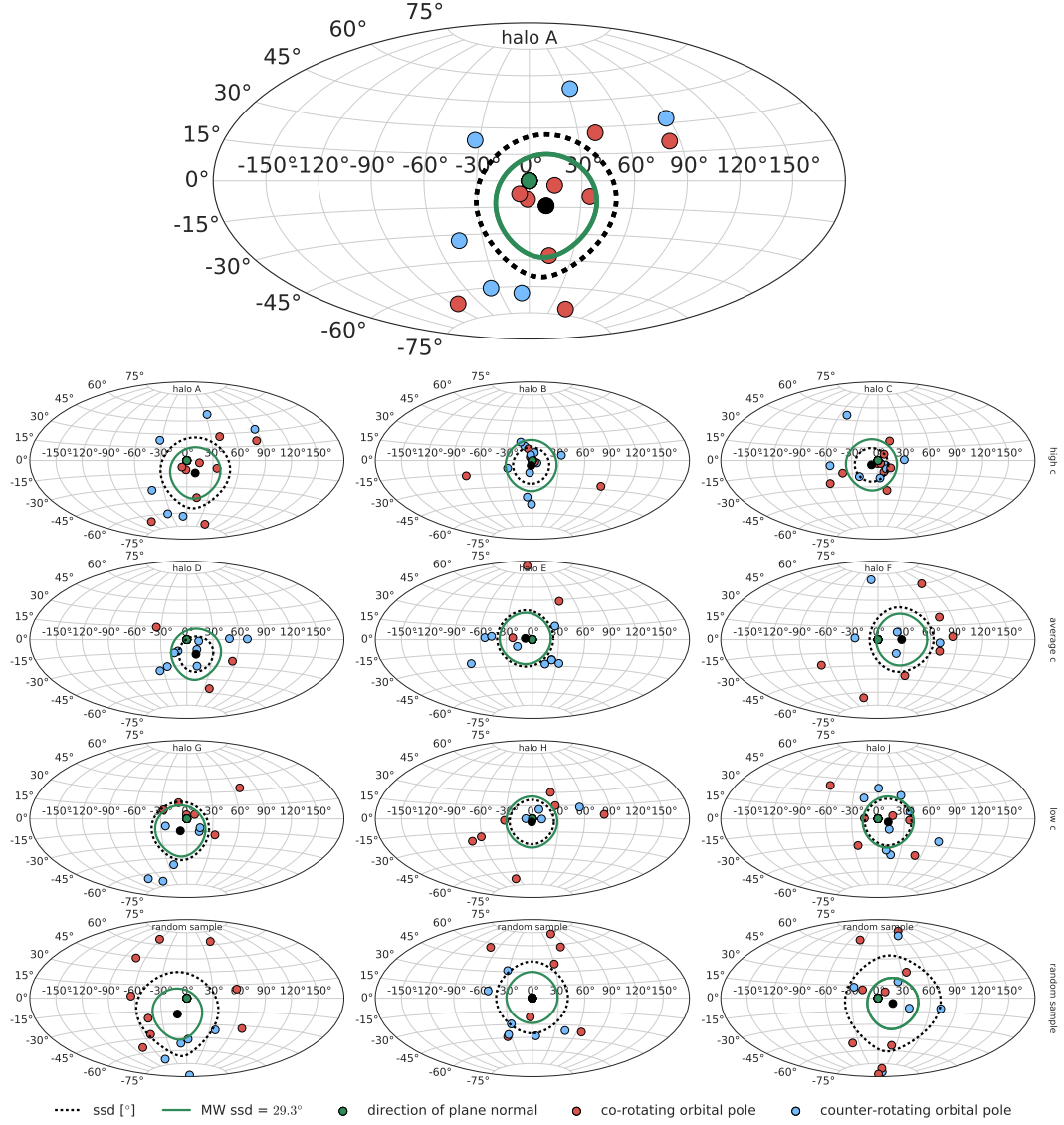
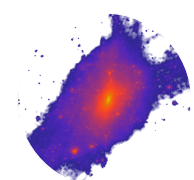


Figure 5.14: A Hammer-Aitoff projection of the orbital poles of the satellites in the plane for the same selection of main halos as shown in the previous plots, plus a random distribution of orbital poles in the lower most panels. The upper most large panel shows halo A also shown in a smaller version in the top left panel for good visibility reasons. The green dot shows the direction of the normal vector of the plane and the color-coded dots show the orbital poles of the co- and counter-rotating satellites, respectively. The green circle shows the spherical standard distance, $\Delta_{\text{sph}} = 29.3^\circ$, of the eight satellites contributing to the best fitting plane of the Milky Way as calculated by Pawłowski et al. (2013). The black dashed line shows the spherical standard distance calculated of all the satellites in the plane with the black dot showing the average orbital pole of all of the satellites. The top row shows high concentration halos, the second row average concentration halos, the third row shows low concentration halos and in the bottom row a random sample consisting of 13, 14 and 15 random orbital poles is plotted.

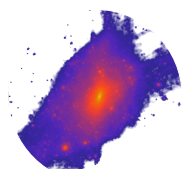


There is a large degree of scattering in the angular momentum directions around the direction of the plane normal, indicating non-ordered motion. If the planes were really to some degree rotating structures as the line-of-sight velocity measurement would indicate, more or less all of the angular momentum directions would cluster near the plane normal direction at $(\phi, \theta) = (0, 0)$. This is obviously not the case, supporting the conclusions drawn from the plots before that the planes are not kinematically coherent structures. The only exceptions are the two upper right panels for the high concentration halos that show more clustering. But even for these halos, about 1/3 of the satellites do not rotate in the plane. This is in agreement with the measurement done for Figure 5.13. For the Milky Way, there are only 8 proper motion measurements used to find a plane from the clustering of orbital poles (Pawlowski et al. 2013). Here all of the halos in the plane found using the algorithm were used to calculate the average pole and the spherical standard distance. For most halos, the calculated spherical standard distance is comparable to that of the Milky Way, but the widespread distribution of orbital poles indicates no coherent motion in the planes. Nevertheless, comparison of the random distribution of orbital poles with the simulations shows that there has to be at least some degree of ordered motion. The orbital poles of the halos in the simulations are less widespread than a random distribution. This is in contrast to the result of Figure 5.12 where no difference to a random sample was found. Therefore the analysis of orbital poles is better suited to measure the co-rotating of satellites in planes than simply count their line-of-sight velocity. Unfortunately it is hard to obtain proper motion information for most of the satellites in Andromeda to do this analysis. It gets even worse if one would do this measurement for satellite planes further away from us than Andromeda.

Encouraged by these findings, it might be interesting to estimate the lifetime of a plane by taking the velocity component of each satellite perpendicular to the plane and multiplying it by an appropriate time scale to estimate the thickening of the plane.

5.3.3 Plane evolution and plane stability

In Figure 5.15, an estimate of the thickening of the best-fit plane at the present time is shown. For this plot, the motion perpendicular to the plane is integrated for the next 150 Myr to estimate how far the satellites in the plane would move. The left panel of Figure 5.15 shows the thickening on an absolute scale while the right panel shows it in terms of the old root-mean-square value, to give a better handle on how the disk appearance changes. Nevertheless this estimate is an upper limit as the disk precession and the exact orbital motion of the satellites is disregarded.



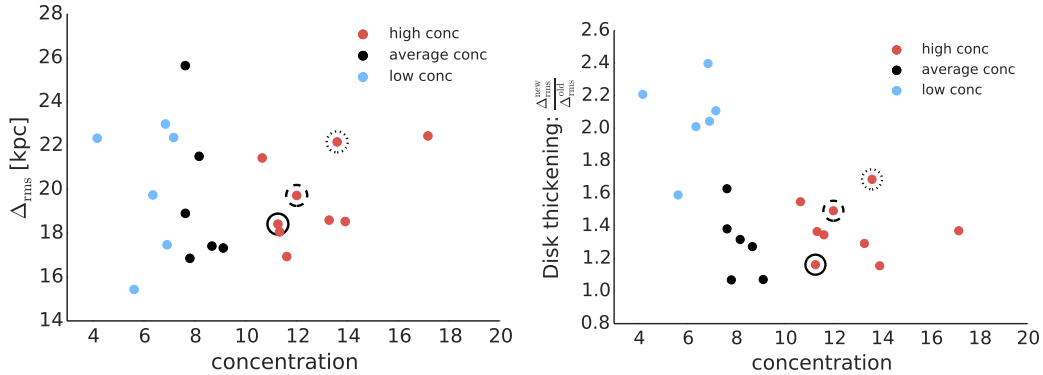


Figure 5.15: Plane thickening. Given the perpendicular velocity of the satellites in the plane, the thickening of the plane after 150 Myr is estimated. *Left panel:* The absolute thickness Δ_{rms} of the plane. The dots show the estimated new root-mean-square thickness of the plane consisting of the satellites originally in the plane. *Right panel:* The new rms value of the satellites previously in the plane in terms of the old value. color-coding divides the halos into high, average and low concentration halos.

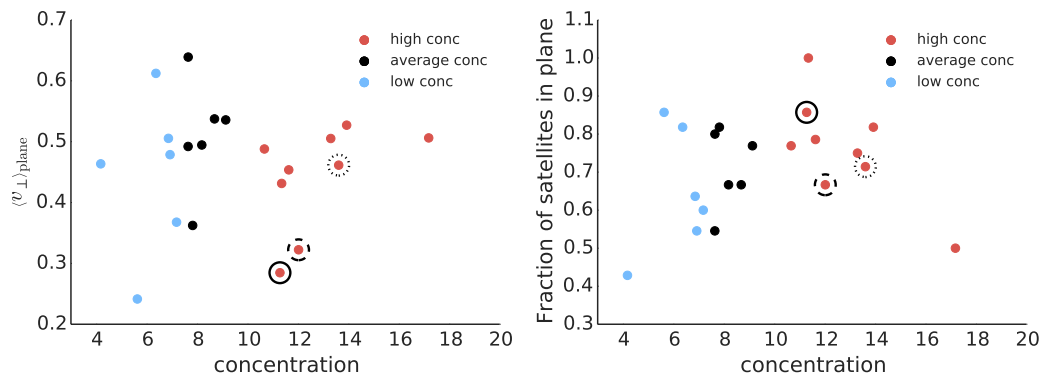
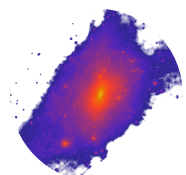


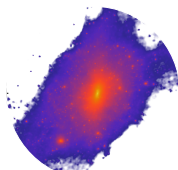
Figure 5.16: *Left panel:* The average perpendicular velocity of all the satellites in the plane of one host as a function of the concentration. *Right panel:* The fraction of satellites in the plane after 150 Myr. The dots show the fraction of satellites still in the region of the original plane, which means they have a perpendicular distance to the plane smaller than the largest distance of satellites at the present time from the plane. Color-coding divides the halos into high, average and low concentration halos.



After 150 Myr, all of the planes show a thickness of more than 15 kpc, or in terms of the old rms, they thicken up by more than a factor of 1.1, whereas the degree of scattering is quite high. Interestingly, there is a strong trend with the concentration. The lower the concentration, the higher the thickening. This is also supported by the left panel of Figure 5.16, which shows the average velocity perpendicular to the plane for all satellites in one plane. There is a slight trend with the concentration, showing that low concentration halos show higher average velocities perpendicular to the plane. But the very large overall scatter makes it impossible to state a clear trend with the concentration. However, the best matching high concentration halos have a comparable low perpendicular velocity.

However, a low value of disk thickening does not directly imply motion in the plane. Since only the velocity perpendicular to the plane is regarded, it is possible that satellites cross through the plane before drifting apart. For example, they could start at one side, cross through the plane of thickness $2\Delta_{\text{rms}}$ and stay within or close to the old boundary of the plane. Thus they move quite a lot perpendicular to the plane but its apparent thickening is not obvious in these plots. Therefore, it might be interesting to additionally analyse how many of the satellites in the plane at the present time are within the same region of the plane after 150 Myr. Therefore, the number of satellites still within the region defined by the distance of the furthest satellite from the plane at the present time are counted. The value of the most distant satellite from the plane gives an upper limit, since this measurement of the thickness is in general greater than the rms value of the plane. The result of this analysis is shown in the right panel of Figure 5.16. This plot shows the fraction of satellites still within the region of the furthest satellite from the old plane after evolving the positions with the perpendicular velocity component 150 Myr into the future. For nearly all halos, the number of satellites drops below $\sim 80\%$ and is on average as low as 70%. Since this is an upper limit on the fraction of satellites still in the plane, it confirms that the plane will disappear on a small time scale. The one high concentration halo, which keeps all its satellites within the region of the furthest satellite, is an example of the fact that this estimate is really an upper limit and does not account for the thickening of the plane due to the reshuffling of the satellites within it. A look at the right panel of Figure 5.15 tells that this plane thickens up to about 1.4 times its original thickness, which is ~ 18 kpc, while keeping all its satellites within the region of the former furthest satellite.

After this simple estimation of the future evolution of the planes, it seems clear that planes of satellites are not a coherent kinematical structures but rather a chance alignment, with at most a backbone of coherently rotating satellites. A more elaborate estimate of the plane's lifetime can be made by following the orbit of the satellites in the plane and tracing their positions back in time. This is done in



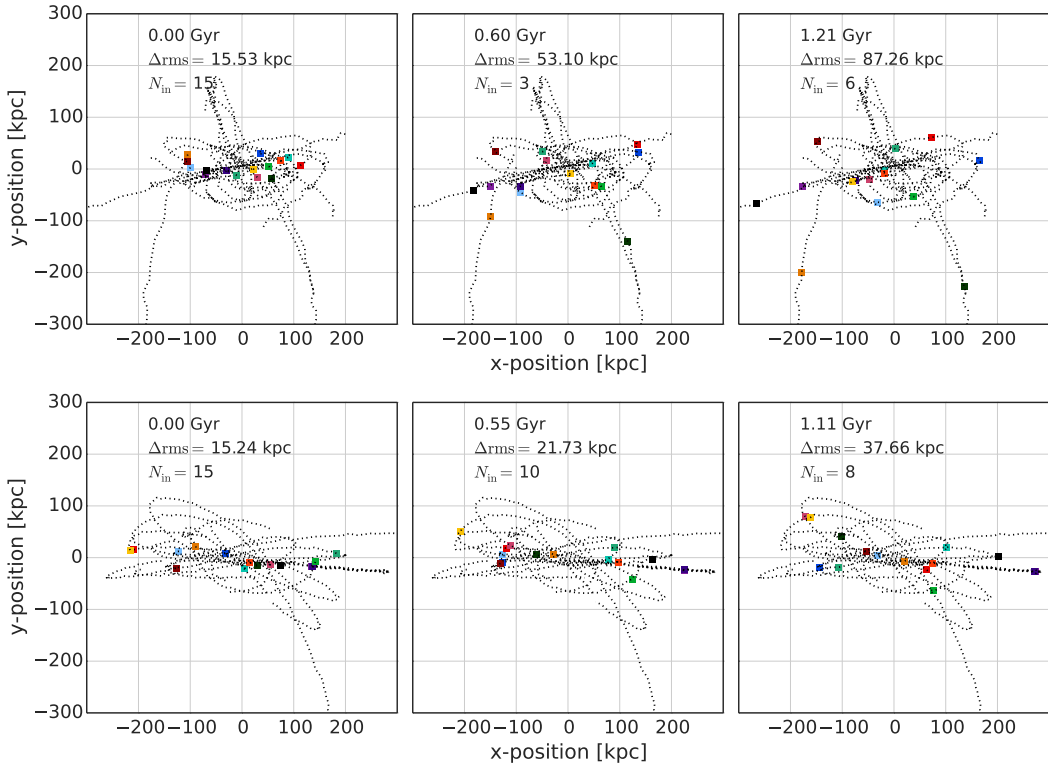
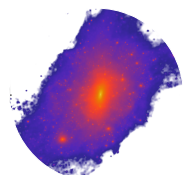


Figure 5.17: Visual impression of the orbits of the satellites in the planes of halo A (top panels) and halo B (bottom panels) with an edge-on view. *Dashed lines* show the trajectories of the satellites and *colored squares* show the positions of the satellites in the planes. From left to right, snapshots at increasingly earlier times are shown. *Left:* The present day configuration, *middle:* the configuration ~ 0.6 Gyr in the past and *right:* ~ 1.2 Gyr ago. In each of the panels, the time, the rms value of the plane and the number of satellites still within the region of the plane at the present time is indicated.

the next subsection for two high concentration halos that show the most promising evidence of a kinematically coherent plane. Additionally, an explanation of the plane formation process will be given in the next section.

5.3.4 Satellite orbits

The plane stability and the evolution of its thickness over the last few Gyr can be investigated by tracking the satellites back in time and investigating their position at the past. One can either look at the satellites making up the best plane at the present time and calculate the corresponding root-mean-square thickness of the



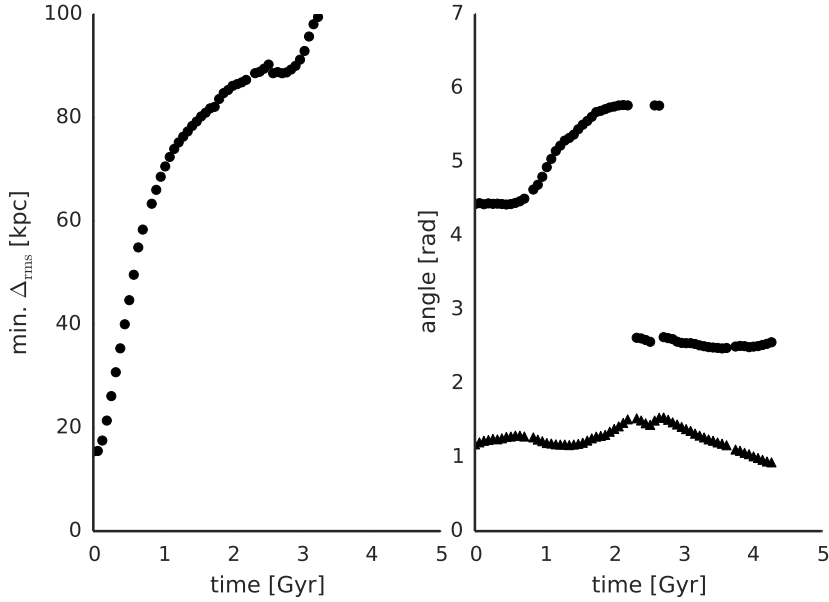
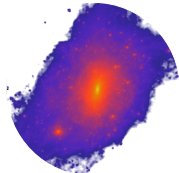


Figure 5.18: The plane thickening as a function of time for the best fitted plane of *halo A*. *Left panel*: The rms value perpendicular to the plane for different time steps going back in time for 4 Gyr. *Right panel*: The evolution of the associated plane normal in spherical coordinates θ (triangles), ϕ (dots) over the past 4 Gyr.

best fitted plane to them (Fig.: 5.18) or rerun the plane finding algorithm on the whole satellite sample at an earlier time to find a new best fitted plane (Fig.: 5.19) probably consisting of a different subset of satellites. Both of these methods were used for two high concentration halos (halo A and halo B).

A visual impression of the orbits of satellites in the planes of halo A and B is given in Figure 5.17. This plot shows the orbit of the satellites ending up in the plane at the present time for about 4 Gyr in the past (grey dotted lines). The three panels of the figure also show the position of each of the satellites with colored squares at the present time (left panel), at ~ 0.6 Gyr in the past (middle panel) and at ~ 1.2 Gyr (right panel). From a quick look at the orbits, it is immediately clear that there is almost no motion in the plane. The tracks of the satellites extend up to a height of about 75 kpc above the plane or are in some cases even perpendicular to the plane at the present time. Furthermore, after only 0.6 Gyr the positions of the satellites indicate a plane thickening up to about 50 kpc for halo A (upper panel) and 20 kpc for halo B (lower panel). After ~ 1.2 Gyr the plane is hardly visible, with an rms value of 87 kpc (halo A) and 37 kpc (halo B).



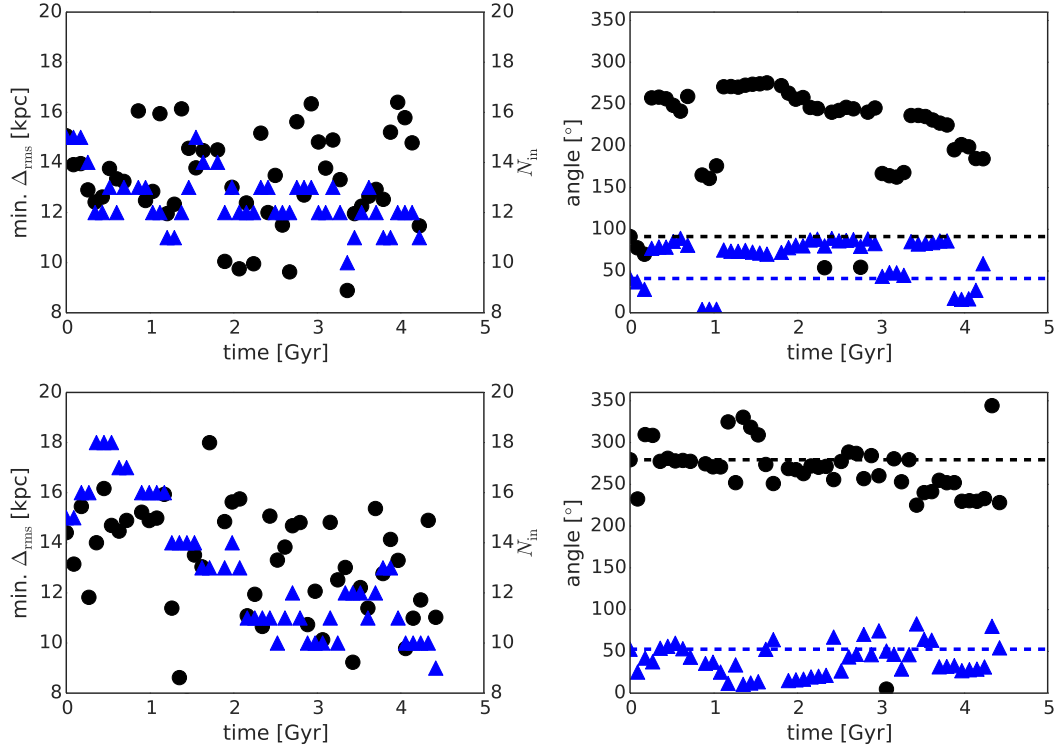
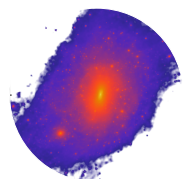


Figure 5.19: The planes at different time steps in the past. *Left panel:* The rms value perpendicular to the plane (black dots) and the number of satellites in the plane (blue triangles, right y-axis) for different time steps of the simulation down to 4 Gyr in the past. *Right panel:* The evolution of the corresponding plane normal in spherical coordinates θ (blue triangles), ϕ (black dots) over the past 4 Gyr. The black and the blue lines show the values of the present day orientation of the plane. The *upper panels* show halo A and the *lower panels* show halo B.

This result is confirmed by Figure 5.18, where the plane finding algorithm was used to find the best-fit plane (the thinnest plane) at earlier times to the positions of the satellites making up the plane at the present time for halo A. The left panel shows the root-mean-square thickness of the plane as a function of time, while the right panel shows the plane normal directions θ and ϕ in degrees as a function of time. The plane thickens up drastically, and after only 1 Gyr the best-fit plane exhibits a thickness of about 60 kpc. Thereby the plane orientation stays almost the same, which can be seen from the right panel of Figure 5.18. After 1 Gyr the plane orientation changes significantly over the course of the next one Gyr, but becomes nearly constant afterwards. The jump at ~ 2.5 Gyr in the past is due to a



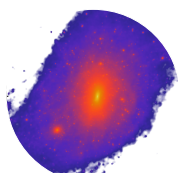
plane normal flip by 180° which does not affect the orientation of the pane. This shows that one specific plane is not stable but rather a transient phenomenon.

A different approach to investigating the behaviour and occurrence of planes over time is to search for planes among the 30 most massive satellites at the infall time at different time steps in the simulation. In this case, the plane finding algorithm is applied to the positions of the 30 satellites selected at the present time at different time steps of the simulation. The outcome of this analysis is presented in Figure 5.19, where the evolution of the plane thickness, Δ_{rms} , number of satellites in the plane, N_{in} , and the plane orientation for halo A and B are shown. Like Figure 5.18 this plot shows in the left panel the rms value of the best-fit plane and in the right panel the corresponding plane normal orientation in spherical coordinates. Additionally, in the left panel, the number of satellites in the best-fit plane is shown with blue triangles and in the right panel the orientation of the present day best plane is indicated with dashed lines (black for ϕ , blue for θ). Figure 5.19 shows that there is a possibility of finding planes with a comparably high number of satellites (~ 12 or even higher) with reasonably low rms values (~ 15 kilopc) over a longer time period (~ 200 Myr). However, regarding the rms value and the number of satellites in the plane, these planes are not stable. The rms value varies between 10 kilopc and 18 kilopc (upper panel) and between 9 kilopc and 16 kilopc (lower panel) for different time steps, and the number of satellites varies. For halo A (upper panel) the variation is only by 1 satellite, and it stays nearly constant at 12 satellites, and for halo B (lower panel) the plane gets richer in the past few time steps but then the number of satellites declines and also fluctuates around 12 satellites in the plane. As the right panel of the figure shows, the normal vector is quite constant over the whole time period and does change only slowly, implying some kind of temporal coherence of the plane. Over the considered time period of ~ 4 Gyr, the planes of both halos exhibit on average about 12 satellites, which is comparable with the estimate that out of the 15 satellites at the present time, at most about 70% are really kinematically coherent.

5.4 Formation scenario and visual impressions of planes

5.4.1 Formation scenario

In this section, the question of where the spatial and kinematic coherence of at least some of the members of the plane does come from is addressed. By tracing the satellites in the plane back to a redshift of $z = 3$, the accretion of the satellites along dark matter filaments can be revealed. This can be seen in Figure 5.20, where



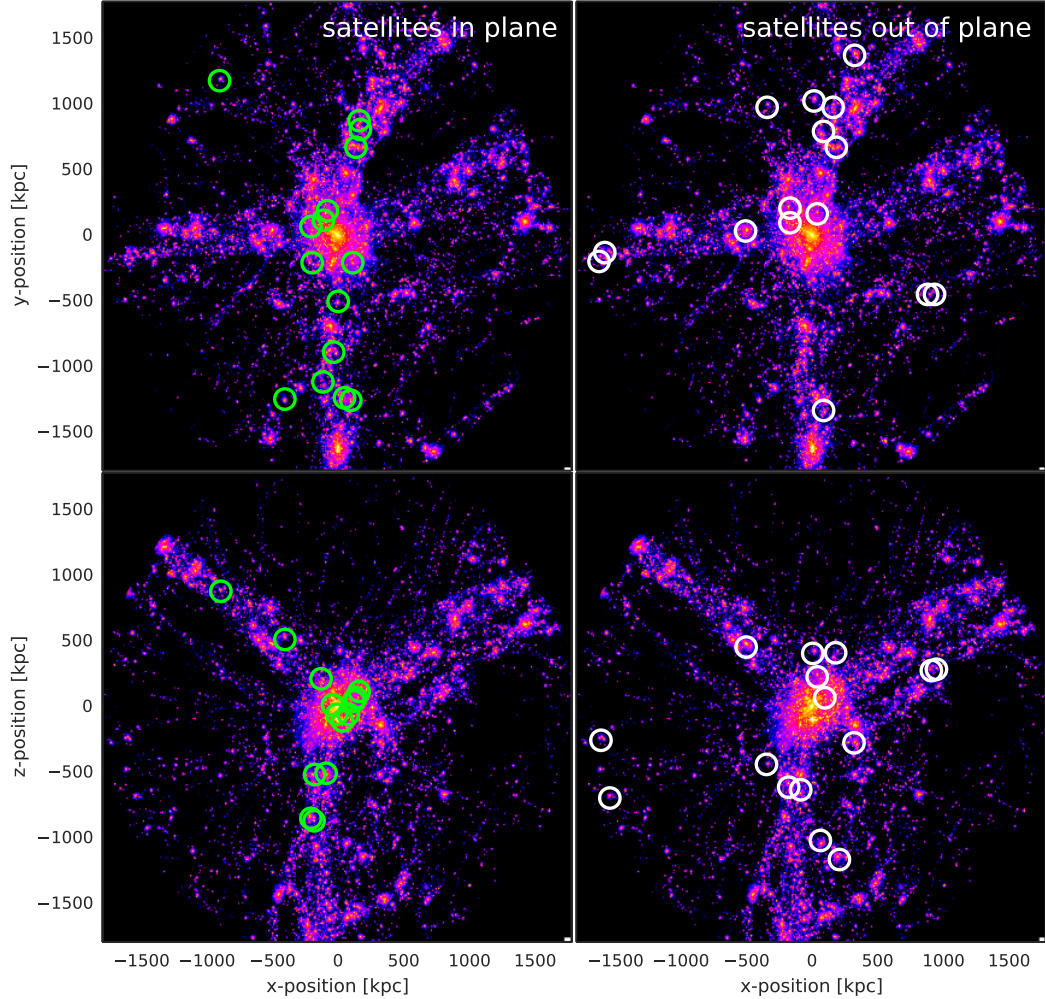
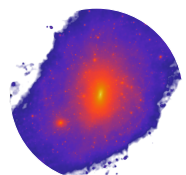


Figure 5.20: High redshift ($z = 3$) density plots of the satellite distribution ending up in the plane and outside of the plane of *halo A*. The *left panel* shows density plots of $x - y$ and $x - z$ -projections of the satellites ending up in the plane at $z = 0$, while the *right panel* shows density plots of the $x - y$ and $x - z$ -projections of the satellites ending up outside of the plane. The upper panel shows that satellites ending up in the plane are accreted along two filaments coming from opposite sides of the main halo, which set a preferred infall direction. On the other hand, satellites that do not end up in the plane are accreted from everywhere. Comparison with the lower panel shows clearly that satellites ending up in the plane lie within the filaments such that their projection collimates in the center of the halo, while satellites that do not end up in the plane scatter around the main halo, indicating that they are not part of the filaments.



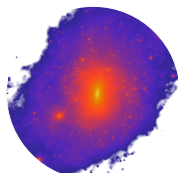
a density plot of the main halo and its substructure at redshift $z = 3$ is shown, indicating the satellites in the plane with green circles and the satellites outside the plane with white circles. Providing two different projections, these plots prove the connection between accretion along the filaments and the property of being in a kinematically coherent plane at redshift $z = 0$. While some of the satellites might be scattered out of the plane when accreted onto the main halo, most of the satellites accreted together stay in a similar orbit. This explains why high concentration halos show more kinematically coherent and richer planes, although even these planes contain up to a 30% chance aligned satellites. In contrast to high concentration halos, low concentration ones form later and not at the crossing points of filaments, which leads to a more uniform accretion of satellites. Therefore the orbits of satellites in low concentration halos are also not as well-ordered as in the high concentration ones.

The presence of a plane of satellites in Andromeda seems then to suggest an (unusual) early formation epoch for this galaxy. Such a scenario is consistent with other observational evidences. For its stellar mass ($\sim 10^{11} M_\odot$), Andromeda lives in a lower mass dark matter halo than typical galaxies of the same mass (Moster et al. 2010). At these stellar masses, the majority of galaxies are bulge-dominated and not star-forming, while Andromeda is disk-dominated and star forming, consistent with an early mass accretion history, and devoid of recent major mergers. A similar line of reasoning also suggests an early formation epoch for the Milky Way.

5.4.2 Visual impression of planes

Figure 5.21 shows one particular projection of the two early forming halos A and B whose plane parameters come closest to those of Andromeda's. The left hand side shows the spatial extension and the kinematics of the systems, clearly revealing a thin but radially extended planes with coherent motion of the satellites around their host. The right hand side shows a dark matter density map of the host halos, with the two satellite populations superimposed, one in the plane (green circles) and one outside the plane (black circles). Such distinct planes were reported previously in CDM simulations (Gillet et al. 2015; Ibata et al. 2014; Pawłowski and Kroupa 2014) but these were not as rich as the ones found here.

It is worth noticing that previous simulation studies were either limited by their substructure resolution, as was the case for Millennium II simulations (Boylan-Kolchin et al. 2009), or, conversely, by a lack of statistics relating to the host halos (Gillet et al. 2015). Moreover, the halos were not selected according to their formation times. Since planes as rich as the one around Andromeda can be found in at least some out of the 21 simulations, the rareness of the planes can be explained



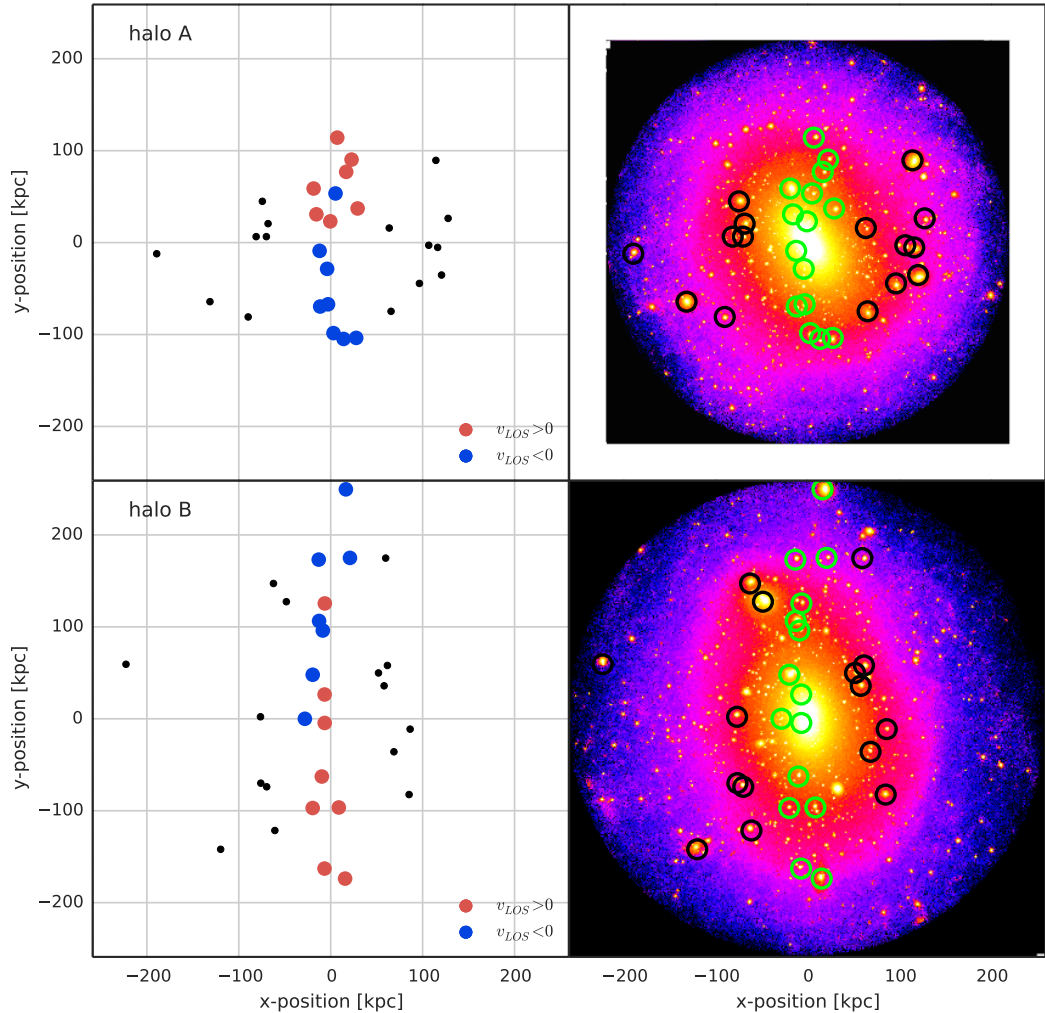
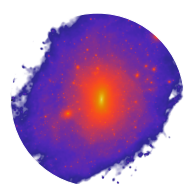


Figure 5.21: An edge-on view of the planes. The *left panels* show the sign of the line-of-sight velocity of the best-fit plane consisting of 15 satellites (colored dots). Black dots show the satellites that are not in the plane. The *right panels* show high resolution density plots of the halo hosting the best matching plane. *Green circles* indicate the subhalos in the plane and *black circles* indicate the subhalos that are not in the plane. *The upper panels* show *halo A*, while the *lower panels* show *halo B*, a slightly more massive halo. These plots also reveal the dependence of radial extension on mass.



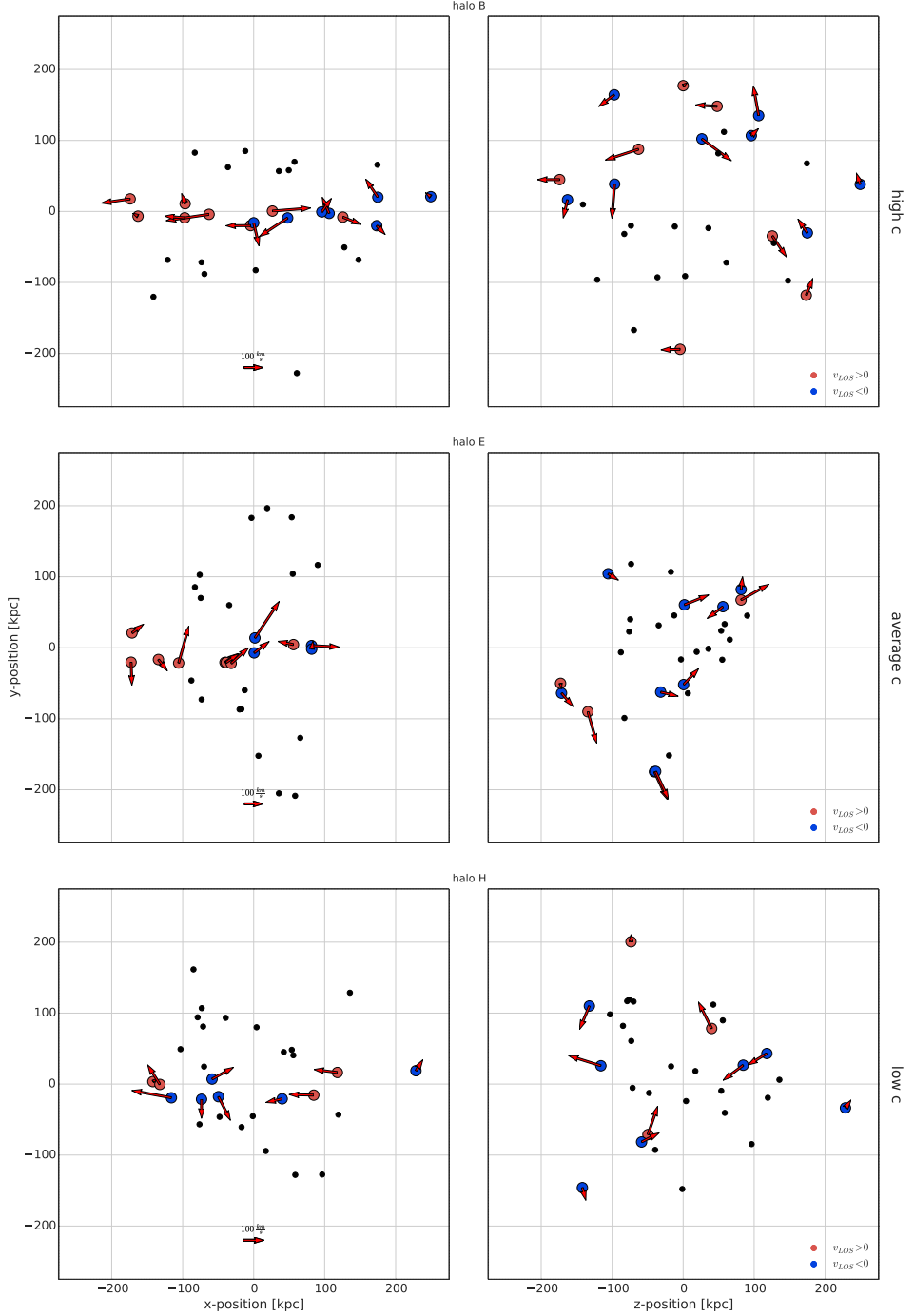
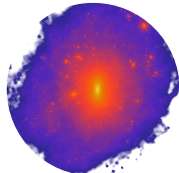


Figure 5.22: A visual impression of the planes. The *left panels* show the sign of the line-of-sight velocity of the planes with edge-on view, while the *right panels* show the planes in face-on view. Black dots show the satellites that lie outside the plane. Arrows indicate the velocity perpendicular to the plane (left panels) and in the plane (right panels). The *top row* shows high concentration halos, the *middle row* average concentration halos and the *bottom row* shows low concentration halos.



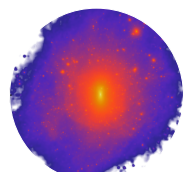
by the rareness of early forming halos. But it is worth noting that although the halos appear in edge-on view to be rotationally supported, detailed analysis of their kinematics reveals that this is not the case. A plane is only partly stable when followed back in time. At most, a plane has a backbone that is kinematically coherent, but a significant fraction of the satellites only appear as a result of chance alignment. This is seen in Figure 5.22 in particular, where a selection of planes of high, average and low concentration halos is shown.

Figure 5.22 shows edge-on (left panel) and face-on (right panel) views of planes found in high, average and low concentration halos. The upper panels show the high concentration *halo B*, the middle panels show the average concentration *halo E* and the bottom panels show the low concentration *halo H*. Satellites in the plane are shown as colored dots with the color indicating the sign of the line-of-sight velocity. Arrows in each plot indicate the other two velocity components. In this way, the upper right panel clearly shows a plane which appears to be rotating to some degree, whereas a look at the edge-on view shows that at least 3 satellites ($\sim 20\%$) have a very high velocity component perpendicular to the plane. This means these satellites are only chance alignments, which quickly leave the plane. Nevertheless, this plane is a very good approximation to the Andromeda plane. It also shows a high degree of lopsidedness, with nearly all of the satellites on one side of the host center. The other panels in this figure are even worse. The lower right panels do not show rotating planes, and the corresponding edge-on views in the left panels show a higher fraction of satellites with high velocity components perpendicular to the plane. Figure 5.22 supports the analysis of previous sections in a nice fashion.

As a final piece of the visual impression, the dependence of the plane shape on the definition of the halo's virial radius should be examined. The halo virial radius is defined via the average over density with respect to the cosmic mean density within a sphere of that radius:

$$\frac{M}{\frac{4\pi}{3}R^3} = \Delta_{\text{vir}}\rho_M \quad (5.3)$$

There are several definitions for the average over density, for example, there exists definitions for $\Delta_{\text{vir}} = 200$ or $\Delta_{\text{vir}} = 100$. The selection of $\Delta_{\text{vir}} = 100$ leads to a bigger virial radius compared to the value for $\Delta_{\text{vir}} = 200$. This leads to totally different planes, since for a bigger virial radius, significantly more substructure in the outskirts of the halo will be included, and thus selecting the 30 most massive satellites at the infall time leads to a more extended satellite distribution. Figure 5.23 shows a comparison of the planes found in the same halo with two different definitions of the virial radius. The left panel shows a plane discussed in this thesis in



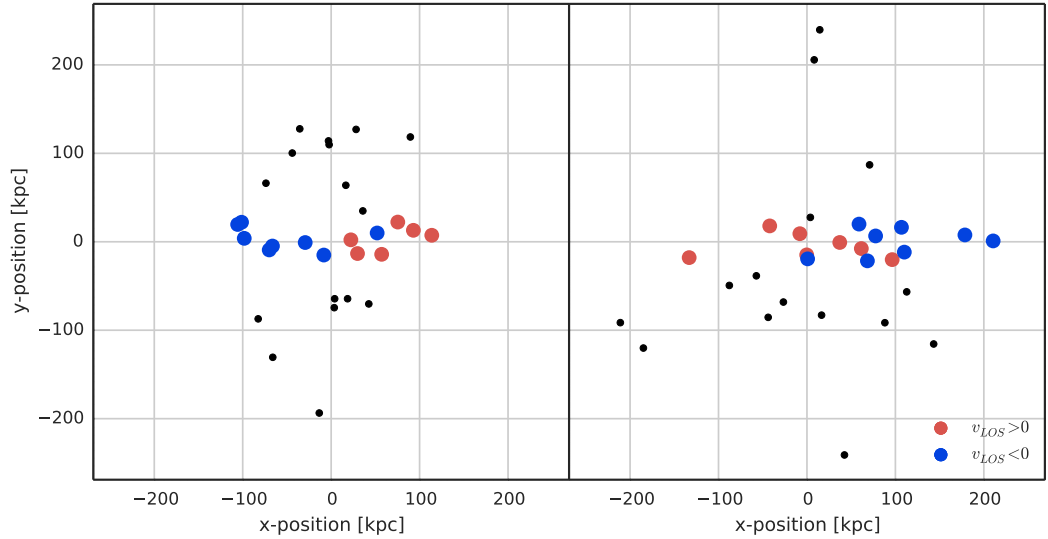
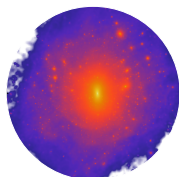


Figure 5.23: A comparison of plane appearance for different definitions of the host halo’s virial radius. *Left:* $\Delta_{\text{vir}} = 200$ *Right:* $\Delta_{\text{vir}} = 100$

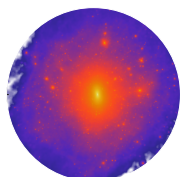
edge-on view, with the definition of $\Delta_{\text{vir}} = 200$, while the right panel shows a plane with the definition $\Delta_{\text{vir}} = 100$. In the right panel, the entire satellite distribution is more extended, and thus the plane appears also more radially extended, while at the same time revealing the same thickness. Since in Andromeda it is not clear whether satellites are within the virial radius of the halo or not, it might be worth investigating the planes of satellites for different definitions of Δ_{vir} and with the additional inclusion of substructure outside of the virial radius. Unfortunately, this is beyond the scope of this thesis and would also require hydrodynamical simulations to robustly select luminous satellites.



6 Summary and Discussion

This thesis investigates the occurrence of planes of satellites in high-resolution Dark Matter only simulations resembling the one observed around our neighbouring galaxy Andromeda (M31) (Ibata et al. 2013), where the kinematic information is based on line-of-sight velocity measurements. Additionally, Pawlowski et al. (2013) claimed to have found a rotating plane around our own Galaxy, the Milky Way. Both studies compare their results to analysis using Millennium II simulations (Boylan-Kolchin et al. 2009) and conclude that rotating planes of satellites are not easily found in simulations of Λ CDM. Thus their reasoning is that Λ CDM is not correct and should be revised.

However, there are two major difficulties with this conclusion. Firstly, the Millennium II simulation has a particle mass of $\sim 10^7 h^{-1} M_\odot$, lacking enough resolution to robustly resolve the substructure needed for this analysis. Secondly, the detection of planes and the conclusion of kinematical coherence based on line-of-sight measurements seems to be not reliable and/or planes that seem to be kinematically coherent appear to be short lived systems. To address both of these issues, high resolution “zoom-in” simulations of 21 roughly Andromeda-mass dark matter halos have been conducted. These simulations use $\sim 10^7$ dark matter particles to resolve the main halo and its substructure, leading to a particle mass of $\sim 10^5 h^{-1} M_\odot$. The simulations can be analysed at different time steps to investigate the temporal evolution of planes. Additionally, halos for re-simulation were selected according to their formation times by selecting either high, average or low concentration halos. The higher the concentration, the earlier the halo formed (Wechsler et al. 2002). Although the observations around Andromeda use a special selection function given by the peculiarities of the Pan-Andromeda Archaeological Survey (McConnachie et al. 2009, PAndAS), for this work we chose not to reproduce the selection function for a number of reasons. Instead, among the hundreds of resolved satellites within the virial radius of the main halo, the 30 most massive ones at the infall time are selected for analysis of their planes. These sub halos are assumed to be the luminous ones (Kravtsov et al. 2004; Conroy et al. 2006; Vale and Ostriker 2006). A plane finding algorithm invoking 100,000 random planes is applied to this sample of satellites, and this algorithm was also used by Ibata et al. (2013) and Gillet et al. (2015). The algorithm finds the thinnest and richest planes seen edge-on. The planes

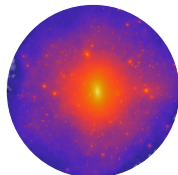


found are characterised by the number of satellites in the plane, N_{in} , the number of co-rotating satellites, N_{corot} , and the root-mean-square value of the plane thickness, Δ_{rms} . The planes are further analysed for the dependence of their parameters on the concentration, their kinematics, the viewing angle and inclination as well as their evolution over time.

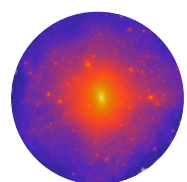
The division of halos into high, average and low concentration halos demonstrates that there is a clear dependence of the plane thickness on concentration. The thinnest planes are only found in high concentration halos. Furthermore, only high concentration halos are able to reproduce the observed planes, consisting of 15 satellites in a plane of width ~ 15 kpc with 13 co-rotating satellites. The reason why high concentration halos are able to produce thinner and richer planes compared to average and low concentration halos is their formation time. High concentration halos form at the nodes of the cosmic web and accrete matter along thin filaments, while average and low concentration halos form later and accrete their matter more uniformly. By tracking satellites in the planes of high concentration halos back through time, it can be shown that most of the satellites in the plane were accreted via filaments, explaining why high concentration halos show thinner and richer planes. By obtaining satellites from special directions (opposite directions), the chance of alignment in a plane becomes higher than in the case of uniform accretion.

In general however, the number of satellites found in a thin plane is about 12, with only a slight dependence on the concentration. However, as Figure 5.11 shows, only high concentration halos seem to show distinct planes for one special viewing angle, while average and low concentration halos are more comparable to a random distribution. One thing that is common to all halos is that planes can only be found when seen edge-on or when only very slightly inclined. It is only in this special orientation that a thin extended plane is visible and detectable. In all other configurations, the plane vanishes.

Once a plane is found in edge-on view and its co-rotation fraction is obtained via line-of-sight velocity measurements, it is not clear if the line-of-sight counting of co-rotating satellites results in the true value of co-rotating satellites. The co-rotation fraction inferred via the line-of-sight velocity measurements is strongly dependent on the specific viewing angle and can vary by as much as ± 6 co-rotating satellites, or about 40%. There are several reasons for this, but the most probable one is that the planes found can contain a lot of interlopers. This is supported by Figures 5.13 and 5.14, which count the number of satellites contained in the plane by the magnitude of the velocity components in the plane or by the angular momenta of the satellites in the plane. Both figures show that the contamination of a plane by interlopers is about 30%. This is also supported by the analysis of the orbits



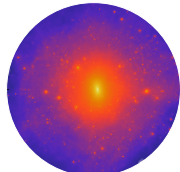
of the satellites in the planes for the two most promising planes, those in halos A and B. The conclusion from this analysis is that the plane is a rather short-lived object consisting of a backbone of satellites in the plane and a significant fraction of chance alignments. A really thin plane is thus a special observation at a special point in time from a special viewing angle, with a comparably high fraction of chance alignments.



7 Conclusion

In this thesis, planes of satellites in high resolution Dark Matter only simulations have been investigated for their kinematics and formation scenarios. The connection between the formation time of a host Dark Matter halo and the alignment of its satellites in a plane as well as the coherent kinematics of its satellites using 21 high-resolution (10 million particles) cosmological N -body simulations has been studied. The key new result is that high concentration (earlier forming) halos tend to have thinner and richer planes. The simulations show that the presence of a thin, rotating, and extended plane of satellites like the one observed around the Andromeda galaxy is not a challenge for the Cold Dark Matter paradigm. Conversely, it supports one of the key predictions of such a model, namely the presence of large filaments of dark matter around galaxies at high redshift and the web-like nature of cosmic structures in the Universe.

However, the rotating planes found contain a significant fraction of interlopers ($\sim 30\%$) and are not long-lived systems. They thicken up on short time scales and are only visible and detectable with an edge-on view. Nevertheless, the simulations performed for this work are dark matter only ones, which do not capture the influence of baryonic physics. Therefore, the selection of luminous satellites according to their mass at the infall time is one questionable point that could be alleviated by using hydrodynamical simulations. Furthermore, as several other studies have shown the impact of baryonic physics on small scales is quite high, it would be desirable to include baryons and re-do all of the analysis with hydrodynamical simulations. Nevertheless, the results obtained here, particularly those for the number of satellites in a plane and the number of interlopers, agree well with the results of other studies, like from Gillet et al. (2015), who used hydrodynamical simulations of two local group analogues. Unfortunately, running hydrodynamical simulations is beyond the scope of this Master's thesis and will be left as future work.



Bibliography

- Abazajian, K. N., Adelman-McCarthy, J. K., Agüeros, M. A., Allam, S. S., Allende Prieto, C., An, D., Anderson, K. S. J., Anderson, S. F., Annis, J., Bahcall, N. A., and et al. (2009). The Seventh Data Release of the Sloan Digital Sky Survey. *ApJS*, 182:543–558.
- Aceves, H. (2013). The radiation energy component of the Hubble function and a LCDM cosmological simulation. *ArXiv e-prints*.
- Anderhalden, D., Diemand, J., Bertone, G., Macciò, A. V., and Schneider, A. (2012). The galactic halo in mixed dark matter cosmologies. *J. Cosmology Astropart. Phys.*, 10:47.
- Barkana, R. and Loeb, A. (1999). The Photoevaporation of Dwarf Galaxies during Reionization. *ApJ*, 523:54–65.
- Barnes, J. and Hut, P. (1986). A hierarchical O($N \log N$) force-calculation algorithm. *Nature*, 324:446–449.
- Bertone, G., Hooper, D., and Silk, J. (2005). Particle dark matter: evidence, candidates and constraints. *Phys. Rep.*, 405:279–390.
- Bertschinger, E. (2001). Multiscale Gaussian Random Fields and Their Application to Cosmological Simulations. *ApJS*, 137:1–20.
- Binney, J. and Tremaine, S. (2008). *Galactic dynamics*. Princeton series in astrophysics. Princeton University Press, Princeton, NJ ; Oxford, 2. ed. edition.
- Boylan-Kolchin, M., Springel, V., White, S. D. M., Jenkins, A., and Lemson, G. (2009). Resolving cosmic structure formation with the Millennium-II Simulation. *MNRAS*, 398:1150–1164.
- Bullock, J. S. (2010). Notes on the Missing Satellites Problem. *ArXiv e-prints*.
- Bullock, J. S., Kravtsov, A. V., and Weinberg, D. H. (2000). Reionization and the Abundance of Galactic Satellites. *ApJ*, 539:517–521.

- Colín, P., Avila-Reese, V., and Valenzuela, O. (2000). Substructure and Halo Density Profiles in a Warm Dark Matter Cosmology. *ApJ*, 542:622–630.
- Conn, A. R., Lewis, G. F., Ibata, R. A., Parker, Q. A., Zucker, D. B., McConnachie, A. W., Martin, N. F., Valls-Gabaud, D., Tanvir, N., Irwin, M. J., Ferguson, A. M. N., and Chapman, S. C. (2013). The Three-dimensional Structure of the M31 Satellite System; Strong Evidence for an Inhomogeneous Distribution of Satellites. *ApJ*, 766:120.
- Conroy, C., Wechsler, R. H., and Kravtsov, A. V. (2006). Modeling Luminosity-dependent Galaxy Clustering through Cosmic Time. *ApJ*, 647:201–214.
- de Blok, W. J. G. and Bosma, A. (2002). High-resolution rotation curves of low surface brightness galaxies. *A&A*, 385:816–846.
- Dekel, A., Birnboim, Y., Engel, G., Freundlich, J., Goerdt, T., Mumcuoglu, M., Neistein, E., Pichon, C., Teyssier, R., and Zinger, E. (2009). Cold streams in early massive hot haloes as the main mode of galaxy formation. *Nature*, 457:451–454.
- Dekel, A. and Silk, J. (1986). The origin of dwarf galaxies, cold dark matter, and biased galaxy formation. *ApJ*, 303:39–55.
- Diemand, J., Kuhlen, M., Madau, P., Zemp, M., Moore, B., Potter, D., and Stadel, J. (2008). Clumps and streams in the local dark matter distribution. *Nature*, 454:735–738.
- Diemand, J., Zemp, M., Moore, B., Stadel, J., and Carollo, C. M. (2005). Cusps in cold dark matter haloes. *MNRAS*, 364:665–673.
- Dubinski, J. (1996). A parallel tree code. *New Astronomy*, 1(2):133–147.
- Dutton, A. A. and Macciò, A. V. (2014). Cold dark matter haloes in the Planck era: evolution of structural parameters for Einasto and NFW profiles. *MNRAS*, 441:3359–3374.
- Flores, R. A. and Primack, J. R. (1994). Observational and theoretical constraints on singular dark matter halos. *ApJ*, 427:L1–L4.
- Gillet, N., Ocvirk, P., Aubert, D., Knebe, A., Libeskind, N., Yepes, G., Gottlöber, S., and Hoffman, Y. (2015). Vast Planes of Satellites in a High-resolution Simulation of the Local Group: Comparison to Andromeda. *ApJ*, 800:34.

- Governato, F., Zolotov, A., Pontzen, A., Christensen, C., Oh, S. H., Brooks, A. M., Quinn, T., Shen, S., and Wadsley, J. (2012). Cuspy no more: how outflows affect the central dark matter and baryon distribution in Λ cold dark matter galaxies. *MNRAS*, 422:1231–1240.
- Herpich, J. (2013). The effect of warm dark matter on hydrodynamical simulations of disk galaxy formation. Master’s thesis, Department of Physics and Astronomy University of Heidelberg.
- Ibata, R. A., Ibata, N. G., Lewis, G. F., Martin, N. F., Conn, A., Elahi, P., Arias, V., and Fernando, N. (2014). A Thousand Shadows of Andromeda: Rotating Planes of Satellites in the Millennium-II Cosmological Simulation. *ApJ*, 784:L6.
- Ibata, R. A., Lewis, G. F., Conn, A. R., Irwin, M. J., McConnachie, A. W., Chapman, S. C., Collins, M. L., Fardal, M., Ferguson, A. M. N., Ibata, N. G., Mackey, A. D., Martin, N. F., Navarro, J., Rich, R. M., Valls-Gabaud, D., and Widrow, L. M. (2013). A vast, thin plane of corotating dwarf galaxies orbiting the Andromeda galaxy. *Nature*, 493:62–65.
- Jones, D. H., Read, M. A., Saunders, W., Colless, M., Jarrett, T., Parker, Q. A., Fairall, A. P., Mauch, T., Sadler, E. M., Watson, F. G., Burton, D., Campbell, L. A., Cass, P., Croom, S. M., Dawe, J., Fiegert, K., Frankcombe, L., Hartley, M., Huchra, J., James, D., Kirby, E., Lahav, O., Lucey, J., Mamon, G. A., Moore, L., Peterson, B. A., Prior, S., Proust, D., Russell, K., Safouris, V., Wakamatsu, K.-I., Westra, E., and Williams, M. (2009). The 6dF Galaxy Survey: final redshift release (DR3) and southern large-scale structures. *MNRAS*, 399:683–698.
- Klypin, A., Kravtsov, A. V., Bullock, J. S., and Primack, J. R. (2001). Resolving the Structure of Cold Dark Matter Halos. *ApJ*, 554:903–915.
- Klypin, A., Kravtsov, A. V., Valenzuela, O., and Prada, F. (1999). Where Are the Missing Galactic Satellites? *ApJ*, 522:82–92.
- Knollmann, S. R. and Knebe, A. (2009). AHF: Amiga’s Halo Finder. *ApJS*, 182:608–624.
- Koch, A. and Grebel, E. K. (2006). The Anisotropic Distribution of M31 Satellite Galaxies: A Polar Great Plane of Early-type Companions. *AJ*, 131:1405–1415.
- Koposov, S., Belokurov, V., Evans, N. W., Hewett, P. C., Irwin, M. J., Gilmore, G., Zucker, D. B., Rix, H.-W., Fellhauer, M., Bell, E. F., and Glushkova, E. V. (2008). The Luminosity Function of the Milky Way Satellites. *ApJ*, 686:279–291.

- Kravtsov, A. V., Gnedin, O. Y., and Klypin, A. A. (2004). The Tumultuous Lives of Galactic Dwarfs and the Missing Satellites Problem. *ApJ*, 609:482–497.
- Kroupa, P., Pawłowski, M., and Milgrom, M. (2012). The Failures of the Standard Model of Cosmology Require a New Paradigm. *International Journal of Modern Physics D*, 21:30003.
- Kroupa, P., Theis, C., and Boily, C. M. (2005). The great disk of Milky-Way satellites and cosmological sub-structures. *A&A*, 431:517–521.
- Lovell, M. R., Eke, V., Frenk, C. S., Gao, L., Jenkins, A., Theuns, T., Wang, J., White, S. D. M., Boyarsky, A., and Ruchayskiy, O. (2012). The haloes of bright satellite galaxies in a warm dark matter universe. *MNRAS*, 420:2318–2324.
- Lynden-Bell, D. (1976). Dwarf galaxies and globular clusters in high velocity hydrogen streams. *MNRAS*, 174:695–710.
- Macciò, A. V. (2010). Milky Way Satellite Properties in a Λ CDM Universe. In Debattista, V. P. and Popescu, C. C., editors, *American Institute of Physics Conference Series*, volume 1240 of *American Institute of Physics Conference Series*, pages 355–358.
- Macciò, A. V., Stinson, G., Brook, C. B., Wadsley, J., Couchman, H. M. P., Shen, S., Gibson, B. K., and Quinn, T. (2012a). Halo Expansion in Cosmological Hydro Simulations: Toward a Baryonic Solution of the Cusp/Core Problem in Massive Spirals. *ApJ*, 744:L9.
- Macciò, A. V., Stinson, G., Brook, C. B., Wadsley, J., Couchman, H. M. P., Shen, S., Gibson, B. K., and Quinn, T. (2012b). Halo Expansion in Cosmological Hydro Simulations: Toward a Baryonic Solution of the Cusp/Core Problem in Massive Spirals. *ApJ*, 744:L9.
- Mashchenko, S., Wadsley, J., and Couchman, H. M. P. (2008). Stellar Feedback in Dwarf Galaxy Formation. *Science*, 319:174–.
- McConnachie, A. W. and Irwin, M. J. (2006). The satellite distribution of M31. *MNRAS*, 365:902–914.
- McConnachie, A. W., Irwin, M. J., Ibata, R. A., Dubinski, J., Widrow, L. M., Martin, N. F., Côté, P., Dotter, A. L., Navarro, J. F., Ferguson, A. M. N., Puzia, T. H., Lewis, G. F., Babul, A., Barmby, P., Bienaymé, O., Chapman, S. C., Cockcroft, R., Collins, M. L. M., Fardal, M. A., Harris, W. E., Huxor, A., Mackey, A. D., Peñarrubia, J.,

- Rich, R. M., Richer, H. B., Siebert, A., Tanvir, N., Valls-Gabaud, D., and Venn, K. A. (2009). The remnants of galaxy formation from a panoramic survey of the region around M31. *Nature*, 461:66–69.
- Metz, M., Kroupa, P., and Libeskind, N. I. (2008). The Orbital Poles of Milky Way Satellite Galaxies: A Rotationally Supported Disk of Satellites. *ApJ*, 680:287–294.
- Moore, B. (1994). Evidence against dissipation-less dark matter from observations of galaxy haloes. *Nature*, 370:629–631.
- Moore, B., Ghigna, S., Governato, F., Lake, G., Quinn, T., Stadel, J., and Tozzi, P. (1999). Dark Matter Substructure within Galactic Halos. *ApJ*, 524:L19–L22.
- Moster, B. P., Somerville, R. S., Maulbetsch, C., van den Bosch, F. C., Macciò, A. V., Naab, T., and Oser, L. (2010). Constraints on the Relationship between Stellar Mass and Halo Mass at Low and High Redshift. *ApJ*, 710:903–923.
- Navarro, J. F., Frenk, C. S., and White, S. D. M. (1996). The Structure of Cold Dark Matter Halos. *ApJ*, 462:563.
- Navarro, J. F., Frenk, C. S., and White, S. D. M. (1997). A Universal Density Profile from Hierarchical Clustering. *ApJ*, 490:493.
- Pawlowski, M. S., Famaey, B., Jerjen, H., Merritt, D., Kroupa, P., Dabringhausen, J., Lüghausen, F., Forbes, D. A., Hensler, G., Hammer, F., Puech, M., Fouquet, S., Flores, H., and Yang, Y. (2014). Co-orbiting satellite galaxy structures are still in conflict with the distribution of primordial dwarf galaxies. *MNRAS*, 442:2362–2380.
- Pawlowski, M. S. and Kroupa, P. (2014). The Vast Polar Structure of the Milky Way Attains New Members. *ApJ*, 790:74.
- Pawlowski, M. S., Kroupa, P., and Jerjen, H. (2013). Dwarf galaxy planes: the discovery of symmetric structures in the Local Group. *MNRAS*, 435:1928–1957.
- Penzias, A. A. and Wilson, R. W. (1965). A Measurement of Excess Antenna Temperature at 4080 Mc/s. *ApJ*, 142:419–421.
- Penzo, C., Macciò, A. V., Casarini, L., Stinson, G. S., and Wadsley, J. (2014). Dark MaGICC: the effect of dark energy on disc galaxy formation. Cosmology does matter. *MNRAS*, 442:176–186.

- Planck Collaboration, Ade, P. A. R., Aghanim, N., Armitage-Caplan, C., Arnaud, M., Ashdown, M., Atrio-Barandela, F., Aumont, J., Baccigalupi, C., Banday, A. J., and et al. (2014). Planck 2013 results. XVI. Cosmological parameters. *A&A*, 571:A16.
- Power, C., Navarro, J. F., Jenkins, A., Frenk, C. S., White, S. D. M., Springel, V., Stadel, J., and Quinn, T. (2003). The inner structure of Λ CDM haloes - I. A numerical convergence study. *MNRAS*, 338:14–34.
- Press, W. H. and Schechter, P. (1974). Formation of Galaxies and Clusters of Galaxies by Self-Similar Gravitational Condensation. *ApJ*, 187:425–438.
- Rees, M. J. (1986). Lyman absorption lines in quasar spectra - Evidence for gravitationally-confined gas in dark minihaloes. *MNRAS*, 218:25P–30P.
- Sawala, T., Frenk, C. S., Fattahi, A., Navarro, J. F., Theuns, T., Bower, R. G., Crain, R. A., Furlong, M., Jenkins, A., Schaller, M., and Schaye, J. (2014). The chosen few: the low mass halos that host faint galaxies. *ArXiv e-prints*.
- Schneider, A., Smith, R. E., Macciò, A. V., and Moore, B. (2012). Non-linear evolution of cosmological structures in warm dark matter models. *MNRAS*, 424:684–698.
- Schneider, P. (2006). *Extragalactic Astronomy and Cosmology*.
- Shandarin, S. F. and Zeldovich, Y. B. (1989). The large-scale structure of the universe: Turbulence, intermittency, structures in a self-gravitating medium. *Reviews of Modern Physics*, 61:185–220.
- Skrutskie, M. F., Cutri, R. M., Stiening, R., Weinberg, M. D., Schneider, S., Carpenter, J. M., Beichman, C., Capps, R., Chester, T., Elias, J., Huchra, J., Liebert, J., Lonsdale, C., Monet, D. G., Price, S., Seitzer, P., Jarrett, T., Kirkpatrick, J. D., Gizis, J. E., Howard, E., Evans, T., Fowler, J., Fullmer, L., Hurt, R., Light, R., Kopan, E. L., Marsh, K. A., McCallon, H. L., Tam, R., Van Dyk, S., and Wheelock, S. (2006). The Two Micron All Sky Survey (2MASS). *AJ*, 131:1163–1183.
- Springel, V. (2010). E pur si muove: Galilean-invariant cosmological hydrodynamical simulations on a moving mesh. *MNRAS*, 401:791–851.
- Springel, V., Frenk, C. S., and White, S. D. M. (2006). The large-scale structure of the Universe. *Nature*, 440:1137–1144.
- Springel, V., Wang, J., Vogelsberger, M., Ludlow, A., Jenkins, A., Helmi, A., Navarro, J. F., Frenk, C. S., and White, S. D. M. (2008). The Aquarius Project: the subhaloes of galactic haloes. *MNRAS*, 391:1685–1711.

- Springel, V., White, S. D. M., Jenkins, A., Frenk, C. S., Yoshida, N., Gao, L., Navarro, J., Thacker, R., Croton, D., Helly, J., Peacock, J. A., Cole, S., Thomas, P., Couchman, H., Evrard, A., Colberg, J., and Pearce, F. (2005). Simulations of the formation, evolution and clustering of galaxies and quasars. *Nature*, 435:629–636.
- Stadel, J. (2013). PkdGRAV2: Parallel fast-multipole cosmological code. Astrophysics Source Code Library.
- Stadel, J. G. (2001). *Cosmological N-body simulations and their analysis*. PhD thesis, UNIVERSITY OF WASHINGTON.
- Tasker, E. J., Brunino, R., Mitchell, N. L., Michielsen, D., Hopton, S., Pearce, F. R., Bryan, G. L., and Theuns, T. (2008). A test suite for quantitative comparison of hydrodynamic codes in astrophysics. *MNRAS*, 390:1267–1281.
- Tegmark, M., Blanton, M. R., Strauss, M. A., Hoyle, F., Schlegel, D., Scoccimarro, R., Vogeley, M. S., Weinberg, D. H., Zehavi, I., Berlind, A., Budavari, T., Connolly, A., Eisenstein, D. J., Finkbeiner, D., Frieman, J. A., Gunn, J. E., Hamilton, A. J. S., Hui, L., Jain, B., Johnston, D., Kent, S., Lin, H., Nakajima, R., Nichol, R. C., Ostriker, J. P., Pope, A., Scranton, R., Seljak, U., Sheth, R. K., Stebbins, A., Szalay, A. S., Szapudi, I., Verde, L., Xu, Y., Annis, J., Bahcall, N. A., Brinkmann, J., Burles, S., Castander, F. J., Csabai, I., Loveday, J., Doi, M., Fukugita, M., Gott, III, J. R., Hennessy, G., Hogg, D. W., Ivezić, Ž., Knapp, G. R., Lamb, D. Q., Lee, B. C., Lupton, R. H., McKay, T. A., Kunszt, P., Munn, J. A., O’Connell, L., Peoples, J., Pier, J. R., Richmond, M., Rockosi, C., Schneider, D. P., Stoughton, C., Tucker, D. L., Vanden Berk, D. E., Yanny, B., York, D. G., and SDSS Collaboration (2004). The Three-Dimensional Power Spectrum of Galaxies from the Sloan Digital Sky Survey. *ApJ*, 606:702–740.
- Thoul, A. A. and Weinberg, D. H. (1996). Hydrodynamic Simulations of Galaxy Formation. II. Photoionization and the Formation of Low-Mass Galaxies. *ApJ*, 465:608.
- Toukmaji, A. Y. and Board, Jr., J. A. (1996). Ewald summation techniques in perspective: a survey. *Computer Physics Communications*, 95:73–92.
- Vader, D., Palpatine, S., Doku, C., Stormtrouper 1, and Skywalker, A. (1977). Implications of the FORCE in a dark matter dominated universe. *Imperial Archives of Dark Sciences*, 1977.
- Vale, A. and Ostriker, J. P. (2006). The non-parametric model for linking galaxy luminosity with halo/subhalo mass. *MNRAS*, 371:1173–1187.

- Wadsley, J. W., Veeravalli, G., and Couchman, H. M. P. (2008). On the treatment of entropy mixing in numerical cosmology. *MNRAS*, 387:427–438.
- Wechsler, R. H., Bullock, J. S., Primack, J. R., Kravtsov, A. V., and Dekel, A. (2002). Concentrations of Dark Halos from Their Assembly Histories. *ApJ*, 568:52–70.
- Zel'dovich, Y. B. (1970). Gravitational instability: An approximate theory for large density perturbations. *A&A*, 5:84–89.
- Zwicky, F. (1933). Die Rotverschiebung von extragalaktischen Nebeln. *Helvetica Physica Acta*, 6:110–127.

List of Figures

1.1	The anisotropies of the Cosmic microwave background (CMB)	5
1.2	All-sky map of the galaxies in the 2MASS survey	6
1.3	Power spectrum and Differential halo number density as a function of mass and redshift	7
2.1	The galaxy distribution obtained from spectroscopic redshift surveys and from mock catalogues.	10
3.1	Schematic of the creation process of the initial conditions for “zoom-in” simulations.	16
3.2	Snapshot of initial conditions for a zoom-in simulation.	17
3.3	Cumulative numbers of the Milky Way substructure, the Virgo Cluster substructure and the simulated model substructure.	21
4.1	An all-sky plot of the orbital poles of the MW satellite galaxies (green dots) in Galactic longitude l and Galactic latitude b in an Aitoff projection.	27
4.2	Satellites around Andromeda as observed in PAndAS	28
4.3	The concentration mass relation and mass growth vs. concentration	29
4.4	The present day cumulative mass function of the 30 most massive satellites at infall time	30
5.1	A density plot of the plane of satellites with values closest to those of Andromeda.	34
5.2	The minimal root-mean-square thickness, min. Δ_{rms}	35
5.3	The minimal root-mean-square thicknesses parallel and perpendicular to the plane	36
5.4	The projected 2 dimensional root-mean-square thickness parallel and perpendicular to the plane	37
5.5	The projected 2-dimensional root-mean-square thickness parallel to the plane	38

5.6	The maximum number of satellites as a function of the concentration and the number of co-rotating satellites vs. the number of satellites in the plane	41
5.7	The number of co-rotating satellites vs. number of satellites in the plane for a selection of halos.	42
5.8	The probability density function of the number of satellites in a plane	44
5.9	The significance of individual planes	45
5.10	A distribution of plane parameters	47
5.11	The variation of plane parameters as a function of inclination angle	50
5.12	The line-of-sight velocity as a function of rotation angle	51
5.13	The fraction of satellites bound to the plane	52
5.14	A Hammer-Aitoff projection of the orbital poles of the satellites in the plane	55
5.15	Plane thickening	57
5.16	The average perpendicular velocity and the fraction of satellites in plane after 150 Myr	57
5.17	The orbits of the satellites in the planes of halo A and halo B with an edge-on view	59
5.18	The plane thickening as a function of time	60
5.19	The planes at different time steps in the past	61
5.20	High redshift ($z = 3$) density plots of the satellite distribution	63
5.21	An edge-on view of the planes	65
5.22	A visual impression of the planes	66
5.23	A comparison of plane appearance for different definitions of the host halo's virial radius	68

Acknowledgments

At the end of my Master thesis I would like to thank all the people that supported my work, not only during the 10 month spent on this thesis, but rather all the people that made it possible to reach this point.

Most notably I would like to thank my supervisors Andrea Macciò and Aaron A. Dutton. I enjoyed working with you during the past ten months. I learned so much about cosmology, galaxy formation and computer simulations from you. You both showed a constant will to support me and listen to my problems, but at the same time you gave me the freedom to approach problems in my own way. You made numerous useful comments on this thesis and most importantly motivated me to make the most out of it.

Particularly I want to thank Andrea Macciò for giving me the opportunity to be a member of his Galaxy Formation in a Dark Universe Group at the Max-Planck-Institut für Astronomie and for giving me full access to all computational resources needed to realize this work.

I would like to thank all members of the Galaxy Formation Group at MPIA for the inspiring group meetings and the nice atmosphere. I really enjoyed the time in this group and hopefully we stay in touch although the group will dissolve soon. I am happy to continue working with you.

All simulations where carried out on the THEO cluster at the Rechenzentrum Garching of the Max-Planck-Gesellschaft and the Max-Planck-Institut für Plasmaphysik.

Furthermore I would like to thank my office mates for making every day a little more enjoyable and reminding me of coffee breaks. And I would like to thank all my friends. Their interest in my work and their sympathy during busy times motivated me and encouraged me to give my best.

Especially I would like to thank Aoife Boyle for reading my thesis and proofing the correct use of language.

Finally I would like to thank my parents and my family, who have supported me at all times and encouraged me to go my own way and who have supported me in doing what I like to do. Without their support this thesis would have not been carried out. Thank you all.

Erklärung

Ich versichere, dass ich diese Arbeit selbstständig verfasst und keine anderen als die angegebenen Quellen und Hilfsmittel benutzt habe.

Heidelberg, den 04. März 2013
